KATHOLIEKE UNIVERSITEIT LEUVEN
FACULTEIT DER TOEGEPASTE WETENSCHAPPEN
DEPARTEMENT WERKTUIGKUNDE
AFDELING PRODUKTIETECHNIEKEN,
MACHINEBOUW EN AUTOMATISERING
Celestijnenlaan 300B – B-3001 Leuven (Heverlee), Belgium

EXPERIMENTAL COMPLIANCE BREAKDOWN AND REAL-TIME OPTICAL DEFORMATION MEASUREMENT OF FLEXIBLE MANIPULATORS

Proefschrift voorgedragen tot
het behalen van het doctoraat
in de toegepaste wetenschappen
door
Francky DEMEESTER

Promotor:
Prof. dr. ir. H. Van Brussel
Copromotor:
Ing. P. Vanherck

92D3 Mei 1992

KATHOLIEKE UNIVERSITEIT LEUVEN
FACULTEIT DER TOEGEPASTE WETENSCHAPPEN
DEPARTEMENT WERKTUIGKUNDE
AFDELING PRODUKTIETECHNIEKEN,
MACHINEBOUW EN AUTOMATISERING
Celestijnenlaan 300B – B-3001 Leuven (Heverlee), Belgium

EXPERIMENTAL COMPLIANCE BREAKDOWN AND REAL-TIME OPTICAL DEFORMATION MEASUREMENT OF FLEXIBLE MANIPULATORS

Proefschrift voorgedragen tot
het behalen van het doctoraat
in de toegepaste wetenschappen
door
Francky DEMEESTER

Jury:
Voorzitter Prof. dr. ir. J. Berlamont, vice-dekaan
Prof. dr. ir. H. Van Brussel, promotor
Ing. P. Vanherck, copromotor
Prof. dr. ir. P. Sas
Prof. dr. ir. A.C.H. Van der Wolf
Universiteit Eindhoven
Prof. dr. ir. J. De Baerdemaeker

U.D.C. 681.3*I29 Mei 1992

D/1992/5769/4
ISBN 90-73802-13-X

The compliance matrix $\mathbf{C}_{ij}$ $(c1_{ij}, \ldots, c8_{ij})$ is determined from this equation. This overdetermined set of equations has no exact solution due to measurement errors and modelling imperfections. The linear least squares principle is often applied in this situation. A numerical reliable method to solve this least squares problem is SVD or QR decomposition [36].

The compliant *joint* j is characterized by the reference planes ij_2 and jk_1 (figure 2.4). The joint deformation $\mathcal{D}_j$ results from equation 2.21:

$$\mathcal{D}_j = \mathcal{D}_{jk_1} - \begin{bmatrix} {}^{jk_1}\mathbf{R}_{ij_2} & {}^{jk_1}\mathbf{L}_{ij_2} \\ \mathbf{O}_3 & {}^{jk_1}\mathbf{R}_{ij_2} \end{bmatrix} \mathcal{D}_{ij_2}. \tag{2.25}$$

The forces $\mathcal{F}_j$ acting on the compliant joint j result from equation 2.19:

$$\mathcal{F}_j = \begin{bmatrix} {}^{jk_1}\mathbf{R}_{ee} & \mathbf{O}_3 \\ {}^{jk_1}\mathbf{L}_{ee} & {}^{jk_1}\mathbf{R}_{ee} \end{bmatrix} \mathcal{F}_{ee}. \tag{2.26}$$

The joint compliance constant c_j is determined from equation 2.10 or 2.11.

The *base* compliance matrix $\mathbf{C}_b$ is determined from equation 2.27:

$$\mathcal{D}_b = \mathbf{C}_b \mathcal{F}_b, \tag{2.27}$$

where $\mathcal{D}_b$ is the deformation of the plane B, coinciding with the mounting plate of the robot. The forces $\mathcal{F}_b$ acting on the base B result from equation 2.19:

$$\mathcal{F}_b = \begin{bmatrix} {}^{b}\mathbf{R}_{ee} & \mathbf{O}_3 \\ {}^{b}\mathbf{L}_{ee} & {}^{b}\mathbf{R}_{ee} \end{bmatrix} \mathcal{F}_{ee} \tag{2.28}$$

2.2.3 Error consideration

Based on the experiences with the experiments performed in section 2.4, an error consideration on the quasi-static compliance breakdown method seems to be useful. Such an error consideration can be divided into two domains. A first domain of possible errors is attached to the quasi-static measurement; errors due the measurement method and the measuring equipment, just as due to the processing of the measured data in the analyzer. On the other hand, also the compliance

Aan Ann

Dankwoord

Graag wil ik mijn oprechte dank betuigen aan allen die direkt of indirekt bijgedragen hebben tot de verwezenlijking van dit doctoraatswerk.

Vooreerst zou ik mijn promotor, *Prof. Hendrik Van Brussel*, willen bedanken voor de wetenschappelijke leiding, mijn copromotor, *Ing. Paul Vanherck*, voor de vele inspirerende discussies aan het bord en voor zijn hulp bij de praktische realisatie van de testen en de testopstellingen, en *Prof. Paul Sas* voor zijn nuttige en gegronde opmerkingen. Hierbij zou ik ook de andere leden van de jury willen bedanken: *Prof. J. Berlamont, Prof. A.C.H. Van der Wolf, en Prof. J. De Baerdemaeker.*

Mijn dank gaat ook naar de collega's op de afdeling PMA, in het bijzonder *Jan Swevers, Hans Thielemans* en *Farid Al-Bender*, naar *iedereen* van de electronische en van de mechanische werkplaats, naar de mensen die voor de computerondersteuning zorgden, in het bijzonder *Philippe Vanherck* en *Jan Thielemans*, naar *iedereen* van het administratief personeel, en naar de opeenvolgende eindwerkstudenten.

Verder wil ik heel speciaal *mijn ouders* bedanken. Voor hun onverdroten steun waar ik al die jaren heb mogen op rekenen.

Tenslotte mijn dank aan *Ann.* Aan haar draag ik dit werk op; zonder haar steun en hulp ware het tijdig klaarkomen van dit doctoraatswerk en van deze tekst een onmogelijke opgave.

Francky Demeester
Leuven, mei 1992

Acknowledgement

The work presented in this thesis has been carried out in the framework of ESPRIT Project 1561: "SACODY". The author would like to acknowledge the support of the Commission of the European Communities, as represented by DG XIII, on Telecommunications, Informations Industries and Innovation, and more especially its CIME Group.

Francky Demeester
Leuven, May 1992

Contents

List of Figures

List of Tables

Nomenclature

The most important notations are summarized below. Symbols that occur only locally in one or a few sections are not mentioned here. All symbols used, including the ones below, are explained in the text. Bold lower case letters (e.g. $\mathbf{p}$) are used for vectors, while bold capital letters (e.g. $\mathbf{A}$) are used for matrices.

General symbols and conventions

t	: time
$\wedge$	: cross product of two vectors
$c_\bullet$	: $\cos a_\bullet$, $\bullet = x, y, z$
$s_\bullet$	: $\sin a_\bullet$, $\bullet = x, y, z$
c_i	: $\cos \alpha_i$, $i = 1, 2, 3$
s_i	: $\sin \alpha_i$, $i = 1, 2, 3$
F	: force
M	: moment
g	: gravitational acceleration ($9.81 \frac{m}{s^2}$)

Homogeneous transforms

$\{XYZ_\bullet\}$	: cartesian coordinate frame $\{\bullet\}$
$X_\bullet, Y_\bullet, Z_\bullet$	: proper axes of corresponding coordinate frame $\bullet$
$x_\bullet, y_\bullet, z_\bullet$	: coordinates defined in coordinate frame $\bullet$
$\bullet_x, \bullet_y, \bullet_z$	: x-, y-, z-component of $\bullet$
${}^j\mathbf{R}_i$	: orientation matrix of frame {i} with respect to frame {j}
${}^j\mathbf{p}_i$	: position vector of the origin of frame {i} with respect to

frame {j}

${}^{j}\mathbf{A}_{i}$	: homogeneous transform describing the position and orientation of frame {i} with respect to frame {j}
$\mathbf{I}_3$	: 3×3 unit matrix
$\mathbf{O}_3$	: 3×3 zero matrix
$\mathbf{J}$	: Jacobian matrix
$\bullet^{t}$	: transpose of $\bullet$
$\bullet^{-1}$	: inverse of $\bullet$

Flexible link deflections

d_x, d_y, d_z	: deflection components along the proper axes of the undeformed link frame
a_x, a_y, a_z	: deflection components about the proper axes of the undeformed link frame

Compliance breakdown

f_{qs}	: quasi-static excitation frequency
$\bullet_a$	: amplitude of the sinusoidal signal $\bullet$
$\mathbf{d}_\bullet$	: displacement vector along the proper axes of the frame at point $\bullet$
$\mathbf{a}_\bullet$	: rotation vector about the proper axes of the frame at point $\bullet$
$\ddot{d}$	: translational acceleration corresponding to displacement d
$\ddot{a}$	: rotational acceleration corresponding to rotation angle a
$\mathcal{D}$	: generalized link deformation vector
$\mathcal{F}$	: generalized force vector applied at the tip of the link
$\mathbf{C}$	: compliance matrix
c_{ij}	: element of the compliance matrix

Strain gauges based link deflection measurements

σ	: yield stress

e : strain
E : YOUNG's modulus of elasticity
τ : shear stress
γ : shear angle
G : shear modulus
M_{by} : bending moment about Y-axis
I_{yy} : moment of inertia about Y-axis
ρ : specific mass of the material
$\mathbf{a}_0$: translational acceleration vector of the beam
$\boldsymbol{\omega}$: rotational velocity vector of the beam
$\dot{\boldsymbol{\omega}}$: rotational acceleration vector of the beam
$\mathbf{B}$: matrix of the proportionality factors between strain and force
$\mathbf{B}'$: inverse of $\mathbf{B}$
b : element of $\mathbf{B}$

Optical link deflection measurements

x_r, y_r : co-ordinates expressed in the reference frame
x_{c_i}, y_{c_i} : co-ordinates expressed in the corrected sensor frame corresponding to PSD i
x_{s_i}, y_{s_i} : co-ordinates expressed in the sensor frame corresponding to PSD i
x_{m_i}, y_{m_i} : co-ordinates expressed in the measuring frame corresponding to PSD i
x_{h_i}, y_{h_i} : co-ordinates expressed in the holder frame corresponding to PSD i
x_{0_i}, y_{0_i} : co-ordinates in the sensor frame of the origin of the measuring frame
α_{0_i} : structural angle between the X-axis of the sensor frame and the X-axis of the measuring frame
S_i : length of distance vector from the origin of the reference frame to the position of the laser spot on PSD i, for the undeformed link
α_i : structural angle between X-axis of reference frame and previous defined distance vector
P : power of the laser diode

λ	: output wavelength of the laser diode
F_d	: focal distance of the laser diode
D	: diameter of the output beam
w_0	: beam radius at the plane where the wave front is flat
θ	: half beam divergence
l_{psd}	: length of PSD
$l_{psd} \times l_{psd}$	: effective sensitive area of PSD
r_{lin}	: linear part of sensitive area of PSD
G_{x_i}, G_{y_i}	: sensitivity factors of PSD i
PSD_{res}	: resolution of PSD
P_a	: allowed incident power per square millimetre on PSD
$\pm d_{max}$	: displacement range of the link
$\pm a_{max}$	: range of the bending angles of the link
F	: focal length of the lens
ϕ	: lens diameter
L	: distance between the lens and the PSD
n	: number of bits of A/D converter
A/D_{res}	: resolution of the A/D converter
A/D_t	: conversion time of A/D converter

Nederlandse samenvatting

N.1 Formulering van het probleem

N.1.1 Formulering van het probleem

In de zestiger en zeventiger jaren werd voorspeld dat robots op grote schaal zouden doorbreken in allerlei industriële toepassingen. Robots zouden alle menselijke tussenkomst in gevaarlijke, eentonige en onnauwkeurige industriële processen vervangen. Buiten in enkele industriële toepassingen, zoals het puntlassen en het verfspuiten in de automobielnijverheid, is echter tot op heden deze doorbraak er nog niet gekomen. De grootste reden voor dit achterwege bijven is onmiskenbaar het gebrek aan nauwkeurigheid waaraan de huidige generatie robots leidt. Om dit gebrek zoveel mogelijk te voorkomen, worden deze robots ontworpen met heel stijve gelederen. Dit maakt hen natuurlijk erg zwaar en beperkt enorm hun maximale snelheid. Daar in de industrie de leuze "Tijd is geld" hoog in het vaandel wordt gedragen, heeft deze beperkte snelheid van deze robots ook bijgedragen tot het achterwege blijven van de voorspelde doorbraak.

De enige oplossing om de snelheid van robots op te drijven, is het bouwen van *lichtgewicht* robots. Door echter het gewicht en de hoeveelheid materiaal van de robot te verminderen, vermindert ook de stijfheid van de robot. Dit resulteert in grotere vervormingen van de robot en dus in een minder nauwkeurig gedrag van de robot. De oplossing voor beide problemen, grote snelheid en grote nauwkeurigheid, is het bouwen van lichtgewicht robots:

- die optimaal ontworpen zijn qua stijfheid,
- waarbij alle, onvermijdbare, vervormingen van de robot on-line gecompenseerd worden door de sturing van de robot.

Om de robot optimaal te ontwerpen qua stijfheid, of om het ontwerp van een reeds bestaande robot of van een prototype robot te verbeteren, is de kennis van de soepele onderdelen van de robot (het identificeren), en van de bijhorende soepelheidswaarden (het kwantificeren), onmisbaar. Het bepalen van deze gegevens wordt de soepelheidsanalyse van de robot geheten. Er bestaan reeds heel wat methoden voor het proefondervindelijk identificeren en kwantificeren van de soepelheden van samengestelde mechanische structuren. Voor het toepassen op robots hebben deze methoden echter enkele nadelen:

- ze nemen heel veel tijd in beslag en zijn enorm duur qua opstelling,
- ze kunnen:
  - ofwel enkel de globale stijfheid aan het eindpunt van de mechanische structuur bepalen ,
  - ofwel de bijdrage van de vervormingen van alle onderdelen van de mechanische structuur tot de globale vervorming van het eindpunt van deze structuur bepalen maar dit enkel voor een welbepaalde, namelijk de opgemeten, configuratie van de mechanische structuur. Voor mechanische structuren met een snel veranderde configuratie waarbij de vervormingen van ieder onderdeel afhankelijk zijn van deze configuratie, zoals dit bij robots het geval is, is dit duidelijk ontoereikend.

Eénmaal de robot qua stijfheid optimaal ontworpen is, rest enkel nog het compenseren van de onvermijdbare, overblijvende vervormingen van de robot. Het compenseren van deze vervormingen kan gebeuren op basis van een soepelheidsmodel van de robot dat eventueel werd bepaald door een proefondervindelijke soepelheidsanalyse van deze robot. Daar hierbij heel wat berekeningen komen kijken en daar voor een bepaalde beweging van de robot alle positie-, oriëntatie- en krachtinformatie beschikbaar moet zijn, is dit enkel uitvoerbaar voor een off-line compensatie van de vervormingen. Hierbij worden de aan te sturen posities en oriëntaties van de robot zodanig gecorrigeerd dat, rekening houdende met de vervormingen van de robot, de robot zijn doel met de gewenste positie en oriëntatie bereikt. Voor heel wat toepassingen, zoals sensorgebaseerde toepassingen, waar enkel on-line

positie- en krachtinformatie beschikbaar is, is deze compensatie, op basis van een soepelheidsmodel van de robot, niet uitvoerbaar. Om in staat te zijn on-line vervormingen te compenseren, zijn on-line vervormingsmetingen noodzakelijk. Liefst geven deze metingen tijdens de uitvoering van een taak onmiddellijk de positie en de oriëntatie van het eindpunt van de robot. De hedendaagse technologie, alsook die in de nabije toekomst, zijn nog niet in staat om dit met voldoende nauwkeurigheid en snelheid te realiseren. Metingen die een lager niveau van sensortechnologie met zich mee brengen, maar die veel realistischer te realiseren zijn, zijn de rechtstreekse metingen van de vervormingen van een gelid van de robot. Er bestaan reeds heel wat meetsystemen die proberen deze metingen te verwezenlijken. Echter, alle in de literatuur gevonden meetsystemen, zijn ontoereikend wat betreft het *on-line* meten van de *ruimtelijke* vervormingen van een robotgelid.

Samenvattend kan het probleem van deze verhandeling als volgt worden geformuleerd:

1. ontwikkel een methode voor het **proefondervindelijk** identificeren en kwantificeren van de **configuratie-onafhankelijke** soepelheden van **alle onderdelen** van een samengestelde mechanische structuur, in het bijzonder van industriële robots.

2. ontwikkel een meetsysteem voor het **on-line** bepalen van de **ruimtelijke** vervormingen van een robotgelid.

N.1.2 Schematisch overzicht van de samenhang van de verhandeling

Figuur N.1 geeft een schematisch overzicht van de samenhang van deze verhandeling. De nummers verwijzen naar de overeenkomstige secties in het Engelse gedeelte van deze verhandeling. De pijlen duiden de opeenvolging aan van de verschillende stappen die noodzakelijk zijn om tot nauwkeurige robots te komen.

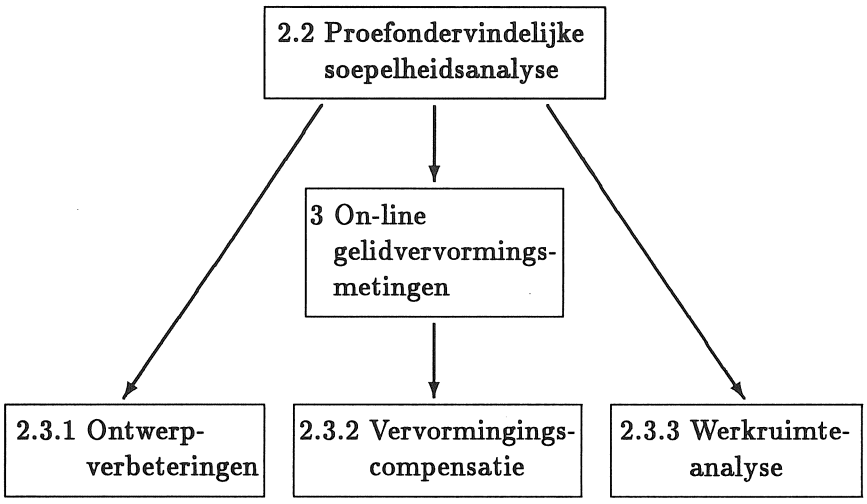

Figuur N.1: Schematisch overzicht van de samenhang van de verhandeling.

N.2 Proefondervindelijke soepelheidsanalyse van industriële robots

N.2.1 Inleiding

Dit hoofdstuk behandelt een proefondervindelijke methode voor het identificeren van de soepele onderdelen in een robot en voor het kwantificeren van de bijhorende soepelheidswaarden. In een aparte sectie wordt de bruikbaarheid van de bekomen resultaten van deze soepelheidsanalyse voor het verbeteren van de robotnauwkeurigheid aan de hand van enkele toepassingen aangetoond.

N.2.2 Quasi-statische soepelheidsanalyse

Een belangrijke stap in het verbeteren van de robotnauwkeurigheid is het identificeren van de soepele onderdelen in een robot en het kwantificeren van de bijhorende soepelheidswaarden. Een literatuurstudie heeft aangetoond dat de quasi-statische soepelheidsanalyse de best aangewezen methode is voor het bepalen van een soepelheidsmodel van een samengestelde mechanische structuur, zoals een industriële

robot.

De quasi-statische soepelheidsanalyse bestaat uit twee opeenvolgende stappen. Eerst, worden de verplaatsingen van de verschillende referentievlakken die een soepel onderdeel kenmerken opgemeten met behulp van een quasi-statische meting. Daarbij wordt ook de aangelegde kracht opgemeten. Daarna worden de soepelheidswaarden van de verschillende onderdelen bepaald op basis van de opgemeten gegevens.

De quasi-statische meetmethode steunt op enkele technieken uit de trillingsanalyse. Om het *statisch* soepelheidsgedrag van een mechanische structuur op te meten wordt de structuur geëxciteerd met behulp van een sinusvormige kracht op een frequentie ver beneden de eerste eigenfrequentie van de structuur. In bepaalde punten van de structuur, welke punten dat zijn wordt later verduidelijkt, worden de versnellingen in drie verschillende richtingen opgemeten. Daar de opgewekte vervormingen sinusvormig zijn, kunnen de overeenkomstige verplaatsingen die in deze punten optreden onmiddellijk uit de opgemeten versnellingen worden afgeleid. De amplitude van deze verplaatsing is namelijk gelijk aan de amplitude van de opgemeten versnelling gedeeld door het kwadraat van de gebruikte excitatiefrequentie en is tegengesteld van teken. Als amplitude van het opgemeten versnellingssignaal wordt enkel de amplitude beschouwd van dat gedeelte van het signaal dat zich op dezelfde frequentie als de excitatiefrequentie bevindt. Indien deze excitatiefrequentie laag genoeg gekozen wordt, kan aan de hand van de frequentierespons van de structuur worden aangetoond dat in een eerste benadering de zonet bepaalde verplaatsingen overeenkomen met de verplaatsingen die zouden worden gemeten indien een even grote statische kracht in hetzelfde punt, als het punt waarin geëxciteerd wordt, aan de structuur zou worden aangelegd. Om deze excitatiefrequentie met de nodige zorg te kunnen bepalen, is het aangewezen om in iedere nieuwe excitatiepositie de frequentierespons van de structuur op te meten. Naast de keuze van de frequentie waarop geëxciteerd wordt, blijkt ook de keuze van de amplitude van de kracht waarmee geëxciteerd zal worden de kwaliteit van de metingen te beïnvloeden. Uit de globale stijfheidskarakteristiek van een structuur blijkt dat deze rond de oorsprong, bij kracht gelijk aan nul, is gekenmerkt door een sterk niet-lineair gedeelte tengevolge van de onvermijdelijk aanwezige speling en wrijving. Om de metingen te kunnen uitvoeren in een meer lineair gedeelte van de globale stijfheidskarak-

teristiek van de structuur is het noodzakelijk een statische voorlast aan de structuur aan te leggen. De amplitude van de kracht waarmee geëxciteerd zal worden, wordt dan gekozen in functie van de totaal toegelaten kracht die aan de structuur mag worden aangelegd.

Op basis van de hiervoor bepaalde verplaatsingen en van de opgemeten excitatiekracht worden in een tweede stap de waarden van de soepelheden van de verschillende opgemeten onderdelen bepaald. Om deze soepelheidswaarden te kunnen bepalen zijn een drietal zaken nodig. Vooreerst moet voor ieder onderdeel van de beschouwde structuur een goed soepelheidsmodel, dat een verband legt tussen de opgetreden vervormingen van het beschouwde onderdeel en de krachten en momenten inwerkend op dit onderdeel, worden gekozen. Dit soepelheidsmodel moet volkomen configuratie-onafhankelijk zijn. In deze verhandeling worden de volgende soepelheidsmodellen gehanteerd. Robotgelederen worden gemodelleerd als lange, symmetrische balken. Hiervoor zijn in de sterkteleer eenvoudige soepelheidsmodellen voor handen. Robotgewrichten worden gemodelleerd als veren: een torsieveer in het geval van een rotatie-gewricht, een lineaire veer in het geval van een translatiegewricht. De andere soepelheden die bij robotgewrichten aanwezig zijn, worden verwaarloosbaar verondersteld in vergelijking met de soepelheid van de beschouwde veer. Tenslotte wordt de robotbasis gemodelleerd door middel van zes veren. Al deze soepelheidsmodellen definiëren de soepelheden voor een bepaald punt of voor een bepaald vlak van het onderdeel en dit gerefereerd ten opzichte van een ander onbeweegbaar punt of vlak van het beschouwde onderdeel. Daarom wordt ieder onderdeel gekenmerkt door twee referentievlakken, die op zichzelf onvervormbaar worden verondersteld: één net voor het beschouwde onderdeel en één er net achter. Door nu ieder referentievlak op de structuur te definiëren door middel van op zijn minst drie punten kunnen de verplaatsingen en rotaties van deze vlakken, ten gevolge van de door de quasi-statische meetmethode aangelegde krachten en momenten, worden berekend vanuit de in de eerste stap van deze meetmethode bepaalde verplaatsingen in deze punten. Nu blijkt dat bij deze berekeningen rekening moet worden gehouden met de invloed van de gravitie op de opgemeten translatieversnellingen. Hiervoor wordt in deze verhandeling een nieuwe methode voorgesteld, die in feite bruikbaar is voor iedereen die met het meten van translatieversnellingen onder gravitatie wordt geconfronteerd. Daar de meeste mensen ech-

ter bij hogere frequenties meten, worden deze invloeden, zonder dat de meesten het beseffen, verwaarloosbaar. Door de verplaatsingen en de rotaties van het referentievlak net voor het beschouwde onderdeel te elimineren uit deze van het referentievlak net achter dit onderdeel blijven enkel de vervormingen van het onderdeel zelf over. Tenslotte wordt vanuit de opgemeten excitatiekracht en vanuit de configuratie van de robot waarbij gemeten wordt de krachten en momenten berekent die op het beschouwde onderdeel inwerken. Vanuit de zonet bepaalde krachten en momenten, en vervormingen worden met behulp van het gepaste soepelheidsmodel de gewenste soepelheidswaarden berekend.

N.2.3 Het verbeteren van de robotnauwkeurigheid

Aan de hand van een literatuurstudie wordt aangetoond hoe de bekomen resultaten van de hierboven beschreven soepelheidsanalyse kunnen bijdragen tot het verbeteren van de robotnauwkeurigheid. Dit wordt nagegaan voor een drietal toepassingen (cfr. figuur N.1): (1) Bij het *ontwerpen van een robot* zijn deze resultaten zeker nuttig voor het maken van enkele kritische ontwerpverbeteringen. (2) Aan de hand van de bekomen resultaten kan de voorspelling en de *compensatie van de vervormingen van het eindpunt van een robot* in de robotprogrammatuur geïntegreerd worden, dit ter verbetering van de nauwkeurigheid van de robot. Dit is bijzonder waardevol bij de off-line programmatie van robots waar de nauwkeurigheid van de robot een kritische factor is voor een succesvolle uitvoering van een robottaak. (3) Tenslotte laten de bekomen resultaten toe om door middel van een *werkruimteanalyse* voor een bepaalde robottaak de beste robothouding en de beste positie van het werkstuk met betrekking tot de robotarm te kiezen.

N.2.4 Praktische toepassingen

Om de nauwkeurigheid van de in dit hoofdstuk ontwikkelde quasi-statische soepelheidsanalyse na te gaan, wordt deze analyse toegepast op een éénzijdig ingeklemde, soepele balk. Voor zo'n balk kunnen de quasi-statisch bepaalde soepelheidswaarden gemakkelijk vergeleken worden met de theoretisch bepaalde en met de statisch bepaalde soepelheidswaarden. Om de algemene toepasbaarheid van de ontwikkelde quasi-statische soepelheidsanalyse aan te tonen, wordt deze analyse

ook toegepast op een samengestelde mechanische structuur, namelijk op een industriële robot. De robot die in deze praktische toepassing wordt gebruikt is een KUKA IR 361/8.0 robot met lange arm. De resultaten van beide praktische toepassingen worden besproken in het besluit van dit hoofdstuk.

N.2.5 Besluit

De, in dit hoofdstuk ontwikkelde, verwezenlijkte en toegepaste, *quasi-statische* soepelheidsanalyse laat toe om de soepele onderdelen in een samengestelde mechanische structuur te identificeren en om de bijhorende soepelheidswaarden *configuratie-onafhankelijk* te kwantificeren. Hierbij is het ook mogelijk om de soepelheidsanalyse uit te voeren op één enkel onderdeel van de mechanische structuur zonder daarbij de volledige structuur te moeten opmeten.

In deze verhandeling werd de soepelheidsanalyse van serieel aangedreven industriële robots benadrukt. Voor dit type van robots werden volgende onderdelen beschouwd: gelederen die als een lange, symmetrische balk kunnen worden gemodelleerd, rotatie-gewrichten en de robotbasis. De modulaire structuur van deze methode laat echter toe om andere types van onderdelen, en andere soepelheidsmodellen voor deze types, aan de in dit hoofdstuk beschreven methode toe te voegen.

Om de quasi-statische soepelheidsanalyse voldoende nauwkeurig te kunnen uitvoeren, werd in dit hoofdstuk een nieuwe methode, die de invloed van de gravitie op de opgemeten translatieversnellingen corrigeert, ontwikkeld. De auteur in niet op de hoogte van het bestaan van enige andere methode die met deze invloed rekening houdt. Niettemin is deze correctie van essentieel belang en is die in feite van toepassing voor iedereen die met het meten van translatieversnellingen onder gravitatie geconfronteerd wordt. Daar de meeste mensen echter bij hogere frequenties meten, worden deze invloeden, zonder dat de meesten het beseffen, verwaarloosbaar.

In een aparte sectie van dit hoofdstuk werd aangetoond hoe de bekomen resultaten van de in dit hoofdstuk beschreven soepelheidsanalyse kunnen bijdragen tot het verbeteren van de robotnauwkeurigheid. Dit werd nagegaan voor het aanbrengen van ontwerpverbeteringen aan een robot, voor het voorspellen en het compenseren van de vervormingen van het eindpunt van een robot, en voor het bepalen van de beste robothouding en de beste positie van het werkstuk met betrekking tot

de robotarm voor een bepaalde robottaak.

De toepassing van de proefondervindelijke, quasi-statische soepelheidsanalyse op een éénzijdig, ingeklemde balk heeft aangetoond dat de haalbare nauwkeurigheid van deze methode heel groot is. De toepassing van deze methode op een industriële robot heeft aangetoond dat deze methode heel geschikt is voor het bepalen van de soepelheidswaarden van de gewrichten van de robot. Het bepalen van de soepelheidswaarden van de gelederen van de robot en van de robotbasis leverde echter geen goede resultaten op. Dit is hoofdzakelijk te wijten aan de moeilijkheden die optreden bij het bepalen van de rotaties van de referentievlakken, die een soepel onderdeel kenmerken, vanuit de opgemeten verplaatsingen van de bij het referentievlak horende punten. Door bij het quasi-statisch meten gebruik te maken van rotatieversnellingsopnemers, naast de reeds gebruikte translatieversnellingsopnemers, zou dit probleem, in theorie dan toch, opgelost zijn en zou deze methode ook goede reslutaten moeten geven voor de soepelheidswaarden van de gelederen van de robot en van de robotbasis. Recent zijn een aantal rotatiebewegingsopnemers op de markt verschenen. Een nauwkeurige analyse van de mogelijkheden van deze opnemers toonde echter aan dat deze voor dit type van toepassing niet geschikt zijn. Het blijkt namelijk dat hun gevoeligheid voor de in deze toepassing opgemeten rotatiebewegingen veel te klein is.

Om de in dit hoofdstuk ontwikkelde proefondervindelijke, quasi-statische soepelheidsanalyse algemeen toepasbaar te maken, werd een programma ontwikkeld dat het configuratie-onafhankelijk soepelheidsmodel van een serieel aangedreven industriële robot bepaald op basis van quasi-statische metingen. Dit programma kreeg de naam **ROBOFLEX**. Figuur E.1 geeft een schematisch overzicht van het **ROBOFLEX**-programma. Door de modulaire opbouw van de programmatuur kan dit programma eenvoudig toepasbaar gemaakt worden voor andere samengestelde mechanische structuren, en voor andere onderdelen.

N.3 On-line vervormingsmetingen van een robotgelid

N.3.1 Inleiding

Dit hoofdstuk behandelt het ontwikkelen van een meetsysteem voor het on-line bepalen van de ruimtelijke vervormingen van een robotgelid. De te bepalen vervormingen zijn diegene die optreden aan het einde van een robotgelid: namelijk twee doorbuigingen, één verlenging, twee buigingshoeken en één torsiehoek. Een literatuurstudie heeft aangetoond dat rekstrookjes en optische opnemers de meest geschikte opnemers zijn voor het opmeten van de vervormingen van een robotgelid. Twee meetsystemen, gebaseerd op de twee verschillende types van opnemers, worden ontwikkeld en praktisch toegepast. Daarbij wordt nagegaan hoe goed ze voldoen aan de kenmerken waaraan een on-line vervormingsmeetsysteem zou moeten voldoen. De kenmerken van het gewenste meetsysteem zijn de volgende:

1. het kan *on-line* alle *ruimtelijke* vervormingen van een robotgelid meten;

2. het kan de vervormingen van het robotgelid nauwkeurig bepalen, en dit met een minimum aan berekeningen;

3. het kan de vervormingen van het robotgelid in het volledige bewegingsbereik van het robotgelid meten;

4. het heeft bij voorkeur een digitale output zodat de bijhorende berekeningen zo snel mogelijk kunnen worden uitgevoerd;

5. het kan in het robotgelid worden ingebouwd;

6. het is eenvoudig te kalibreren;

7. het heeft een redelijke kostprijs (afhankelijk van de toepassing).

In een aparte sectie worden op basis van de twee meetsystemen, die in dit hoofdstuk worden ontwikkeld, enkele alternatieve meetsystemen voor on-line vervormingsmetingen van een robotgelid voorgesteld.

N.3.2 On-line vervormingsmetingen van een robotgelid gebaseerd op rekstrookjesmetingen

Een eerste type van opnemer die wordt onderzocht op zijn geschiktheid voor het opmeten van de vervormingen van een robotgelid is het rekstrookje. Rekstrookjes meten de vervormingen niet rechtstreeks. Het verband tussen de rek, gemeten in een bepaald punt van het robotgelid, en de vervormingen aan het eindpunt van het robotgelid is niet éénduidig maar is afhankelijk van de verandering van de rek langs het robotgelid. Deze verandering van de rek wordt echter wel éénduidig bepaald door de krachten en momenten die op het robotgelid inwerken. Door nu de rek in een aantal punten op het robotgelid te meten, is het mogelijk vanuit de opgemeten rekken deze krachten en momenten te bepalen. De combinatie van deze krachten en momenten met een uitgebreid soepelheidsmodel van het robotgelid geeft de gewenste vervormingen. Dit toont aan dat bij een meetsysteem gebaseerd op rekstrookjes de kennis van de krachten en momenten die op een robotgelid inwerken van essentieel belang is, dit in tegenstelling met bijvoorbeeld een op optische opnemers gebaseerd meetsysteem.

Het aantal punten op een robotgelid waarin de rek moet worden opgemeten, wordt bepaald door het aantal verschillende belastingen die worden beschouwd. In het hier beschouwde meetsysteem wordt rekening gehouden met volgende belastingen: ten opzichte van iedere traagheidsas van de dwarsdoorsnede op het einde van het robotgelid (twee dus) zijn dat de kracht en het moment inwerkend op het einde van het robotgelid, de translatieversnelling (waaronder de gravitatie) waaraan het robotgelid onderhevig is en de rotatieversnelling. Dit geeft een voorlopig totaal van acht verschillende belastingsgevallen. Daar komt nog het torsiemoment, dat op het einde van het robotgelid inwerkt, bij. In totaal geeft dat negen belastingsgevallen. Om iedere belasting te kunnen bepalen, is het opmeten van de rek in negen verschillende punten van het beschouwde robotgelid vereist. Voor het opmeten van het torsiemoment worden best daarvoor speciaal ontwikkelde rekstrookjes gebruikt.

Om de in deze sectie ontwikkelde methode praktisch toe te passen en om de geschiktheid van deze methode voor het meten van de vervormingen van een robotgelid na te gaan, wordt een éénzijdig, ingeklemde balk voorzien van de nodige rekstrookjes en worden de nodige metingen uitgevoerd op deze balk. Het resultaat van deze metingen

zijn de volgende:

1. Het bepalen van de vervormingen van een balk op basis van rekstrookjesmetingen is mogelijk.

2. De nauwkeurigheid waarmee deze vervormingen kunnen worden bepaald, is beperkt daar in praktische toepassingen de evenredigheids- en de soepelheidsfactoren, noodzakelijk voor de berekening van de vervormingen, alleen kunnen worden bepaald door kalibratie, wat in de meeste toepassingen moeilijk met voldoende nauwkeurigheid is uit te voeren.

3. De gemeten rekken zijn heel klein: de rekstrookjes worden enkel gebruikt tot maximaal vijf procent van hun totale bereik. Daardoor worden een aantal bijeffecten heel belangrijk. Deze methode wordt echter wel interessant indien de vervormingen van heel soepele of van heel lange robotgelederen, zoals de armen van een aantal ruimterobots, moeten worden opgemeten. Deze methode is namelijk één van de enige methoden die zo'n grote vervormingen kan meten.

4. Deze methode is enkel bruikbaar indien voor ieder belastingsgeval de nodige rekstrookjes worden voorzien. Een niet-beschouwd belastingsgeval geeft aanleiding tot volledig verkeerde interpretaties.

Deze resultaten tonen aan dat het meten van de vervormingen van een robotgelid gebaseerd op rekstrookjesmetingen niet de meest ideale methode is.

N.3.3 On-line vervormingsmetingen van een robotgelid gebaseerd op metingen met optische opnemers

Een tweede type van opnemer die wordt onderzocht op zijn geschiktheid voor het opmeten van de vervormingen van een robotgelid is de optische opnemer. Door een optische opnemer aan het uiteinde van een robotgelid te bevestigen en de bijhorende lichtbron aan het begin van het robotgelid te bevestigen, is de positie van de lichtvlek, afkomstig van de lichtbron, op de optische opnemer een maat voor de vervormingen van het robotgelid.

Aan de hand van een uitgebreide literatuur- en marktstudie wordt nagegaan welke tweedimensionale optische opnemer en welke lichtbron het meest geschikt zijn voor het beschouwde meetsysteem. Als optische opnemer werd gekozen voor de PSD (positiegevoelige detector). In vergelijking met de andere beschouwde tweedimensionale optische opnemers (CCD's en vierkwadrantencellen) vertoont de PSD een grote positieresolutie, een goed lineair gedrag, een grote reactiesnelheid, een eenvoudige verwerkingselectronica en een onafhankelijkheid van de grote van de lichtvlek. Als lichtbron werd gekozen voor een halfgeleiderlaser. In vergelijking met een HeNe-laser is een halfgeleiderlaser heel compact (bijvoorbeeld 8 bij $17mm$, alle optica inbegrepen), heeft het een langere levensduur (50.000 uren, in vergelijking met 20.000 uren), is het goedkoper, stabilizeert bij het opstarten de laserstraal veel vlugger (10 seconden, in vergelijking met ongeveer 30 minuten) en is het goed geschikt om eventueel binnen in een robotgelid in te bouwen.

Op basis van de hiervoor gekozen optische opnemer en lichtbron, wordt een meetsysteem ontwikkeld, en wordt de bijhorende theorie opgesteld, voor het *on-line* meten van alle *ruimtelijke* vervormingen van een robotgelid. Figuur 3.18 geeft een schematische voorstelling van het ontwikkelde meetsysteem. Het meetsysteem kreeg de naam **DIOMEDES**, wat staat voor "laser **DI**ode **O**ptical system for **ME**asuring structural **DE**flection**S**". Dit meetsysteem meet alle ruimtelijke vervormingen van een robotgelid, met uitzondering van de verlenging van het robotgelid. In de praktijk is deze vervorming echter zo klein dat het verwaarlozen ervan enkel een tweede orde fout oplevert. Het systeem bestaat uit drie halfgeleiderlasers opgesteld aan het ene uiteinde van het robotgelid, en uit drie tweedimensionale positiegevoelige detectoren, waarvan één opgesteld is in het brandvlak van een lens, opgesteld aan het andere uiteinde van het robotgelid. Daar de laserstralen een rechte lijn volgen, onafhankelijk van de vervorming van het robotgelid, bevatten de posities van de lichtvlekken, afkomstig van de halfgeleiderlasers, op de positiegevoelige detectoren alle informatie betreffende de vervormingen van het robotgelid. Het probleem van het bepalen van de vijf vervormingen van het robotgelid uit de zes gemeten coördinaten van de posities van de lichtvlekken op de positiegevoelige detectoren kan worden onderverdeeld in twee deelproblemen. De twee doorbuigingen en de torsiehoek van het robotgelid kunnen wor-

den bepaald vanuit de coördinaten gemeten door de positiegevoelige detectoren zonder lens. Daarvoor moet eerst wel de invloed van de twee buigingshoeken op de opgemeten coördinaten gecorrigeerd worden. Deze buigingshoeken kunnen rechtstreeks worden bepaald vanuit de coördinaten gemeten door de positiegevoelige detector die in het brandvlak van een lens werd geplaatst. Hierdoor is namelijk de positie van de laservlek op deze detector ongevoelig voor de twee doorbuigingen van het robotgelid. Door de twee buigingshoeken te definiëren ten opzichte van een door de torsiehoek verdraait assenstelsel kan ook de invloed van deze laatste vermeden worden.

Het bouwen van een hiervoor besproken meetsysteem verloopt in twee fases: een ontwerpfase, en een opstel- en kalibratiefase. In de ontwerpfase worden de verschillende componenten, waaruit het meetsysteem zal worden opgebouwd, gekozen. In de opstel- en kalibratiefase worden de verschillende componenten indien nodig eerst samengebouwd, zoals bijvoorbeeld het lens-opnemer systeem, en gekalibreerd, en wordt het meetsysteem op het robotgelid opgesteld. Daarbij moeten een aantal parameters, die noodzakelijk zijn voor het berekenen van de vervormingen uit de opgemeten coördinaten, worden gekalibreerd. Beide fases zijn uitgebreid beschreven in deze verhandeling, en zijn van de nodige richtlijnen voorzien.

Op basis van deze richtlijnen wordt een op optisch opnemers gebaseerd, on-line vervormingsmeetsysteem gebouwd en opgesteld op een soepele balk. Het doel van het bouwen van dit meetsysteem is aan te tonen dat dit meetsysteem in staat is om *on-line* alle *ruimtelijke* vervormingen van de balk, met uitzondering van de verlenging van de balk, te bepalen. De resultaten van deze praktische toepassing worden besproken in het besluit van dit hoofdstuk.

N.3.4 Alternatieve methoden voor on-line vervormingsmetingen van een robotgelid

Afgeleid van de twee hiervoor besproken vervormingsmeetsystemen, het op rekstrookjes gebaseerde en het op optische opnemers gebaseerde meetsysteem, worden een tweetal alternatieve meetsystemen voor on-line vervormingsmetingen van een robotgelid voorgesteld. Het eerste alternatieve meetsysteem dat hier wordt voorgesteld, combineert de optische metingen met de rekstrookjesmetingen. Door de torsiehoek met behulp van rekstrookjes op te meten blijkt het mogelijk om in het

op optische opnemers gebaseerde meetsysteem één optische opnemer uit te sparen. Het tweede alternatieve meetsysteem is opgebouwd uit drie lens-opnemer systemen. Hierdoor kan dit meetsysteem met even grote optische opnemers, als in het oorspronkelijke op optische opnemers gebaseerde meetsysteem worden gebruikt, grotere vervormingen meten. Hierbij zijn de berekeningen, vereist voor het bepalen van de vervormingen, wel heel wat ingewikkelder.

N.3.5 Besluit

Dit hoofdstuk toont de uitvoerbaarheid aan om op basis van rekstrookjes en op basis van optische opnemers een meetsysteem te bouwen dat in staat is om *on-line* de *ruimtelijke* vervormingen van een robotgelid te meten. De resultaten van de praktische toepassing van het op rekstrookjes gebaseerde vervormingsmeetsysteem tonen aan dat het meten van de vervormingen van een robotgelid gebaseerd op rekstrookjesmetingen niet de meest ideale methode is. Daarentegen, tonen de resultaten van de praktische toepassing van het op optische opnemers gebaseerde vervormingsmeetsysteem aan dat dit meetsysteem heel goed voldoet aan de, in de inleiding van dit hoofdstuk geformuleerde, kenmerken van het gewenste vervormingsmeetsysteem. Dit meetsysteem haalt een nauwkeurigheid die voor de verschillende opgemeten vervormingen varieert tussen 2% en 10%. Een deel van deze onnauwkeurigheid is te wijten aan de electronica die de analoge signalen, afkomstig van de optische opnemers, versterkt. Ook het on-line karakter van dit meetsysteem werd aangetoond: het meten van de zes coördinaten en het berekenen van de vijf vervormingen hieruit vergt in het totaal, op een PC-AT!!!, minder dan $5ms$. Om het belang van on-line vervormingsmetingen aan te tonen werd dit meetsysteem gebruikt bij het verwezenlijken van een nauwkeurige baansturing van een éénarmige soepele robot. Voor enkele toepassingen, waarin het voorgestelde op optische opnemers gebaseerde vervormingsmeetsysteem niet zou voldoen, werden enkele alternatieve meetsystemen voorgesteld.

N.4 Algemeen besluit

Deze verhandeling stelt een nieuwe proefondervindelijke methode voor de soepelheidsanalyse van samengestelde mechanische structuren voor, met inbegrip van een nieuwe methode voor het corrigeren van de in-

vloed van de gravitatie op translatieversnellingsmetingen, en toont de uitvoerbaarheid aan om op basis van rekstrookjes en op basis van optische opnemers on-line de ruimtelijke vervormingen van een robotgelid te meten.

De nieuwe, in deze verhandeling voorgestelde, quasi-statische soepelheidsanalyse laat toe om de soepele onderdelen in een samengestelde mechanische structuur *proefondervindelijk* te identificeren en om de bijhorende soepelheidswaarden *configuratie-onafhankelijk* te kwantificeren. Hierbij is het mogelijk om de soepelheidsanalyse uit te voeren op één enkel onderdeel van de mechanische structuur zonder daarbij de volledige structuur te moeten opmeten.

In deze verhandeling wordt de soepelheidsanalyse van serieel aangedreven industriële robots benadrukt. Voor dit type van robots worden volgende onderdelen beschouwd: gelederen die als een lange, symmetrische balk kunnen worden gemodelleerd, rotatie-gewrichten en de robotbasis. De modulaire structuur van deze methode, en van het bijhorende programma dat werd ontwikkeld binnen deze verhandeling, laat echter toe om andere types van onderdelen, en andere soepelheidsmodellen voor deze types, toe te voegen.

Om de quasi-statische soepelheidsanalyse voldoende nauwkeurig te kunnen uitvoeren, stelt deze verhandeling een nieuwe methode die de invloed van de gravitie op de opgemeten translatieversnellingen corrigeert voor. De auteur in niet op de hoogte van het bestaan van enige andere methode die met deze invloed rekening houdt. Niettemin is deze correctie van essentieel belang en is die in feite van toepassing voor iedereen die met het meten van translatieversnellingen onder gravitatie geconfronteerd wordt. Daar de meeste mensen echter bij hogere frequenties meten, worden deze invloeden, zonder dat de meesten het beseffen, verwaarloosbaar.

De resultaten van de quasi-statische soepelheidsanalyse dragen op verschillende manieren bij tot het verbeteren van de robotnauwkeurigheid: bij het aanbrengen van ontwerpverbeteringen aan een robot, bij het voorspellen en het compenseren van de vervormingen van het eindpunt van een robot, en bij het bepalen, voor een bepaalde robottaak, van de beste robothouding en de beste positie van het werkstuk met betrekking tot de robotarm. Voor deze laatste toepassing laat het programma, dat werd ontwikkeld binnen deze verhandeling, toe om het ruimtelijke vervormingsgedrag van de robot binnen zijn werkruimte te

analyseren.

De toepassing van de proefondervindelijke, quasi-statische soepelheidsanalyse op een éénzijdig, ingeklemde balk heeft aangetoond dat de haalbare nauwkeurigheid van deze methode heel groot is. De toepassing van deze methode op een industriële robot heeft aangetoond dat deze methode heel geschikt is voor het bepalen van de soepelheidswaarden van de gewrichten van de robot. Het bepalen van de soepelheidswaarden van de gelederen van de robot en van de robotbasis leverde echter geen goede resultaten op. Door bij het quasi-statisch meten gebruik te maken van rotatieversnellingsopnemers, naast de reeds gebruikte translatieversnellingsopnemers, zou dit probleem opgelost zijn en zou deze methode ook goede reslutaten moeten geven voor de soepelheidswaarden van de gelederen van de robot en van de robotbasis. De recent op de markt verschenen rotatiebewegingsopnemers zijn echter niet geschikt voor dit type van toepassing.

Deze verhandeling toont ook de uitvoerbaarheid aan om op basis van rekstrookjes en op basis van optische opnemers een meetsysteem te bouwen dat in staat is om *on-line* de *ruimtelijke* vervormingen van een robotgelid te meten. De resultaten van de praktische toepassing van het op rekstrookjes gebaseerde vervormingsmeetsysteem tonen aan dat het meten van de vervormingen van een robotgelid gebaseerd op rekstrookjesmetingen niet de meest ideale methode is. Daarentegen, tonen de resultaten van de praktische toepassing van het op optische opnemers gebaseerde vervormingsmeetsysteem aan dat dit meetsysteem heel goed voldoet aan de kenmerken van het gewenste vervormingsmeetsysteem. Dit meetsysteem haalt een nauwkeurigheid die voor de verschillende opgemeten vervormingen varieert tussen 2% en 10%. Een deel van deze onnauwkeurigheid is te wijten aan de electronica die de analoge signalen, afkomstig van de optische opnemers, versterkt. Ook het on-line karakter van dit meetsysteem wordt aangetoond: het meten van de zes coördinaten en het berekenen van de vijf vervormingen hieruit vergt in het totaal, op een PC-AT!!!, minder dan $5ms$. Voor enkele toepassingen, waarin het voorgestelde op optische opnemers gebaseerde vervormingsmeetsysteem niet zou voldoen, worden enkele alternatieve meetsystemen voorgesteld.

What prevents the already long expected breakthrough of robots in industrial applications?

In the sixties and the seventies, robots were expected to make a great breakthrough in industrial applications. They were expected to replace all human interventions in industrial processes that were dangerous, tedious or imprecise. Except a few industrial branches, like the automotive industry, this breakthrough did however not happen yet. One of the biggest reasons for this failure to occur is undeniably the lack of accuracy which plague present day industrial robots. Besides, to keep this impreciseness to a minimum those robots are designed with very stiff links, which makes them very heavy and which limits their maximum speed very much. As "time is money", which is certainly the case in industry, also this limited speed of the robot contributes to this failure to occur.

The only answer to the problem of increasing the speed of robots are *lightweight* robots. The speed of these robots can be increased since there is less inertia. Reducing the weight and material needed for the robots lowers the overall cost. In addition, they require smaller actuators, and hence less power, and they are lighter to transport. This makes them very appropriate for space applications. A lightweight manipulator is also less hazardous since it carries less momentum and if it is elastic it may bend before breaking should it encounter an unforeseen obstacle. There will be more time to respond to emergencies

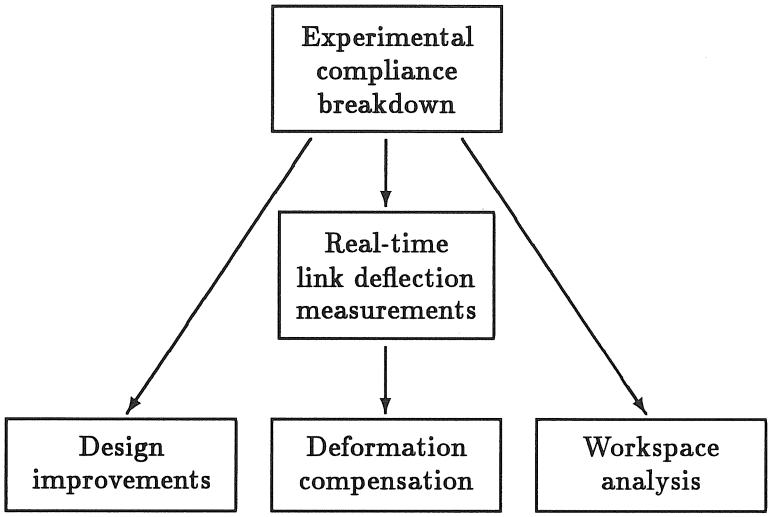

Figure: Some consecutive steps to realize accurate industrial robots.

and the impact of the collision will not be as serious. However, reducing weight and material reduces the rigidity of the robot links resulting in a less precise behaviour, or bigger deflections, of the robot under loading. As such, the flexibility of the robot links and joints, has to be considered in the control of the robot, statically as well as dynamically.

To develop very accurate industrial robots, robots should be optimally designed for stiffness. To realize this, methods should exist to identify the compliant components of the robot and to quantify their compliances. Once the robot has been optimally designed, the inevitable remaining deflections should be on-line compensated; statical as well as dynamical deformations should be treated. This thesis mainly considers statical deformations, but also it is tried to contribute as much as possible to the on-line compensation of the dynamical deformations. The figure on top of this page shows some consecutive steps necessary to realize very accurate industrial robots. For each of those steps, literature provides several methods. They all have their own advantages and drawbacks. Some of them are fairly simple whilst others are more complicated. In subsequent chapters those different steps are discussed more in detail.

The first chapter situates the reasons why the already long expected breakthrough of robots in industrial applications did not occur yet. A comparison is drawn between the accuracy of a robot and that of the human arm in spatial motion. As a result, some techniques to solve the deformation problem of robots are derived from the human use of additional feedback information. An overview of literature is presented for some of these techniques. For each of these techniques several methods are compared with each other and the most appropriate method is selected for further research.

The second chapter presents a *new* experimental method to identify the compliant components in a robot and to quantify their compliances. To perform an accurate compliance breakdown, this chapter introduces a *new* method to correct the influence of gravitation on translational accelerometer measurements. The experimental compliance breakdown method is discussed in detail and some error considerations on the experimental method are presented. The contribution of the results of the compliance breakdown to potential improvement of robot precision is briefly discussed in some applications (see figure on previous page). Finally, the experimental compliance breakdown method is applied in practice to a flexible beam and to an industrial robot. The experiment on the beam is intended to verify the accuracy of the compliance breakdown.

The third chapter deals with the real-time link deflection measurement. The measured deflections are those occurring at the tip of each flexible link. Two methods are investigated and tested for the desired features of a link deflection sensor. This link deflection measurement system should be able to determine in *real-time* the *spatial* structural deflections of a flexible link. First, a method is developed and verified to determine the structural deflections of a flexible link by means of strain gauges. The proposed theory has been verified on an experimental setup, and some conclusions were formulated. Based on these conclusions, the applicability of strain gauges for link deflection measurements is discussed. Secondly, a laser diode optical system is developed and verified for the real-time measurement of all spatial structural deflections of a flexible link. Different optical displacement transducers and light sources have been compared to determine which displacement transducer and which light source should be used in the link deflection measurement system. Based on the results of this com-

parison, a measurement setup is defined and the equations which define the relation between the structural deflections of the link and the optical displacement transducers measurements are determined. An accuracy analysis is carried out on the optical measurement system and the requirements for a practical optical measurement system are established. From the two proposed methods some alternative methods to build a link deflection measurement system are derived. Finally, to demonstrate the feasibility of the optical measurement system to determine in *real-time* the spatial structural deflections of a flexible link, an experimental optical link deflection sensor has been built and tested.

Chapter four summarizes the conclusions which have been drawn in the previous chapters, and checks how far the achieved results meet the requirements stated in the introduction chapter.

Appendix A derives a mathematical expression for the relation between the dynamic and static compliance behaviour of a mechanical system. Appendix B gives some theoretical backgrounds of homogeneous transforms. Appendix C describes a new method to correct the influence of gravitation on translational accelerometer measurements. Appendix D explains the Denavit-Hartenberg approach for representing the kinematics of lower-pair mechanisms. Appendix E gives a detailed description of the **ROBOFLEX** program, which has been developed within this thesis. Appendix F explains the basic features of laser theory that contribute to a better comprehension of this text. Appendix G contains definitions and detailed mathematical derivations in connection with the relation between the structural deflections of a flexible link and the measurements by the optical displacement transducers.

Chapter 1

Introduction and survey of literature

1.1 Introduction

The automated manufacture of high tolerance parts in small batch operations represents a major dilemma for the present level of manufacturing technology. High precision equipment is required to achieve the desired precision. However, small batch production necessitates easy reprogramming and multiple task handling capabilities. Robots partially solve this problem. Their high repeatability and simple reprogramming capabilities appear to bridge the gap between precision and task flexibility. However, as practice proved, repeatability does not imply precision under loading or during dynamic positioning. Due to their lack of precision, robots are used in simple repetitive tasks, such as spot welding, spray painting, and pick-and-place operations. Applications where accuracy under loading is necessary still belong to the future.

The lack of precision in most industrial robots is due to the deformation of the links and low stiffness in the drive components. This causes under load variable deformations not compensated for by the robot controller. Deformation of a robot is due to several loading factors working together; these include the loads applied to the end-effector from the payload statics and dynamics, and the interaction with the environment, static loads on the individual links due to gravity, and dynamic loading on the links due to the motion of the robot.

The significance of each loading factor varies from application to application.

The deformations themselves can be divided into two distinct types; static deformations, caused by external loads and inertial loads due to the motion of the arm, and small vibrations about the deflected equilibrium position. An important consideration for robot design and control is the relative magnitude of these two types of deformations. This research mainly considers static deformations.

The present approach to the deformation problem is to design manipulators with very stiff links. Dynamic effects are very small but the robot remains inaccurate and becomes very heavy. This results in 'slow' robots with a very high weight to payload ratio (20:1). For instance the KUKA IR 361/15.0 industrial robot weighs 300 kg and has a payload of 15 kg. A better approach to the deformation problem is to compensate the deformations in the robot control.

In industrial and space applications, lightweight robot manipulators are becoming increasingly important. The speed of robots can be increased since there is less inertia. Reducing the weight and material needed for the robots lowers the overall cost. In addition, they require smaller actuators, and hence less power, and are lighter to transport. This makes them very appropriate for space applications.

Reducing weight and material reduces the rigidity of the robot links. As such, the flexibility of the robot links has to be considered in the control of the robot. The flexibility of the lightweight link can be advantageous in certain applications. In positioning applications, for example inserting a bolt into a hole, the flexible link can compensate a certain amount of error in positioning. A lightweight manipulator is also less hazardous since it carries less momentum and if it is elastic it may bend before breaking should it encounter an unforeseen obstacle. There will be more time to respond to emergencies and the impact of the collision will not be as serious.

Increased precision through some means other than increasing the stiffness of the robot is obviously desired. The accuracy of the human arm in spatial motion is largely due to extraordinary hand-eye co-ordination. The eye acts as a feedback mechanism in the control loop of the hand. Unfortunately, the eye is not good at quantifying distances which renders it relatively imprecise and incapable of quantified motion. However, the basic answer to the deformation problem

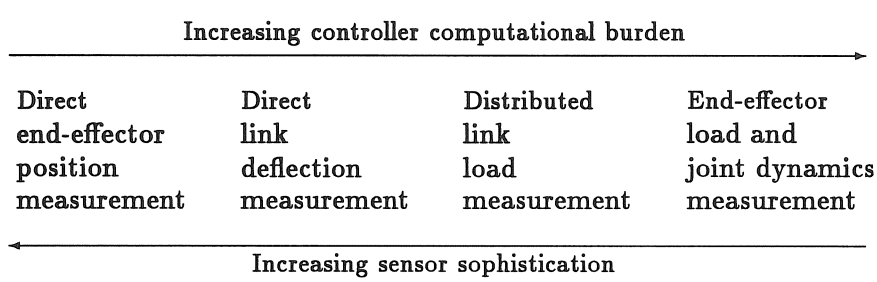

Figure 1.1: Sensor and controller correspondence for deflection compensation.

of robots can be derived from the human use of additional feedback information.

The amount of additional sensory input needed to achieve a deflection quantification tends to be inversely proportional to the amount of calculation required in the controller for the deflection model. Figure 1.1 [1] illustrates this concept. Shown is the spectrum from pure calculation of the end-effector deflection to completely external sensing of the end-effector position.

The most sensor intensive technique in figure 1.1 involves direct end-effector position measurement during task execution. This procedure does not rely upon the manipulator structure at all. Instead, optical sensors track the end-effector and triangulation returns the position of the end-effector in global coordinates [2, 3, 4]. This position allows simple computation of the positioning error from the desired value, which can be corrected by the robot actuators. However, current technology does not appear to fulfil this update requirement. In addition, optical methods severely limit the robot workspace since the end-effector may not be visually obscured from the sensors. Current systems are able to track the end-effector at low speed and within a restricted area of the robot workspace, and are used for robot calibration and performance measurements.

The next lower level of sensor technology is the direct measurement of the link deformations. In a subsequent chapter, a laser diode optical method is investigated for the real-time measurement of the spatial structural deflections of a flexible link (section 3.4). Flexibility of the

joint actuators needs separate consideration.

Distributed link load measurement implies measuring the actual load on the link and then calculating a deflection prediction. The load measurement can be achieved by using strain gauges distributed along the manipulator links. The loading on each individual link consists of a reaction force and moment from the succeeding link and distributed loading due to gravity and inertia. Since the strain gauges are actually measuring deflection, it may be possible to obtain an accurate deformation characterization from the distributed strain gauges. Such a strain gauge based method is investigated in section 3.3.

The final scheme suggested in figure 1.1 requires sensing the local reaction forces and moments from the end-effector and also the joint dynamic states (velocity and acceleration). Joint position and dynamic state information is then used as inputs to a dynamic and gravitational loading model. This model combined with the end-effector load information yields the reaction loads at each link [5]. These reaction loads along with a link and joint flexibility characterization in the form of local flexibility matrices will yield the total deformation of the robot. A method to determine accurately the local flexibility matrices of the different components of a specific robot system is developed in section 2.2. However, the technique presented in the final scheme is too time consuming for real-time implementation and is best used in the context of design development and workspace analysis, or to predict deformations due to known loads (section 2.3).

Real-time deformation compensation can be achieved by combining direct link deflection measurement and joint flexibility modelling. Section 2.3.2.2 deals with the real-time deformation control of flexible systems: static deformation compensation as well as vibration control.

Figure 1.2 gives a schematic overview of the proposed methods in this thesis. The numbers refer to the corresponding sections of this thesis, the arrows indicate the consecutive steps.

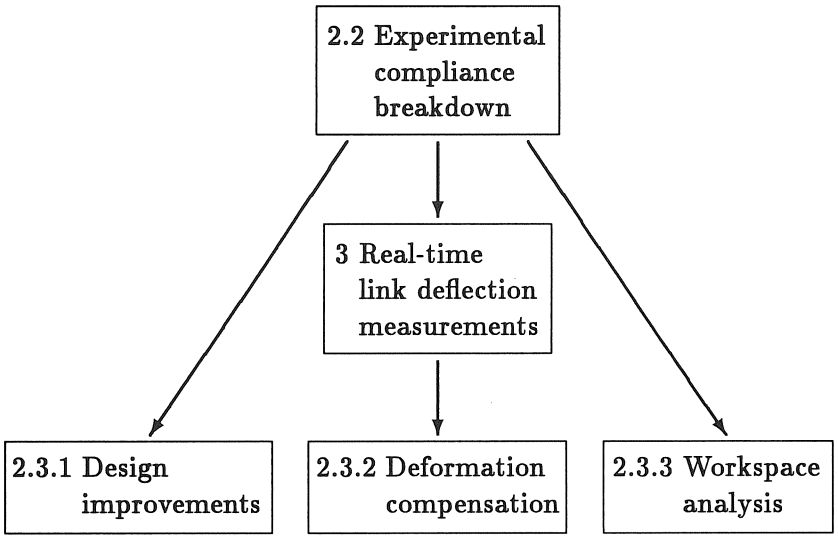

Figure 1.2: Schematic overview of proposed methods.

1.2 Experimental compliance breakdown of industrial robots

An important step in the compensation of robot deformations is the identification of the compliant components in the robot and the quantification of their compliance values. The compliance breakdown procedure must generate a fixed set of local flexibilities within the robot system which can be used to accurately predict the end-effector deformation due to an arbitrary load at any location within the robot workspace. The end-effector flexibility varies as a function of the arm configuration. This is therefore a position-dependent phenomenon and will be referred to as a global flexibility. The flexibility model parameters are normally position-independent quantities and are referred to as local flexibilities. Typically, individual units of identical robot models will have identical flexibility characteristics. Thus, this procedure is only required for a single unit and is likely an activity to be executed by a robot manufacturer or user. Both experimental and analytical techniques may be used to provide these parameters, however this research focuses on experimental techniques. RIVIN [6, 7] has developed analytical techniques for the different components of a robot.

In literature, several methods are proposed to identify experimentally the robot compliances: based on static, dynamic, holographic, and quasi-static measurements. The *quasi-static* approach is used exclusively in this research.

1.2.1 Static flexibility testing

To discover a model for joint compliance and link deformation for a six degrees-of-freedom robot, a Unimation PUMA 560, WHITNEY ET AL. [8, 9] use the setup shown in figure 1.3. Static forces are applied to the robot arm first at F_1 and then at F_2. Deflections are measured at positions $\otimes_i$ (i=1-7) using dial gauges. The resulting data are fitted to a model of rigid links connected by compliant joints that act as torsional springs of stiffness. Besides joint compliance, also backlash, robot base motion and some other effects are considered.

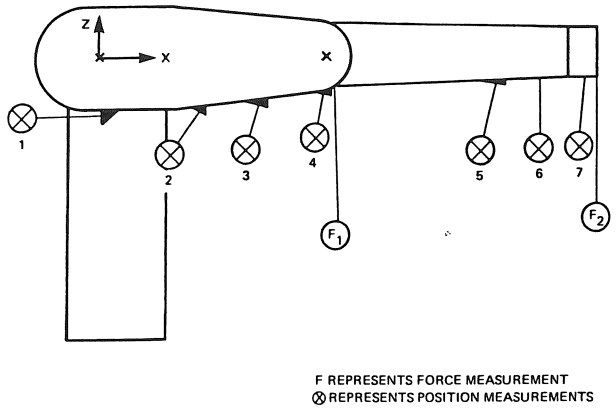

Figure 1.3: Measurement points for force deflection curves.

ELMARAGHY and JOHNS [10] apply in a first approach a static force directly to the end-effector and measure the corresponding displacements. The applied force is measured using a six-axis force sensor attached to the end-effector. The displacements, translational as well as the rotational, are measured using three dial indicators. Knowing these forces and displacements, the resulting torques and joint rotations are calculated using the Jacobian. Rotation is plotted versus torque for each joint where the slope of the line represents the joint compliance. The second approach avoids the use of the Jacobian by applying torques directly to the robot joints. This is done by loading

each joint at a known lever arm distance and measuring the resulting rotation by a dial indicator placed at known distance from the joint along the robot link. Both previous approaches only consider joint compliances.

LEU ET AL. [11] apply a static force directly to the end-effector and measure the total end-effector deflection. To estimate the end-effector deflections due to the link and the bearing deformations analytical techniques are used. The end-effector deflection due to the joint compliance is then the difference between the measured total deflection and the estimated deflections due to the link and bearing deformations.

Another approach is presented by SKLAR [12]. He determines the global compliance matrix by applying known directional loads at the end-effector and measuring the corresponding end-effector deformation. The precise load is measured using a six component force sensor, and the pose of the end-effector is determined by measuring the 3D co-ordinates of three established reference points using a 3D measurement system. This is done in a number of configurations of the robot arm, and the local link and joint flexibility constants are determined from analytic models relating the local and global flexibilities. Unfortunately, the consistency of the predicted models is poor. This is due to errors in the global matrices, due to the problem of applying pure torques, and the inability of the least-squares algorithm to solve the equations adequately, due to the complex dependencies that exist between the different columns of the matrices.

Two methods can be distinguished to perform a static analysis of all components within the structure's flux of force:

- direct measuring of the local deformations, (WHITNEY, LEU, ELMARAGHY, ...),
- measuring of the global compliance matrix followed by a calculation of the local, component flexibilities from analytic models relating the local and global flexibilities (SKLAR).

The direct measuring method is only possible with extensive experimental expense. In order to determine the deformation and displacement of a component it is indispensable to surround the structure being examined with a measuring scaffold constructed from pipe elements, and to detect the deformation relative to the measuring stand

at the structural points with appropriate measuring devices. Thermal displacements of the measuring scaffold, floor vibrations, and not to be forgotten, measuring stand deformation, considerably increase the measuring precariousness of this procedure. The global measuring method avoids the use of a measuring scaffold but the consistency of the predicted models is poor.

1.2.2 Dynamic flexibility testing

TLUSTY and STERN [13, 14] use modal analysis techniques to determine directly the flexibility in a robot. Transfer functions are measured by accelerometers at various points of the structure and are obtained by impacts by an instrumented hammer. The measurements are so arranged as to obtain a dynamic model of the structure as an assembly of springs, masses and dampers as it responds to external forces. This identification is based on the extensive lumped-mass vibrational model of a robot developed by BEHI [15]. This technique provides both the flexibility and the mass content parameters.

Using modal analysis techniques to determine robot flexibilities reduces the experimental expense considerably. This method needs an accurate, and extensive, dynamic model of the structure covering all dynamic, and static, effects. The biggest problem is the accurate identification of the many parameters of the dynamic model, which all influence the value of the desired flexibilities.

1.2.3 Holographic flexibility testing

KURTOGLU [16, 17] uses holographic interferometry to investigate the load-induced flexibility of the mechanical construction of a robot. Holographic interferometry is used to measure because of its ability to measure simultaneously and with great accuracy the deformation of every visible point on the total robot. A multitude of holograms are made recording the displacement that occurred as forces are applied to different configurations of the robot. Its true behaviour is thereby revealed and can be studied analytically. The displacement patterns of individual elements are recorded in detail.

Holographic interferometry not only permits to obtain flexibility information but also the deformation patterns of the different components. However, holographic interferometry needs very specialized,

and expensive, equipment and the translation of the multitude of deformation patterns to numerical flexibility data is not so obvious. If bendings are small, it becomes impossible to detect them by an ocular observation and the bending curvature cannot be calculated.

1.2.4 Quasi-static flexibility testing

WECK and ECKSTEIN [18, 19, 20] provide a quick examination technique to determine the static load-deformation behaviour of complex mechanical structures, especially of machine tools. Contrasting existing methods, it is not only possible to measure the summarized stiffness at the cutting location but also to describe the static deformation of the complete machine structure. On the basis of a quasi-static force, which is a sinusoidal force with a frequency far below the first natural frequency, the acceleration at certain points of the structure is measured absolutely. With these data it is possible to determine the displacement quotas of the different components within the machines flux of force.

With the aid of the quasi-static technique the expense required for determining the load-deformation behaviour of complex mechanical structures, including industrial robots, and their components, can be considerably reduced. This technique is largely based upon modal analysis techniques used to investigate the structures dynamic behaviour.

1.2.5 Conclusion

Quasi-static flexibility testing seems to be the most appropriate method to determine the compliance model of a complex mechanical structure, such as an industrial robot. In section 2.2 the quasi-static technique of WECK and ECKSTEIN is adapted to be able to determine *configuration-independently* the compliances of the different components of an industrial robot. This new method permits to determine the compliances of a component without measuring the whole robot. The results of this compliance breakdown contribute to potential improvement of robot precision in several ways; such as in robot design improvement, in prediction and compensation of robot-endpoint deflection, in selection of best robot posture and best workpiece position with respect to the robot arm for a given task.

1.3 Real-time link deflection measurements

To control the structural deflections and vibrations of flexible manipulators, the knowledge of the position of the end-effector or of the tip of the flexible link is essential [21].

Knowing the position of the end-effector, all deflections, backlash, and other error sources of the manipulator can be compensated [2, 3, 4]. However, systems measuring dynamically the position of the end-effector are difficult to develop because high accuracy three-dimensional position and orientation measurements must be made over a large operating volume.

End-point feedback can be avoided if a sufficiently detailed dynamic model of the manipulator structure can be developed and calibrated [22]. However, such a model would be extremely complex even if low order beam models were used, and would suffer from the need to be recalibrated for every new position of the manipulator since most robots have a variable structure.

Accordingly, this research addresses a different approach to the problem of control of structural deflections and vibrations of flexible manipulators, and concentrates on the measurement of the errors caused by structural deflections of flexible links. Knowing the position of the tip of a flexible link, all structural deflections and vibrations of that link can be compensated.

In literature, several schemes are proposed to measure the position of the tip of a flexible link. The position of the tip of a flexible link can be determined by using the information of the encoder and by measuring the structural deflections at the tip of the link. Capacitive detectors, strain gauges and optical detectors are devices that have been used to measure the deflection of the link. In a subsequent chapter, strain gauges and optical detectors are investigated.

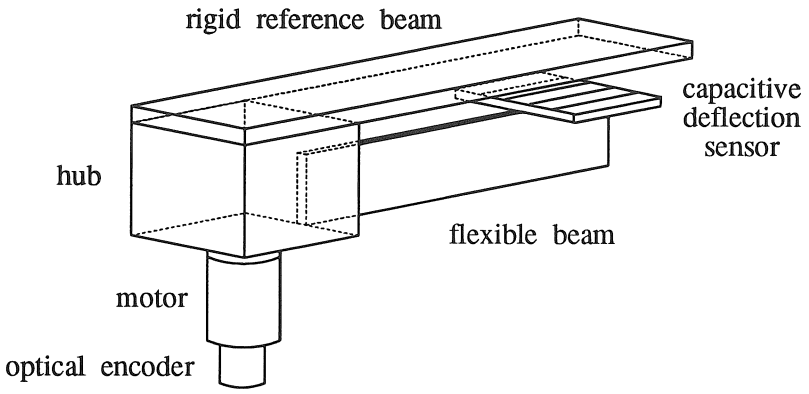

Figure 1.4: Capacitive link deflection sensor.

1.3.1 Capacitive deflection measurements

RAMAKRISHNAN [23] uses the capacitive encoder principle [24] to measure the link deflection. The link deflection sensor is shown in figure 1.4. His scheme involves attaching a separate "rigid" beam to the flexible arm. A thin, wide beam made of fibreglass is used as the reference "rigid" beam attached to the motor shaft. A small sensor plate is rigidly attached to the tip of the flexible beam so that the relative displacement of the sensor plate (and thereby the position of the tip of the beam) with respect to the reference beam can be measured. This gives the beam deflection. Hence the position of the tip of the beam can be obtained by adding the rigid body rotation and the deflection vectorially.

The advantage of this scheme is that it can measure the deflection anywhere in the range of motion of the link. The disadvantage is that the motor would have to carry the additional load of the reference beam.

1.3.2 Strain gauges based deflection measurements

SWEVERS ET AL. [25, 26, 27, 28] and BOOK ET AL. [29] use feedback control based on strain gauges measurements to damp out the vibrations of a flexible arm. Feedback depends on the measurement of variables from which the state of the arm can be determined. Joint position and velocity measurements are important, but even with a

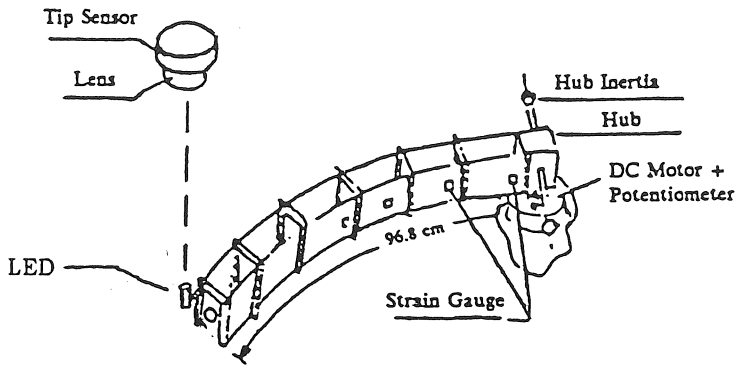

Figure 1.5: Optical link deflection sensor.

slight amount of Coulomb friction, unwanted vibrations can exist that cannot be detected in these measurements. A number of strain gauge measurements are used to reconstruct the same number of flexible shape amplitudes directly.

Strain gauges are relatively inexpensive and well known and have been used effectively. However, they have the disadvantage of not measuring the deflection directly. The structural deflections at the tip of the link have to be calculated from measurements at several points on the link. This results in more complex computation, and possibly lower accuracy. As such, more direct methods of measuring the structural deflections have to be considered.

1.3.3 Optical deflection measurements

CANNON and SCHMITZ [21] use an optical photodetector to measure the position of the tip of the link directly (figure 1.5). In their case, a small light bulb is attached to the tip of the link for optical sensing of the tip position. The tip sensor consists of a focusing lens $1\,m$ above the tip's light bulb and, behind the lens, a photodetector is used to detect the position from the light spot created by the light bulb. Hence the tip position can be measured directly.

The disadvantage is that the range is limited to motion of the arm $\pm 40\,cm$ about the centre line. But the important drawback of this scheme is that either the light source or the sensor must be attached to a known reference. For a single link, a set of light sources or sensors can be positioned along the perimeter of a circle. But if the manipulator

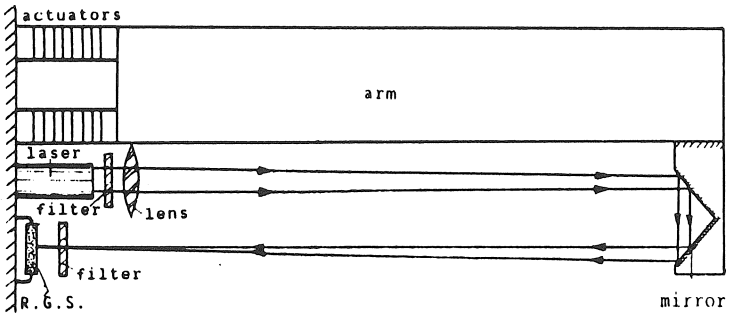

Figure 1.6: Optical link deflection sensor.

has more than one flexible link, the placement of the sensor becomes a problem. Because one of the goals of this thesis is to implement a sensing scheme that can monitor the deflections of any link in a multi-link manipulator, the scheme of CANNON and SCHMITZ cannot be used.

ZALUCKY and HARDT [30] propose an optical displacement sensor to measure the bending deflections of a beam. However, for simplicity and ease of construction, they consider only one bending axis and use an displacement transducer rather than the beam straightness measurement.

MULDERS ET AL. [31] measure the position of the free end of a robot arm, namely the deviation in x- and y-direction, by using a laser system. These deviations have to be measured in spite of the bending of the end of the arm. Figure 1.6 shows the optical link deflection sensor. The source of this deflection sensor is a semiconductor laser mounted at the fixed end of the robot arm. The transmitted laser beam is conducted through lenses for collimating and converging, and is reflected by a special mirror, a retroreflector, mounted at the free end of the robot arm. The retroreflector has the special property that only the translation and not the rotation of this mirror effects the reflected laser beam. Finally, the reflected laser beam is detected in a resistive gate sensor of 200×300 pixels. A filter reduces the energy of the laser beam for the resistive gate sensor to the allowable amount. In this way, the position of the free end of the link can be determined.

The disadvantages are that the detection of the position of the laser beam in the matrix of pixels is time-consuming, about $20\,ms$,

and that system is only able to measure the x- and y-deviation, and no deformation angles.

UCHIYAMA and KONNO [32] present a laser optical method to measure the *spatial* structural deflections of a flexible link of a robot. The deflections which it measures are those at the tip of each link. The system consists of three semiconductor lasers and three position sensitive detectors (PSD's). The laser diodes are mounted on one end of the link, and the PSD's on the other end. The PSD is of a planar type and measures the position co-ordinates of the laser spot on the sensor surface. The deflections are calculated from the co-ordinates measured by the PSD's.

This method determines all structural deflections, except for the elongation of the link and the sign of the two structural bending angles. Up to now, their experimental set-up is restricted to the measurement of one-degree-of-freedom deflections.

PREVOST and PAVLIN [33] present an optical process proper to the measurement of structural deflections of robot manipulators. The rigid structure of the robot is idealized by an optical skeleton, which consists of light beams emitted by a HeNe laser linked to the base frame of the robot (cf. figure 1.7). Quadrant detectors, indicated by C in the figure, linked to the link at various locations, give a measure of the deflections of the link resulting from structural bendings and torsions. For the whole robot, the implementation of such a light reference requires the use of precisely tuned mirrors, indicated by M in the figure, to deviate the laser beam at each joint.

The disadvantages of this system are mainly:

- the introduction of many tuning points: mirror parallelism, detector alignment, ...;
- a large computation time: it takes $20ms$ with a 80386 microprocessor system to calculate the deflections of a three degree-of-freedom robot;
- a high cost, because of the optical devices and precision mechanics involved.

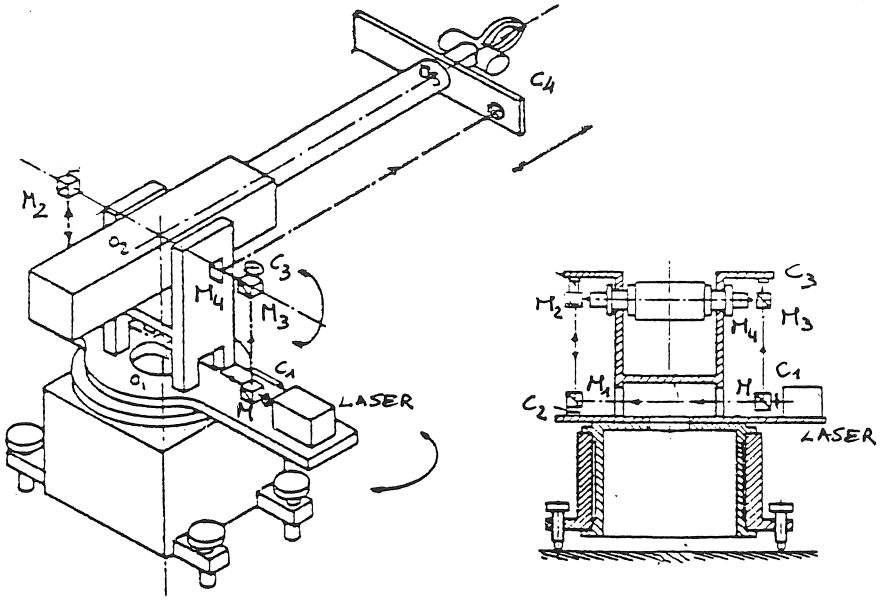

Figure 1.7: Optical skeleton.

1.3.4 Conclusion

In summary, the link deflection sensor system should have the following features. It should:

1. measure in *real-time* all *spatial* structural link deflections;
2. measure the link deflections accurately and with minimum computation;
3. measure deflections anywhere in the range of motion of the link;
4. preferably have a digital output to speed up subsequent computations;
5. enable to build in the link deflection sensor system inside a robot arm;
6. be easy to calibrate;
7. be of reasonable cost.

Optical detectors seem to be the most obvious devices to meet most of this features. In section 3.4 a laser diode optical method is presented for the *real-time* measurement of all spatial structural deflections of a flexible link, except for the elongation of the link. Neglecting the elongation causes no real error. The system consists of three semiconductor laser diodes and three PSD's, one mounted in the focal plane of a lens. The laser diodes are mounted at one end of the link, and the PSD's at the other end.

This laser diode optical system has been developed apart from the system of UCHIYAMA and KONNO, and has the following advantages:

- it is able to determine also the sign of the two structural bending angles;
- an experimental set-up has been developed which measures all *spatial* structural deflections in *real-time*.

If however the cost of the sensor system is a decisive feature, or if very big deformations have to be measured, strain gauges become very useful devices. The applicability of strain gauges to build a link deflection sensor is investigated in section 3.3.

1.4 Conclusion: formulation of the problem

To realize the already long expected, and until now highly overrated, breakthrough of robots in industrial and space applications, industrial robots should meet certain requirements: robots should be highly accurate, even in applications where accuracy under loading is necessary, and robots should become very fast. Lightweight robots are the only answer to the problem of increasing the speed of robots, however reducing weight and material of the robot also reduces the rigidity of the robot links which results in a less precise behaviour, or bigger deflections, of the robot under loading. The solution to both problems is to build lightweight robots:

- which are optimally designed for stiffness;
- with all inevitable deflections on-line compensated.

To optimally design a robot for stiffness, or improve the design of an existing or prototype robot, the compliant components of the robot

should be identified and their compliances should be quantified. This is called the compliance breakdown of a robot. There exist already some methods to identify and quantify experimentally the compliances of complex mechanical structures. However, specific for robots, these methods

- take a lot of time and are very expensive;
- are only able to measure the summarized stiffness at the end-effector of the robot;
- are only able to determine the compliances of the different components of a complex mechanical structure for a specific configuration, which is especially for fast changing configurations as robots insufficient.

Once the robot has been optimally designed for stiffness, the inevitable remaining deflections should be compensated. The compensation of the deflections based on a compliance model, eventually derived by an experimental compliance breakdown, is only feasible for off-line compensation. However, for many applications, such as all sensor based applications, only on-line position and force information is available and off-line compensation becomes impossible. For on-line compensation, compensation based on a compliance model of the robot is not feasible. Therefore on-line compensation needs to be based on on-line deflection measurements. Ideally, these measurements should be direct end-effector position measurement during task execution. However, current, and near future, technology does not appear to fulfil this update requirement. Measurements which involve a lower level of sensor technology, but which are much more realistic, are direct link deflection measurements. Several methods have already been investigated, but they all are deficient in performing *real-time, spatial* link deflection measurements.
In conclusion, the problem may be stated as follows:

1. develop a method to identify and to quantify **experimentally** and **configuration-independently** the compliances of **all components** of complex mechanical structures, *especially of industrial robots.*
2. develop a sensor system which is able to determine in **real-time** the **spatial** structural deflections of a link of a robot.

Chapter 2

Experimental compliance breakdown of industrial robots

2.1 Introduction

An important step in the improvement of robot precision is the identification of the compliant components in the robot, and the quantification of their compliances.

Section 1.2 has shown that quasi-static compliance breakdown is the most appropriate method to determine the compliance model of a complex mechanical structure, such as an industrial robot. In this chapter the quasi-static technique of WECK and ECKSTEIN is adapted to be able to determine *configuration-independently* the compliances of the different components of an industrial robot. This new method permits to determine the compliances of a component without measuring the whole robot. The results of this compliance breakdown contribute to potential improvement of robot precision in several ways; such as (1) in robot design improvement, (2) in the prediction and compensation of robot end-point deflection, or (3) in the selection of, for a given task, best robot posture and best workpiece position with respect to the robot arm, based upon a workspace analysis.

2.2 Quasi-static compliance breakdown

Quasi-static compliance breakdown consists of two consecutive steps. First, a quasi-static measurement is carried out to measure the displacements of the planes characterizing the different components of the robot within the flux of force. Afterwards, the compliances of the measured components based on the previous measured data are measured. Some precautions to prevent errors occurring during both steps are discussed in a separate section.

2.2.1 Quasi-static measurement

The quasi-static measurement method is developed on the basis of modal analysis techniques. To measure the *static* compliance behaviour of a mechanical system, the system is excited with a sinusoidal excitation force with an excitation frequency far below the first natural frequency of the system. At certain points of the system the accelerations (with respect to a stationary reference frame connected to the robot base) are measured. With these data it is possible to determine the compliances of the different components within the flux of force. This method will be explained more in detail in the following paragraphs.

Figure 2.1 shows the frequency response of a flexible clamped-free beam (cf. section 2.4.2.5). The static compliance is evidently to be found at a frequency of $0Hz$. The frequency up to which the dynamic and static compliance behaviour are in a first order identical characterizes the *quasi-static range*. The more detailed figures at the right point out that between $4Hz$ and $8Hz$ the magnitude of the compliance remains nearly constant, and the phase between force and displacement represents with a level of $0°$ the static case. Low frequencies, less than $2Hz$, pose a limitation. This phenomenon is caused by the roll-off at low frequencies of the electromagnetic vibration exciter, and by the low acceleration level at those frequencies. Disregarding this disturbance at lower frequencies, the magnitude of the compliance within the quasi-static range represents the static compliance. The quasi-static range defines the frequency f_{qs} of the quasi-static force F_{qs} to be applied to the system. Appendix A derives a mathematical expression to choose for a desired accuracy the frequency f_{qs} with respect to the

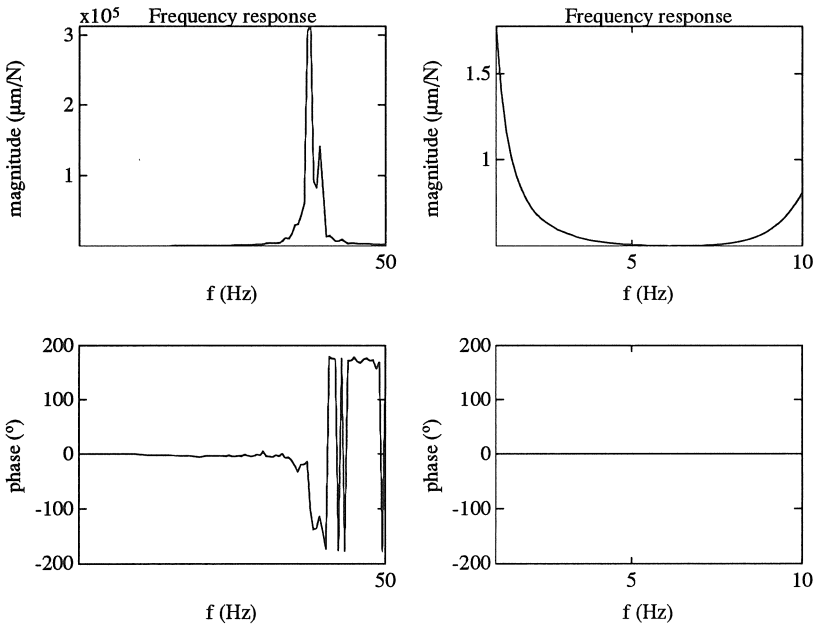

Figure 2.1: Determination of the quasi-static range.

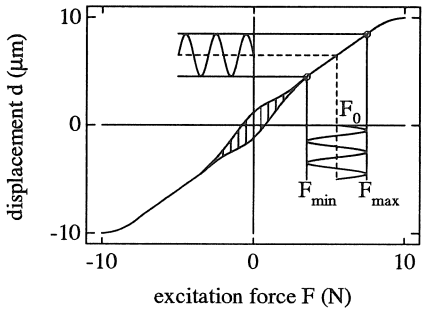

Figure 2.2: Measurement of the summary static compliance.

corresponding first natural frequency of the considered system.

To carry out the measurements on the system within its range of linear elastic behaviour, also the magnitude of the quasi-static force should be well chosen. Figure 2.2 shows an example of a global stiffness characteristic. The measured stiffness characteristic is characterized by a non-linear and a linear section, and by hysteresis. The linear section is of interest for the measurement method. The hysteresis is due to backlash and friction. To measure within the linear range of the stiffness characteristic, a static preload is necessary. The magnitude of the static preload F_0 is defined by

$$F_0 = \frac{F_{min} + F_{max}}{2}, \tag{2.1}$$

where F_{min} is the limit of the linear section, and F_{max} the maximal permissible load. The magnitude of the sinusoidal part of the quasi-static force F_a is restricted by the linear section:

$$F_a \leq \frac{F_{max} - F_{min}}{2}. \tag{2.2}$$

The resulting quasi-static force F_{qs} is shown in figure 2.2, and is defined as:

$$F_{qs} = F_0 + F_a \sin(2\pi f_{qs} t). \tag{2.3}$$

The measurement of the compliance frequency response, and the global stiffness characteristic of the system is necessary at each new excitation location to define the appropriate quasi-static force F_{qs}.

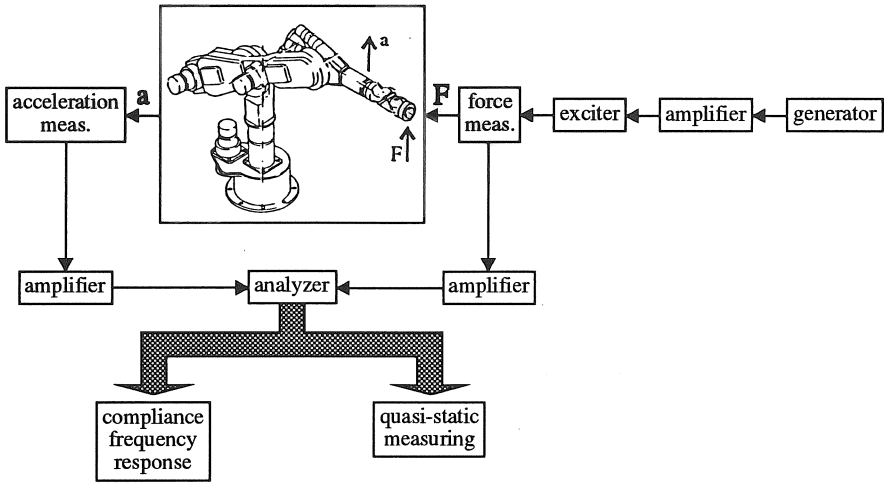

Figure 2.3: Equipment for the quasi-static measurement.

On the basis of the quasi-static force excitation the accelerations at certain points of the robot are measured. The corresponding displacements d_{qs} are sinusoidal with the same frequency f_{qs}, because of the linear elastic behaviour of the system:

$$d_{qs} = d_a \sin(2\pi f_{qs} t + \varphi). \tag{2.4}$$

Theoretically, the phase φ between the quasi-static force and the displacement is 0°. The magnitude of the displacement d_a is derived by integrating twice the magnitude of the measured acceleration $\ddot{d}_a$:

$$d_a = -\frac{\ddot{d}_a}{(2\pi f_{qs})^2}. \tag{2.5}$$

Figure 2.3 illustrates the required setup for measuring the quasi-static load-deformation behaviour. A vibration exciter, controlled by a generator, introduces low frequency, with respect to the first natural frequency of the considered robot, sinusoidal forces at the robot end-effector. The accelerations, measured at predefined structural points, and the force signals are led to an analyzer which converts simultaneously the analog signals to their digital value. Based on a least squares approximation at the considered frequency and for a number

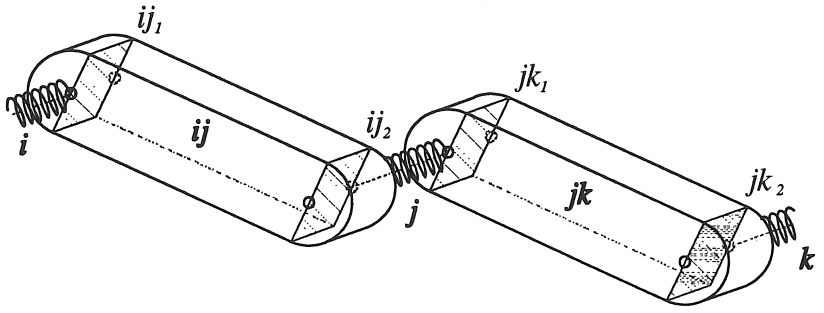

Figure 2.4: Reference planes characterizing compliant parts.

of repeated measurements the analyzer determines the magnitude and the phase dependent behaviour of the displacements and the forces. Within the analyzer the measured displacements are assigned to the structural points of the robot, and the forces are assigned to the excitation point. The analyzer consists of a multi-channel data acquisition system linked to a microcomputer.

2.2.2 Compliance breakdown

To determine the exact static load deformation behaviour of a robot end-effector, a method to locate the static compliances is necessary. This method should be able to determine the link and joint compliances independent from the robot configuration. The compliance breakdown method proposed within this section is based on the measurements carried out by the quasi-static measurement, which has been discussed in the previous section, and is realized by the same microcomputer.

2.2.2.1 Compliance modelling

To carry out a compliance breakdown of a robot, compliant components are characterized by two reference planes, considered as being rigid; a plane just before the considered component, and another just after.

Links can be modelled as long, symmetric beams. Figure 2.4 shows the two reference planes ij_1 and ij_2 which characterize link ij.

If $\mathcal{D}_{ij}$ stands for the link deformation, and $\mathcal{F}_{ij}$ stands for the generalized force vector applied at the tip of link ij; with

$$\mathcal{D}_{ij} = \begin{bmatrix} \mathbf{d}_{ij} \\ \mathbf{a}_{ij} \end{bmatrix}, \tag{2.6}$$

$$\mathcal{F}_{ij} = \begin{bmatrix} \mathbf{f}_{ij} \\ \mathbf{m}_{ij} \end{bmatrix}, \tag{2.7}$$

where $\mathbf{d}_{ij}$ and $\mathbf{a}_{ij}$ are the translations along and the rotations about the proper axes of the frame at the tip of the link, and $\mathbf{f}_{ij}$ and $\mathbf{m}_{ij}$ are the forces along, and the moments about the proper axes of the same frame, then the relation between the link deformation and the forces applied at the tip of the link is given by:

$$\mathcal{D}_{ij} = \mathbf{C}_{ij}\, \mathcal{F}_{ij}, \tag{2.8}$$

where $\mathbf{C}_{ij}$ is the compliance matrix of the link. The standard beam theory [34] provides following compliance matrix $\mathbf{C}_{ij}$:

$$\mathbf{C}_{ij} = \begin{bmatrix} c1_{ij} & 0 & 0 & 0 & c7_{ij} & 0 \\ 0 & c2_{ij} & 0 & c8_{ij} & 0 & 0 \\ 0 & 0 & c3_{ij} & 0 & 0 & 0 \\ 0 & c8_{ij} & 0 & c4_{ij} & 0 & 0 \\ c7_{ij} & 0 & 0 & 0 & c5_{ij} & 0 \\ 0 & 0 & 0 & 0 & 0 & c6_{ij} \end{bmatrix}. \tag{2.9}$$

The compliance of link ij is defined by 8 parameters $(c1_{ij}, \ldots, c8_{ij})$.

Joints can be modelled as torsion springs or as linear springs, depending on the type of joint. The two reference planes which characterize joint j are the planes ij_2 and jk_1 (figure 2.4). The joint compliance can be represented by a single compliance constant c_j, representing the compliance of the equivalent spring. The other compliances of the joint are considered negligible with respect to this compliance. If j is a revolute joint, the joint deformation is given by the scalar equation

$$\Delta\theta_j = c_j\, M_{z_j}, \tag{2.10}$$

where $\Delta\theta_j$ is the angular joint deformation, and M_{z_j} is the moment about the motion axis of the joint; if j is a prismatic joint, the equation becomes

$$\Delta d_j = c_j\, F_{z_j}, \tag{2.11}$$

where Δd_j is the linear joint deformation, and F_{z_j} is the force along the motion axis of the joint.

To provide a uniform analysis with the link compliance, the joint compliance matrix $\mathbf{C}_j$ is defined as

$$\mathbf{C}_j = \begin{bmatrix} 0 & 0 & 0 & 0 & 0 & 0 \\ 0 & 0 & 0 & 0 & 0 & 0 \\ 0 & 0 & (1-\delta)\, c_j & 0 & 0 & 0 \\ 0 & 0 & 0 & 0 & 0 & 0 \\ 0 & 0 & 0 & 0 & 0 & 0 \\ 0 & 0 & 0 & 0 & 0 & \delta\, c_j \end{bmatrix}, \tag{2.12}$$

where $\delta = 0$ if j is prismatic, and $\delta = 1$ if j is revolute.

This joint compliance is due to the compliance of the mechanical transmission between the actuator and the joint. The robot controller introduces also some supplementary joint compliance, however generally this contribution is negligible with respect to the compliance due to the transmission, especially since the *static* load-deformation is considered. Therefore, the joint compliance is measured with the brakes on, and the robot controller off.

In practice, the joint compliance cannot always be represented by a single compliance constant c_j. The joint compliance c_j can change with the joint angle. The quasi-static measurement method solves this problem by measuring c_j for different joint angles. Tabulating these results gives for each joint angle the corresponding joint compliance.

Quasi-static measurement also permits to model the compliance of the *base*. The base compliance matrix $\mathbf{C}_b$ depends on the type of base. The two reference planes characterizing the base are a plane attached to the world, considered immovable, and a plane B coinciding with the mounting plate of the robot. Contrary to the compliances of the links and the joints, the compliance of the base is not independent of the robot installation. The base compliance should be redefined for each new robot installation.

2.2.2.2 Reference plane movement

A reference plane, W, characterizing the compliant components, is defined by, at least, three non-collinear structural points P_i (figure 2.5). The sinusoidal accelerations are measured at the structural points P_i in

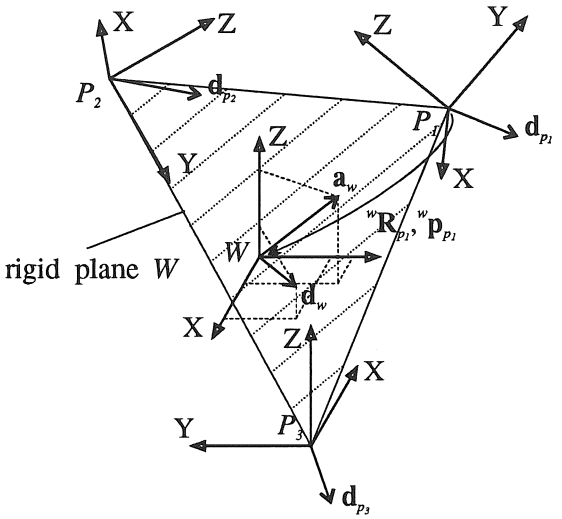

Figure 2.5: Movement of a reference plane.

three perpendicular directions. Integrating the considered acceleration component twice gives the components of the displacement vector $\mathbf{d}_{p_i}$. The absolute movement of the reference plane W, $\mathcal{D}_w$ (equation 2.6), is solved using the different displacement vectors $\mathbf{d}_{p_i}$.

Four co-ordinate frames are drawn in figure 2.5. The co-ordinate system $\{XYZ_w\}$ represents the reference plane W. The co-ordinate frames $\{XYZ_{p_i}\}$ represent the structural points P_i, belonging to the plane W. The position and orientation of the point frame $\{XYZ_{p_i}\}$ with respect to the plane frame $\{XYZ_w\}$ is described by the homogeneous transform ${}^w\mathbf{A}_{p_i}$ (appendix B):

$$ {}^w\mathbf{A}_{p_i} = \left[\begin{array}{ccc|c} & {}^w\mathbf{R}_{p_i} & & {}^w\mathbf{p}_{p_i} \\ \hline 0 & 0 & 0 & 1 \end{array}\right], \tag{2.13} $$

where ${}^w\mathbf{R}_{p_i}$ is the orientation matrix and ${}^w\mathbf{p}_{p_i}$ the position vector.

If the plane W undergoes a movement $\mathcal{D}_w$, the displacement vector in a point P_i, defined in the plane frame $\{XYZ_w\}$, is given by

$$ (\mathbf{d}_{p_i})_w = \mathbf{d}_w + \mathbf{a}_w \wedge {}^w\mathbf{p}_{p_i}, \tag{2.14} $$

where $\wedge$ denotes the cross product of two vectors, and

$$(\mathbf{d}_{p_i})_w = {}^w\mathbf{R}_{p_i}\ \mathbf{d}_{p_i}. \tag{2.15}$$

The absolute movement of the reference plane W, $\mathcal{D}_w$, is found solving following equation:

$$\begin{bmatrix} \mathbf{I}_3 & {}^w\mathbf{K}_{p_1} \\ \mathbf{I}_3 & {}^w\mathbf{K}_{p_2} \\ \mathbf{I}_3 & {}^w\mathbf{K}_{p_3} \end{bmatrix} \mathcal{D}_w = \begin{bmatrix} (\mathbf{d}_{p_1})_w \\ (\mathbf{d}_{p_2})_w \\ (\mathbf{d}_{p_3})_w \end{bmatrix}, \tag{2.16}$$

where $\mathbf{I}_3$ is the 3×3 unity matrix, and

$$\begin{aligned} {}^w\mathbf{K}_{p_i} &= \begin{bmatrix} \mathbf{x}_w \wedge {}^w\mathbf{p}_{p_i} & \mathbf{y}_w \wedge {}^w\mathbf{p}_{p_i} & \mathbf{z}_w \wedge {}^w\mathbf{p}_{p_i} \end{bmatrix}, \\ &= \begin{bmatrix} 0 & ({}^w\mathbf{p}_{p_i})_z & -({}^w\mathbf{p}_{p_i})_y \\ -({}^w\mathbf{p}_{p_i})_z & 0 & ({}^w\mathbf{p}_{p_i})_x \\ ({}^w\mathbf{p}_{p_i})_y & -({}^w\mathbf{p}_{p_i})_x & 0 \end{bmatrix}. \end{aligned} \tag{2.17}$$

Due to the influence of gravitation on the translational accelerometer measurements, equation 2.14 needs to be corrected as given in appendix C. The author is not aware of the existence of any other method which compensates the influence of gravitation on translational accelerometer measurements, although it is essential to derive the *correct* absolute movement of the reference plane W. In fact, all people using translational accelerometer measurements encounter this phenomenon, but as they measure at higher frequencies they neglect, in many cases without knowing, this influence.

Equation 2.14 becomes:

$$\begin{aligned} (\mathbf{d}_{p_i})_w &= \mathbf{d}_w + \mathbf{a}_w \wedge {}^w\mathbf{p}_{p_i} + \mathbf{a}_w \wedge {}^b(\mathbf{d}_g)_w, \\ &= \mathbf{d}_w + \mathbf{a}_w \wedge \left({}^w\mathbf{p}_{p_i} + {}^b(\mathbf{d}_g)_w\right); \end{aligned} \tag{2.18}$$

with

$$\begin{aligned} {}^b(\mathbf{d}_g)_w &= \frac{g}{\omega_{qs}^2}\,({}^b\mathbf{r}_{\mathbf{3}w})^t, \\ \omega_{qs} &= 2\pi f_{qs}; \end{aligned}$$

where : g : gravitational acceleration $(9.81\frac{m}{s^2})$;
f_{qs} : quasi-static frequency;
${}^b\mathbf{r}_{\mathbf{3}w}$: third row of ${}^b\mathbf{R}_w$, the orientation matrix of the reference plane frame with respect to the robot base frame.

The absolute movement of the reference plane W, $\mathcal{D}_w$, is then found solving equation 2.16 with the substitution of

$$^{w}\mathbf{p}_{p_i} \qquad \text{by} \qquad ^{w}\mathbf{p}_{p_i} + {}^{b}(\mathbf{d}_g)_w$$

in equation 2.17.

2.2.2.3 Compliances calculation

To calculate the compliances of compliant components, the forces acting on the compliant component, and the resulting deformation of the compliant component are necessary (cf. equations 2.8, 2.10, 2.11).

The forces acting on a compliant component of a robot consist of three components, due to

- the robot end-effector loads,
- the gravity working on the following components, and
- the inertia of the following components.

The gravity forces should not be taken into account for the quasi-static measurement. They are dc-components, and can be considered as an additional static preload. Only ac-components contribute to the quasi-static deformation. The inertial forces are in a first order negligible due to the low acceleration level during the quasi-static measurement (cf. section 2.4.2.6). Only the robot end-effector loads contribute to the quasi-static deformation. The robot end-effector loads result from the low frequency, sinusoidal excitation forces. A six component force sensor measures continuously the robot end-effector loads $\mathcal{F}_{ee}$ (equation 2.7). If no six component force sensor is available, the excitation force is measured continuously by means of a piezo-electric load cell, and besides, this force is transformed to the corresponding robot end-effector loads $\mathcal{F}_{ee}$. The forces acting on the compliant component are derived by transforming the robot end-effector loads $\mathcal{F}_{ee}$ from the end-effector frame $\{XYZ_{ee}\}$ to the corresponding component frame $\{XYZ_{cc}\}$.

$$\mathcal{F}_{cc} = \begin{bmatrix} {}^{cc}\mathbf{R}_{ee} & \mathbf{O}_3 \\ {}^{cc}\mathbf{L}_{ee} & {}^{cc}\mathbf{R}_{ee} \end{bmatrix} \mathcal{F}_{ee}, \tag{2.19}$$

where $\mathbf{O}_3$ is the 3×3 zero matrix, and

$$^{cc}\mathbf{L}_{ee} = \left[\begin{array}{ccc} ^{cc}\mathbf{p}_{ee} \wedge {}^{cc}\mathbf{x}_{ee} & ^{cc}\mathbf{p}_{ee} \wedge {}^{cc}\mathbf{y}_{ee} & ^{cc}\mathbf{p}_{ee} \wedge {}^{cc}\mathbf{z}_{ee} \end{array} \right]. \tag{2.20}$$

The deformation of the compliant component is derived from the absolute movement of the two reference planes characterizing the compliant component. Let W_1 denote the plane just before the compliance, and W_2 the plane after the compliance. The deformation of the compliant component $\mathcal{D}$ results from

$$\mathcal{D} = \mathcal{D}_{w_2} - \left[\begin{array}{cc} ^{w_2}\mathbf{R}_{w_1} & ^{w_2}\mathbf{L}_{w_1} \\ \mathbf{O}_3 & ^{w_2}\mathbf{R}_{w_1} \end{array} \right] \mathcal{D}_{w_1}, \tag{2.21}$$

where $\mathcal{D}_{w_1}$ and $\mathcal{D}_{w_2}$ are found solving equation 2.16, $\mathbf{O}_3$ is the 3×3 zero matrix, and $^{w_2}\mathbf{L}_{w_1}$ is defined by equation 2.20. To realize the subtraction, both reference plane movements are expressed with respect to the same frame, in this case frame $\{XYZ_{w_2}\}$. By combining the reference plane movements, of the planes characterizing the compliant components, in a different manner, the same reference planes can be used for the deformation calculation of the links, of the base and of the joints.

Now, the compliances of the different compliant components can be determined. The compliant *link* ij is characterized by the reference planes ij_1 and ij_2 (figure 2.4). The link deformation $\mathcal{D}_{ij}$ results from equation 2.21:

$$\mathcal{D}_{ij} = \mathcal{D}_{ij_2} - \left[\begin{array}{cc} ^{ij_2}\mathbf{R}_{ij_1} & ^{ij_2}\mathbf{L}_{ij_1} \\ \mathbf{O}_3 & ^{ij_2}\mathbf{R}_{ij_1} \end{array} \right] \mathcal{D}_{ij_1}. \tag{2.22}$$

The forces $\mathcal{F}_{ij}$ acting on the compliant link ij result from equation 2.19:

$$\mathcal{F}_{ij} = \left[\begin{array}{cc} ^{ij_2}\mathbf{R}_{ee} & \mathbf{O}_3 \\ ^{ij_2}\mathbf{L}_{ee} & ^{ij_2}\mathbf{R}_{ee} \end{array} \right] \mathcal{F}_{ee}. \tag{2.23}$$

Equation 2.8 gives a set of 6 equations with 8 parameters $(c1_{ij}, \ldots, c8_{ij})$. This set of equations is underdetermined. Measuring the forces and the deformations in two independent robot configurations a and b, gives a set of 12 equations with 8 parameters.

$$\mathbf{C}_{ij} \left[\begin{array}{cc} \mathcal{F}_{ij_a} & \mathcal{F}_{ij_b} \end{array} \right] = \left[\begin{array}{cc} \mathcal{D}_{ij_a} & \mathcal{D}_{ij_b} \end{array} \right]. \tag{2.24}$$

The compliance matrix $\mathbf{C}_{ij}$ $(c1_{ij}, \ldots, c8_{ij})$ is determined from this equation. This overdetermined set of equations has no exact solution due to measurement errors and modelling imperfections. The linear least squares principle is often applied in this situation. A numerical reliable method to solve this least squares problem is SVD or QR decomposition [36].

The compliant *joint* j is characterized by the reference planes ij_2 and jk_1 (figure 2.4). The joint deformation $\mathcal{D}_j$ results from equation 2.21:

$$\mathcal{D}_j = \mathcal{D}_{jk_1} - \begin{bmatrix} {}^{jk_1}\mathbf{R}_{ij_2} & {}^{jk_1}\mathbf{L}_{ij_2} \\ \mathbf{O}_3 & {}^{jk_1}\mathbf{R}_{ij_2} \end{bmatrix} \mathcal{D}_{ij_2}. \tag{2.25}$$

The forces $\mathcal{F}_j$ acting on the compliant joint j result from equation 2.19:

$$\mathcal{F}_j = \begin{bmatrix} {}^{jk_1}\mathbf{R}_{ee} & \mathbf{O}_3 \\ {}^{jk_1}\mathbf{L}_{ee} & {}^{jk_1}\mathbf{R}_{ee} \end{bmatrix} \mathcal{F}_{ee}. \tag{2.26}$$

The joint compliance constant c_j is determined from equation 2.10 or 2.11.

The *base* compliance matrix $\mathbf{C}_b$ is determined from equation 2.27:

$$\mathcal{D}_b = \mathbf{C}_b \mathcal{F}_b, \tag{2.27}$$

where $\mathcal{D}_b$ is the deformation of the plane B, coinciding with the mounting plate of the robot. The forces $\mathcal{F}_b$ acting on the base B result from equation 2.19:

$$\mathcal{F}_b = \begin{bmatrix} {}^{b}\mathbf{R}_{ee} & \mathbf{O}_3 \\ {}^{b}\mathbf{L}_{ee} & {}^{b}\mathbf{R}_{ee} \end{bmatrix} \mathcal{F}_{ee} \tag{2.28}$$

2.2.3 Error consideration

Based on the experiences with the experiments performed in section 2.4, an error consideration on the quasi-static compliance breakdown method seems to be useful. Such an error consideration can be divided into two domains. A first domain of possible errors is attached to the quasi-static measurement; errors due the measurement method and the measuring equipment, just as due to the processing of the measured data in the analyzer. On the other hand, also the compliance

breakdown itself can introduce some important errors; errors related to the quantification of the compliance parameters of the different compliant components. For both domains, some general precautions to prevent errors are discussed in the following two sections. A third section gives some practical considerations concerning some specific error sources of some commercially available motion measuring equipment.

2.2.3.1 Errors with respect to quasi-static measurement

It should be stressed that the final result of the quasi-static compliance breakdown can only be as good as the measurements, on which the compliance breakdown is based. Therefore, the quasi-static measurement should be carried out very carefully. As already mentioned above, errors can creep in the quasi-static measurement due to the measurement method, due to the measuring equipment, and due to the processing of the measured data in the analyzer.

The goal of the quasi-static measurement method is to measure the displacements of the reference planes, characterizing the different compliant components of the robot, within the flux of force. To realize this, a temporary change of the robot structure is necessary; accelerometers need to be fixed to the robot at different, predefined structural points; a force (and moment) transducer is fixed to the end-effector of the robot; a shaker is connected to the force transducer. The fixing of this equipment to the robot could influence the structural behaviour of the robot itself, and of its components.

Beside the equipment fixed to the robot, also fluctuations of temperature can introduce some errors to the quasi-static measurement. A quasi-static measurement of the whole robot takes several hours. Within this period, the temperature of the environment and especially the temperature distribution along the robot should be kept as constant as possible while fluctuations of temperature introduces changes in the structural behaviour of the robot and of its components.

With respect to the measuring equipment itself, several error sources can be considered.

- Highly accurate and linear measuring equipment should be used.
- The calibration of the sensitivity of this equipment should be carried out very carefully. For a load cell or for an ordinary

accelerometer this is not very difficult, although for the measurement with these transducers their cross-influence could be important. If a six component force sensor is calibrated, the calibration should take into account the cross-influences between the six measurements. If a servo accelerometer [35] is used, the calibration of its sensitivity becomes much more difficult, and besides, also the exact point where the acceleration is measured inside the servo accelerometer need to be calibrated (cf. section 2.2.3.3). Mostly, the calibration of the measurement equipment is carried out statically or at relatively high frequencies. However, as the first natural frequency of some industrial robots is about $10Hz$, the measuring equipment should also be sensitive at very low frequencies. So, for the quasi-static measurement, also the sensitivity frequency response of the used equipment is very important.

- If a loadcell is used to measure the excitation force, the mounting of the load cell becomes very important. The excitation force should only induce a force in the direction measured by the load cell. Therefore the beam transmitting the force from the shaker to the load cell should only be stiff in the excitation direction. All forces and moments, not measured by the load cell, but applied at the end-effector of the robot cause additional deflections which are measured by the accelerometers. Those deflections disturb the compliance modelling.

- If electromagnetic shakers are used, the functioning of the measuring equipment can be disturbed. Electromagnetic shakers produce a large, permanent magnetic field around the shaker. Therefore, as some of the measuring equipment, such as a lot of accelerometers, operates on magnetic principles, they need to be perfectly shielded magnetically.

When the previous measures have been taken into account, the measuring equipment can be fixed to the robot, and the quasi-static measurement can start. The measured accelerations and forces are led to a multi-channel data acquisition system which converts simultaneously the analog signals to their digital value and stores them in memory. Some problems related to the digitizing of analog signals are discussed in section 3.4.4.1.1. Later on these digital signals are then

led to a microcomputer which determines the magnitude and the phase dependent behaviour of the measured displacements and forces at the considered frequency. Within the measured signals, beside the fundamental component, at the quasi-static frequency f_{qs}, also harmonic components and noise are observed.

2.2.3.2 Errors with respect to compliance breakdown

Errors with respect to the compliance breakdown itself are related to the calculations necessary to quantify the compliance parameters of the different compliant components. Those calculations are divided into different steps:

1. the determination of the absolute movement of the reference planes which characterizes the compliant components (section 2.2.2.2);
2. the determination of the forces acting on the compliant components, and of the deformations of the compliant components (section 2.2.2.3);
3. the quantification of the compliance parameters of the compliant components (section 2.2.2.3).

The determination of the absolute movement of a reference plane is based on the structural displacement vectors measured at different points of the plane, and on the position and orientation of the measurement frame within these points with respect to the plane frame. To determine the displacements of the reference plane, this position and orientation information does not need to be so accurate. But to determine the rotations of the reference plane, the exact information is necessary. Especially the orientation of the measurement frame is not always easy to be defined. Using in one measuring point a triaxial *angular* accelerometer instead of a triaxial translational accelerometer overcomes this problem. This triaxial angular accelerometer measures directly the rotations of the reference plane. However, this type of accelerometers has become available only recently, and great care should be taken to their cross-sensitivity to translations, and even to their sensitivity to angular motion (cf. section 2.2.3.3).

The determination of the forces acting on a compliant component is based on the forces measured at the end-effector of the robot and on

the geometry of the robot between the end-effector and the compliant component, while the determination of the deformation of the compliant component is based on the absolute movement of the two reference planes, characterizing the compliant component, and on the geometry of the component between the two reference planes. In both cases, it is advisable to know the geometry of the robot as good as possible. However, as these parameters are known very accurate (error less than 1%) their influence is limited: e.g. an error of $1mm$ on a distance of $1m$ to the end-effector causes on error of 0.1% when calculating the moment due to a force applied at the end-effector.

Finally, the quantification of the compliance parameters of the component is realised by solving the set of equations relating the deformation of the compliant component to the forces acting on this component. Within this step of the calculations several problems can occur:

- the compliance modelling of the compliant component should approximate as close as possible the real structural behaviour of the component. For components with a non-linear structural behaviour the constant compliance parameters could be replaced by a table of compliance parameters: e.g. if the joint compliance is function of the joint angle a table of joint compliances, measured with respect to the considered joint angle, could be drawn;

- this overdetermined set of equations has no exact solution due to measurement errors and modelling imperfections. The linear least squares principle is often applied in this situation. A numerical reliable method to solve this least squares problem is SVD or QR decomposition [36];

- to determine the joint compliance, beside the compliance due to the mechanical transmission between the actuator and the joint, also some compliance due to the robot controller can be considered. This influence is measured by carrying out also a quasi-static measurement with the robot controller on, and the actuator brakes off. However, for some robots this is difficult to realize without moving the robot. If only the *static* load-deformation is considered, the compliance contribution due to

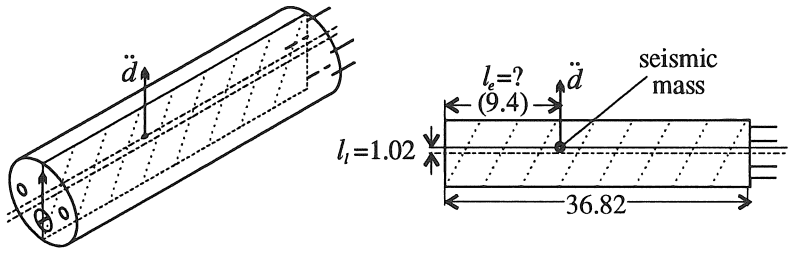

Figure 2.6: Schematic representation of a SUNDSTRAND servo accelerometer.

the robot controller can be neglected with respect to the compliance due to the transmission.

2.2.3.3 Two practical examples of an error consideration

This section discusses two practical examples of problems, and errors, encountered with the use of some commercially available motion measuring equipment. First, a problem occurring when using a servo accelerometer for measuring rotational accelerations is discussed. Secondly, the influence of the linear acceleration sensitivity, of an angular motion velocity sensor, on rotational velocity measurements is discussed.

2.2.3.3.1 Influence of the exact knowledge of the position of the seismic mass of a SUNDSTRAND servo accelerometer on rotational acceleration measurements

Figure 2.6 gives a schematic representation of a SUNDSTRAND servo accelerometer [35]. The values mentioned in the figure are expressed in *mm*. The figure at the right shows the position of the seismic mass, used to measure the acceleration, within the vertical longitudinal plane of the accelerometer. The servo accelerometer measures the acceleration in a direction perpendicular to the longitudinal axis, contrary to traditional accelerometers which measure the acceleration in a direction along the longitudinal axis.

When measuring the rotational acceleration, $\ddot{a}$, of a system with a servo accelerometer (cf. figure 2.7), by putting the servo accelerom-

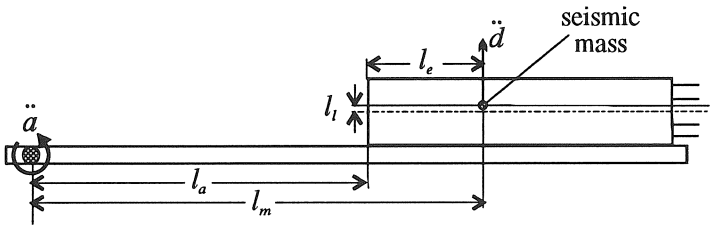

Figure 2.7: Schematic representation of a rotational acceleration measurement using a servo accelerometer.

eter at a certain distance, l_a, from the rotation point of the system, it is obvious that the exact knowledge of the distance between the rotation point and the seismic mass of the accelerometer, l_m, is very important. However, the manufacturer of the servo accelerometer only specifies the distance between the seismic mass and the longitudinal axis, l_l, and does not specify the distance between the seismic mass and the end-plates of the accelerometer, l_e. As in our application the distance l_a is only a few centimetres an error of some millimetres on l_e is very important. Therefore calibration of this distance was necessary (l_e=9.4mm).

2.2.3.3.2 Influence of the linear acceleration sensitivity of an angular motion velocity sensor on rotational velocity measurements

Recently, *angular* motion sensors (KISTLER [63] and PCB [64]) have become commercially available. However, great care should be taken to their cross-sensitivity to translations, and to their sensitivity to angular motion. Finding, for commercially available angular motion measuring systems, a value for this cross-sensitivity poses a real problem. From the two systems cited above, only the manufacturer of the secondly mentioned system [64] specifies a value for the linear acceleration sensitivity. Based on this information and based on the results of the quasi-static measurement carried out in section 2.4.2 a practical error evaluation is discussed.

Figure 2.15, of section 2.4.2, shows the dimensions of the beam on which the quasi-static measurement has been carried out. The beam

has been excited at point E_1 by a vertical, sinusoidal force with an amplitude of $10N$ and a frequency, f_{qs}, of $4\,Hz$. The accelerations has been measured at the point P_1 of the beam. The results of the quasi-static measurement are:

$$[(\ddot{\mathbf{d}}_{p_1})_w]_z = 0.037\frac{m}{s^2}, \tag{2.29}$$

$$(\ddot{\mathbf{a}}_w)_y = 0.286\frac{rad}{s^2}; \tag{2.30}$$

with

$$l_x = 0.131mm,$$

where l_x is the distance between point P_1 and the longitudinal axis of the beam.

The measuring system specified in [64] is an angular motion velocity sensor. The manufacturer specifies a linear acceleration sensitivity, s_l, of $0.005\frac{rad}{s}/g$. Using this sensor to measure, within the above described experiment, the rotational velocity, $(\dot{\mathbf{a}}_w)_y$, yields following results:

$$\begin{aligned}(\dot{\mathbf{a}}_w)_y &= \frac{(\ddot{\mathbf{a}}_w)_y}{2\pi f_{qs}}, \\ &= \frac{0.286}{8\pi}\frac{rad}{s}, \\ &= 11.38\,10^{-3}\frac{rad}{s}.\end{aligned} \tag{2.31}$$

To calculate the influence of the linear acceleration on the rotational velocity measurement, the units used in equation 2.29 have to be adapted:

$$[(\ddot{\mathbf{d}}_{p_1})_w]_z = 3.77\,10^{-3}g,$$

with $g = 9.81\frac{m}{s^2}$. For the considered sensor, the influence of the cross-sensitivity to linear acceleration is:

$$\begin{aligned}\Delta_{\dot{a}} &= s_l[(\ddot{\mathbf{d}}_{p_1})_w]_z, \\ &= 18.85\,10^{-6}\frac{rad}{s}.\end{aligned}$$

The error on the rotational velocity, specified in equation 2.31, is about 0.2%, which is of course very small. In this case, the influence of the linear acceleration on the rotational velocity measurement is negligible.

Although for this sensor the cross-sensitivity to linear acceleration does not pose any problems, this sensor is not suited for the quasi-static measurement. The biggest problem poses its sensitivity to the rotational velocity. The sensitivity of this sensor is $6.7mV/\frac{rad}{s}$, which gives for this experiment, cf. equation 2.31, a voltage of $0.076mV$. This is of course far too low. The KISTLER measuring system poses the same problem.

So, the at the moment commercially available angular motion sensors are not usable for this type of application: especially due to their low sensitivity to angular motion.

2.3 Improving robot precision

The results of the previously described compliance breakdown contribute to potential improvement of robot precision in several ways. In *robot design*, the results of this study should be useful for making some critical design improvements [7, 37]. In addition, the prediction and *compensation of robot end-point deflection* may be incorporated into the robot software to improve the working precision of robots. This is particularly valuable to off-line robot programming in which precision of robots is critical for successful implementation. In *workspace analysis*, these results enable to choose, for a given task, the best robot posture and the best workpiece position with respect to the robot arm. In subsequent sections, an overview of literature is presented for the above mentioned applications. As the literature on these applications is quite extensive, only the most relevant papers will be reviewed herein.

2.3.1 Design improvements

In robot design, some critical decisions must be made concerning the following questions:

1. Where should the motors for driving the forearm and the wrist be mounted?

2. Should harmonic drives or gear trains be used for amplification of torques?

3. Which of the joints, links, and bearings should be stiffened first in order to improve accuracy?

4. Should the joint rotation be measured before or after the speed reduction?

The quasi-static measurement provides a method for determining the static weak points of robots. On the basis of this compliance breakdown, well-aimed design improvements can be simulated, implemented and verified. In literature, two approaches are found to perform those design improvements:

1. Replace the weak components by less weak components (1) which are commercially available, (2) which fulfil the stiffness and dimensional requirements of the considered components, and (3) whose characteristics are filed in a database (including dimensions, stiffness information, ...). Performing a database search can give the desired, better components. Due to the characterization of the stiffness of the components in the database, the improvement produced by a new component can be simulated. If the new component fulfils the stiffness and dimensional requirements, the weak component can be replaced by the new component. If not, a next database search is performed. If however no component which fulfils all requirements is found, the second approach can be considered.

2. Replace the weak components by less weak components which are better designed according to *design for stiffness* principles. Conventional and new design techniques are used to improve the stiffness of the components.

In subsequent sections, an overview of literature is presented for the above mentioned approaches.

2.3.1.1 Optimal robot construction programming system

To improve the design of robots, WECK [38] uses a programming system which allows to optimize, with regard to several, partly contradictory criteria (e.g. minimal weight, maximal stiffness), the mechanical construction of a robot. The programming system consults a database

with the characteristics of all possible robot components. Those characteristics are (1) derived from information provided by the manufacturer, or (2) measured by specially developed test facilities, or (3) calculated by appropriate calculation methods. This programming system is used to investigate and to optimize different types of robots, such as gantry robots [39, 40] and articulated robots [41].

The optimization of the mechanical construction of a robot consists of following steps:

1. collection of the characteristics of all possible robot components;
2. creation of a database, and filing of the previously determined characteristics in this database;
3. realization and adaptation of the optimization strategies, and of the structural calculation methods;
4. compliance breakdown of the robot;
5. optimization of the mechanical construction of the robot using the programming system developed in steps 2 and 3, and using the information resulting from the compliance breakdown.

For the robot components, only those characteristics relevant for the optimization of the robot are considered. This involves on the one hand geometrical and technical data, such as dimensions, built-in volume, weight, moment of inertia, rated torque, static and dynamic load ratings, and on the other hand structural data, such as stiffness and damping. Figure 2.8 [38] shows the structure of the database containing the previous mentioned characteristics of the (commercially) available robot components.

Criteria considered for the optimization of the structural and dynamical behaviour of the mechanical construction of a robot are, besides *stiffness* and *weight*, also the *undamped natural frequencies.*

2.3.1.2 Design for stiffness

RIVIN investigates in his book *Mechanical design of robots* [7, Chapter 4] very thoroughly the structural dynamic characteristics of robots, including stiffness, inertia, damping, and natural frequencies. Special attention is paid to stiffness enhancement. Besides a design technique

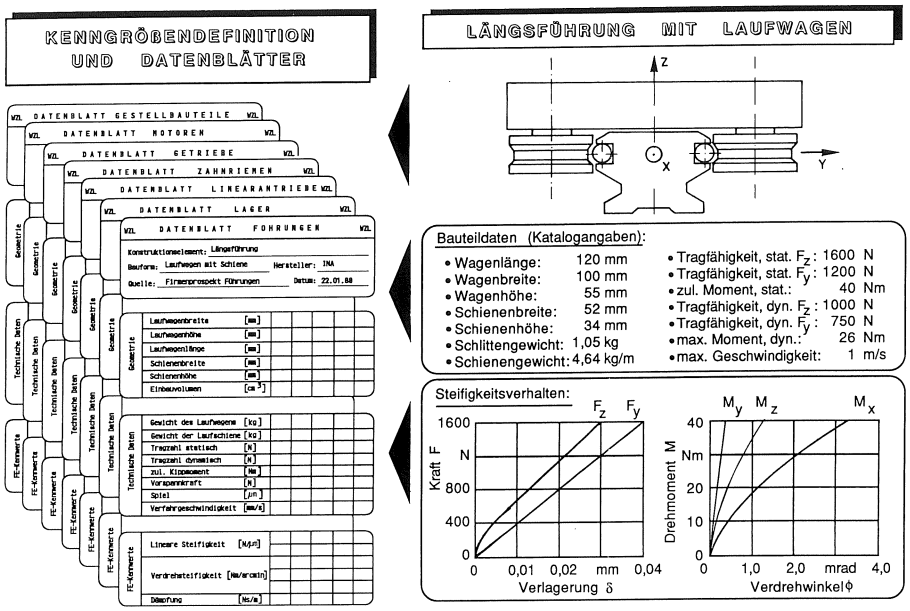

Figure 2.8: Structure of the robot component database.

for stiffness enhancement developed by RIVIN, also some design techniques developed by other people are mentioned.

RIVIN considers the compliance, a reciprocal of stiffness, of a robot a result of three basic factors:

1. structural deformations of load-transmitting components;
2. contact deformations between parts;
3. deformations in the energy-transforming devices (motors and actuators).

He states that

> "stiffness is one of the most important general criteria of machine design; which is especially true for robots. The problem of stiffness enhancement is especially important since conventional techniques, such as "beefing up" cross sections or using higher-modulus conventional materials, are in many cases not acceptable either because they are counterproductive (increasing weight brings higher inertial

> forces, and thus, larger deflections) and/or not cost effective. However, there are still substantial resources for enhancement of the stiffness of robots. To utilize these resources and, as a result, to improve the performance and accuracy characteristics of robots, one has to clearly understand the sources of structural compliance, compute a compliance breakdown, identify weak points, and direct design efforts toward their improvement. Any efforts wrongly targeted to improve areas which are not the major contributors to the overall compliance would result in waste."

In his book, RIVIN further considers several conventional techniques for the optimization of certain stiffness characteristics. A technique deserving particular attention is the *combination link* design technique [7, 42]. This technique is described more in detail in the next paragraphs.

Deflections are proportional both to compliance and to forces. Therefore deflections can be reduced by the reduction of the acting forces: inertia forces, gravity forces and robot end-effector loads. For given motion regimes the only way to reduce motion-related forces is by reducing the inertia of the structural components, including the inertia of the links. The most important constraint during this process is a requirement that inertia reduction is not to be accompanied by a significant reduction in stiffness.

From the deflection analysis of a revolute link, following observations are made: (1) the highest intensity of inertial forces is generated in sections adjacent to the end of the link; (2) the greatest bending moment occurs at the built-in end of the link. Rephrased for design purposes, this sounds: "A well designed link would be characterized by a *light end-of-link* segment and a *rigid center-of-rotation* segment with not very stringent requirements as to rigidity of the former and/or to the specific weight of the latter." These specifications call for a *combination link* design, which is relatively easy to implement by a reliable joining of several segments of the same cross-sectional shape that are made of different materials.

The main advantages of the combination link structure are a reduction of arm end deflections, and a reduction in the required driving torque. However, there are additional advantages important for robot applications, such as:

- a shift of center of gravity of the link closer to the center of rotation;
- reduction in the overall mass and moment of inertia of the link;
- an increase in the fundamental natural frequency of bending vibrations of the link which, in many cases, is equivalent to the natural frequency of the whole robot structure in certain motion modes;
- reduction of the static stiffness of the link is not very significant as compared with a link made of one material with greater elasticity modulus.

Another design technique for stiffness enhancement, proposed by WEST and ASADA [43], and by BOOK ET AL. [29], is *bracing*. This technique is used effectively in human motion when the arm is held rigid by resting the heel of the hand against a stationary object, as during writing. Manipulation is then carried out with the hand's precision degrees of freedom. Just as a human being, a robot can brace itself against the work surface and perform its task with greater force and accuracy. One possibility of bracing the robot against its work surface is by using a "jig hand" as shown in figure 2.9. It incorporates a special hand with kinematic constraints in selected directions for rigidization but allows the existing joints of the arm to move the end-effector in other directions. The main advantages of a "jig hand" are

- an improvement of the load bearing ability of the robot by bracing the manipulator against the work surface and increasing its mechanical advantage, so enabling it to bear larger loads at the end-effector, and by increasing the effective stiffness of the robot;
- the possibility for the robot to reference the motion of its tool relative to a reference surface on the workpiece, hence eliminating some of the tool positioning errors due to misalignment of the workpiece.

A final, within this section discussed, design technique for stiffness enhancement is the *framework integration* design technique [44], applied at the Laboratory for Engineering Design (LKL), University of

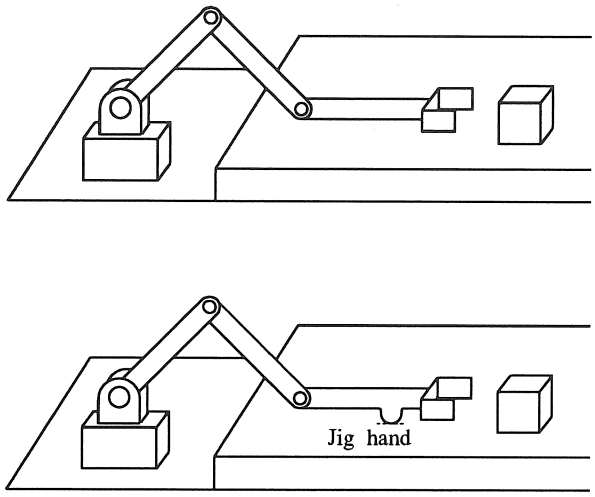

Figure 2.9: Manipulator constrained by contact with the environment.

Paderborn, Germany. This technique tries to reduce the weight of a robot arm to achieve high working speed and high positional accuracy by

1. a well-considered arrangement of drive motors and transmissions;
2. an optimization of the robot components using "framework integration".

The optimization of the components is subdivided into the following criteria: form, material, stability, power stream, and production. The result of this optimization for the robot arm of figure 2.10 is a mixed form of construction out of framework and plate connections to combine the advantage of both construction types. The area between the two joints not containing any further components and the smoothly-running power stream within this area allows this area to be substituted by a framework. However, the integration of gearing, motors, ... in a framework causes difficulties. Therefore plates are needed. Hyperbolic transitions from the plates to the framework provide an improvement of the power stream. With the shape of the robot arm as the first point of optimization, the thickness of the plates could be

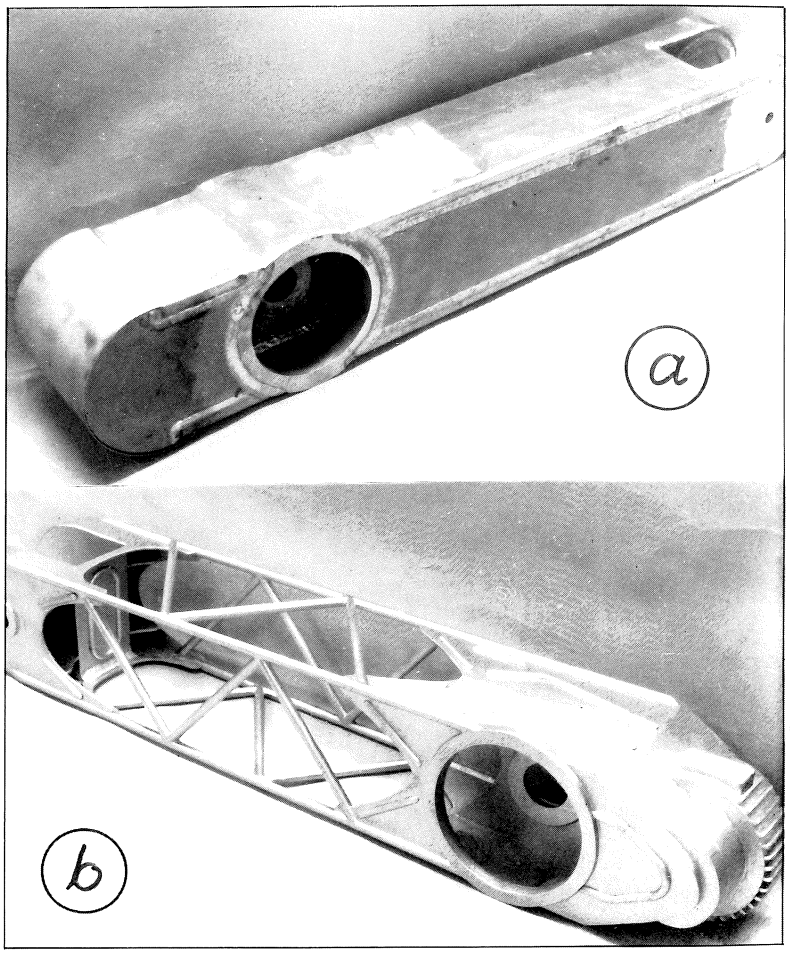

Figure 2.10: Different types of supporting structure of a robot arm: (a) joint arm made of *Al* semi-finished products (plate); (b) joint arm with integrated framework made of *Al* semi-finished products (plate and tube).

reduced as a result of the low material utilization. To avoid the inevitable deformation of the robot arm, numerous crimps are put into position. As a result of this component optimization, the weight of the robot arm supporting structure could be reduced by 58%, though the material was not changed.

2.3.2 Deformation compensation

A first section discusses the *off-line deformation compensation* of a general serial manipulator, and of hybrid systems which combine serial links with parallel structured modular devices. Only "quasi-static" deformations are considered. Thus small oscillations (due to vibrations) are ignored and the inertial loads are considered applied loads. Although the technique discussed within this section is too time consuming for on-line implementation, an effort is mentioned that tries to realize on-line compensation based on the developed compliance model.

A second section deals with the *real-time deformation control of flexible systems*, which includes static deformation compensation as well as vibration control. In fact, the method discussed within this section does not use the results of the previously described compliance breakdown method. However, it focuses on a technique which uses the optical link deflection sensor which has also been developed within this thesis (cf. section 3.6.1) to realize fast and accurate tracking control of a flexible one-link robot.

As the literature on these applications is quite extensive, only the most relevant papers will be reviewed hereafter.

2.3.2.1 Off-line deformation compensation

Compensation of the robot structural deformations can be realized on the basis of the compliance model developed in section 2.2. Only "quasi-static" deformations are considered (see above). The local link and joint deformations are found combining the corresponding compliances with the forces acting on the compliant component. The derivation of these forces requires sensing the local reaction forces and moments from the end-effector and also the joint dynamic states (velocity and acceleration). Joint position and dynamic state information is then used as inputs to a dynamic and gravitational loading model.

This model combined with the end-effector load information yields the forces acting on the compliant component. For this purpose, an on-line computational scheme for mechanical manipulators has been developed by LUH ET AL. [5]. The local deformations are transformed to end-effector deformations through the use of the robot geometry. FRESONKE ET AL. [45, 46] describe a method to derive systematically the total end-effector error for a general serial manipulator. This method considers end-effector, gravity, and inertial loads. SKLAR and TESAR [47] generalize the method by FRESONKE to hybrid systems which combine serial links with parallel structured modular devices. The magnitude of the joint displacements $\Delta\theta_t$ required to compensate for the total end-effector error $\mathcal{D}_{ee_t}$ is estimated as

$$\Delta\theta_t = -\mathbf{J}^{-1}\,\mathcal{D}_{ee_t} \tag{2.32}$$

where J is the Jacobian and is assumed to be non-singular.

BAGCI [48] uses a quasi-static model, considering flexibility effects in a technique very similar to the derivation provided by FRESONKE. Included in his work is an iterative compensation algorithm providing joint angle corrections to compensate for end-effector deformation.

Compensating in this manner, that is using the system's joint actuators, always limits the response time to the inherent capability of the robot itself. Thus, a few researchers have considered high-speed, external devices to provide compensation at a much higher bandwidth.

TLUSTY AND STERN [13] use a single DOF additional slide, mounted at the end-effector, for corrective motion (figure 2.11). In this system, a dynamometer D measures the cutting forces at the plate carrying the additional slide and servomechanism. The servomotor M drives the table T through a cam C and follower transmission. The spindle with the routing tool R is attached to the table. The commands for the corrective motion of this additional servo are determined from the inputs of the force components and the tool position co-ordinates via the flexibility model developed by STERN [14]. HUDGENS [49] extended this concept further leading to a complete 6-DOF "micro-manipulator" device capable of providing complete compensation for end-effector deformation. Compensation achieved through external devices offers significant advantages over compensation by robot joint correction mainly due to quicker response, better resolution, and partially decoupled linear motion.

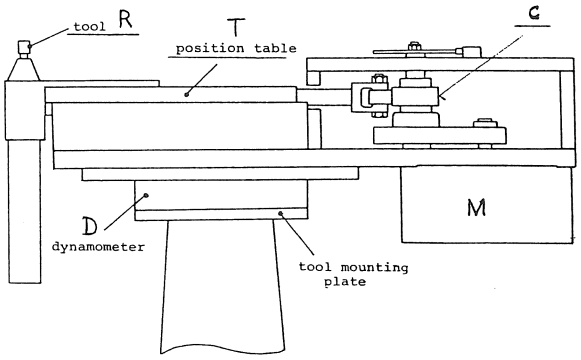

Figure 2.11: Additional slide for corrective motion.

The technique presented in this section is too time consuming for on-line implementation and is best used to predict *off-line* deformations due to known loads. However, WANDER and TESAR [50] try to realize *on-line* compensation by realizing the method developed by FRESONKE in the form of pipelined modelling software which is implemented on a medium-sized array processor to run in real time.

2.3.2.2 Real-time deformation control of flexible systems

BOOK ET AL. [29] formulate the problem of control of flexible systems as follows:

> "The problem of flexible arm control can be solved in several ways, but each choice presents its own constraints. These options include:
>
> - materials and shapes with higher stiffness-to-weight ratios and higher damping ratios;
> - feedback control algorithms that account for the flexible dynamics;
> - strategies of arm use that avoid the problem whenever possible (e.g., a lightweight, flexible arm for gross motion and a rigid one with lesser high-inertia penalties for fine motions; bracing);
> - arm trajectories which do not unnecessarily excite flexible behaviour.

> The highest performance requires a combination of these choices."

The approach of BOOK ET AL. has concentrated on the first two choices, although they briefly discuss the others also.

In literature, the control of flexible systems has been quite extensively discussed. The work by CANNON and SCHMITZ [21] deserves special attention because they belong to the first people who developed and *demonstrated* techniques for stable and precise position control of one end of a very flexible beam by use of direct measurement, described in section 1.3.3, of that end's position as a basis for torqueing at the other end.

A second technique worthwhile mentioning is the "linear control of flexible robots"-technique developed by SWEVERS [28], at the Division of Production Engineering, Machine Design and Automation (PMA), Katholieke Universiteit Leuven, Belgium. This technique has been experimentally validated for the continuous path tracking control of a flexible one-link robot, and of a KUKA IR 161/60 industrial robot with joint flexibility. In the next paragraphs, this control technique is briefly discussed and is used to realize fast and accurate tracking control of a flexible one-link robot, based on real-time link deflection measurements performed by the optical link deflection sensor developed in section 3.6.1 [51]. This paragraph is based on the paper by SWEVERS ET AL. [52].

The control technique developed by SWEVERS aims at good tracking and positioning accuracy, which are both very important in industrial robot applications. The control design is based on a discrete time state space model that is built from two experimentally identified transfer functions of the system. The identification method used for this purpose is a frequency domain identification method which fits discrete time transfer functions to stepped-sine measured frequency response functions. The frequency domain identification method is the weighted least squares frequency domain identification method [28]. The controller is a discrete time controller that consists of: (1) feedforward, and (2) feedback of the difference between desired and measured states. It uses the non-minimal phase zero elimination scheme of Tomizuka [53, 54] for the feedforward calculation. This feedforward calculation aims at zero tracking errors; it is based on the inverse

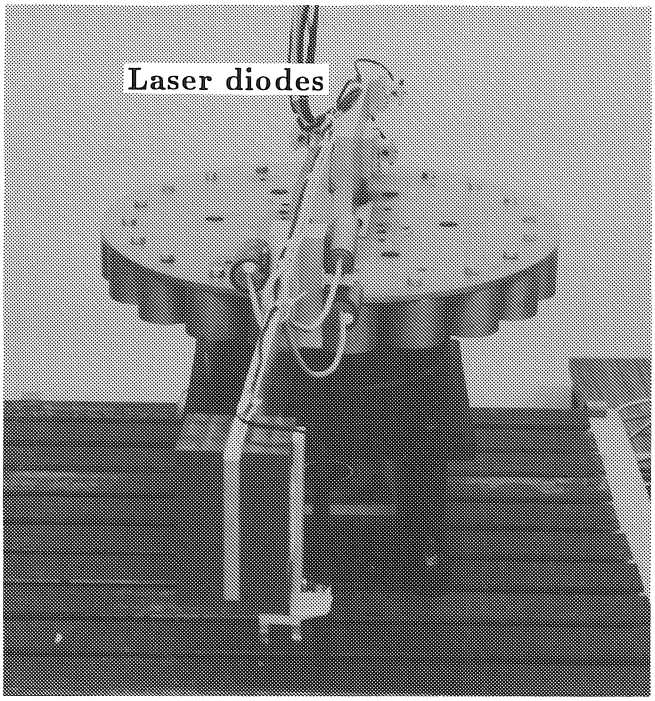

Figure 2.12: Test setup.

open loop model of the system, and therefore independent of the feedback calculation. The feedback term compensates for disturbances and modelling inaccuracies. Much attention is paid to simplicity as implementation on an industrial robot controller need to be considered.

The experiments on a flexible one-link manipulator prove that the control approach allows accurate tracking and positioning. The tests also show that the tracking accuracy and overshoot are very sensitive to modelling errors, while the disturbance rejection ability, which is function of the feedback, is less sensitive to these errors.

Figure 2.12 shows the test setup. It consists of a flexible beam with a payload, equipped with an optical link deflection sensor, developed in section 3.6.1. The beam is connected to a direct drive brushless dc-motor. The first resonance frequency is a free-free mode in the neighbourhood of $8.4Hz$. The second resonance frequency is at approximately $52Hz$. This mode and the higher ones are not taken into

account in the modelling and control. An anti-resonance exists at approximately $5Hz$, which corresponds to a slightly damped clamped-free mode. The control input to the system is a voltage between -10 Volt and +10 Volt, which is linearly converted by the power supply of the motor into a current. A built-in encoder measures the angular motor position. The optical link deflection sensor measures the beam deflections. As the beam is very rigid in the vertical plane and as most of the applied loads lie in the horizontal plane, only the deflections in the horizontal plane, d_y and a_x, should be considered. From those deflections, only the structural displacement d_y is needed to determine the end effector position. The optical link deflection sensor is mounted somewhere halfway the link because of the limited measuring range of the PSD ($\pm 5mm$). The beam deflections at the tip, d_y, exceed this range during the tracking control of the flexible beam. When only one natural frequency is taken into account, which is the case here, the beam deflection at the tip, d_y, is proportional to the deflection measured by the PSD. The proportionality factor has been calibrated, and is equal to 4.01. The maximum beam deflection is therefore restricted to $4.01 \times \pm 5mm = \pm 20.05mm$. The end effector position is determined by the motor position and the beam deflection d_y, and is expressed in mm arc length.

A tracking test has been executed to validate the controller performance. The feedforward calculation method used by this control technique requires a smooth path: simulation with the inverse model of the system results in large peaks in the feedforward signal if the desired trajectory is not smooth. In addition it avoids unnecessary excitation of the natural frequencies. Therefore, the reference trajectory is based on a tenth order polynomial which gives intermediate positions between the initial and final position along a smooth path.

The maximum end point acceleration and end point velocity during the tracking are $14.0 \frac{m}{s^2}$ and $6.88 \frac{m}{s}$. These values are selected such that the beam deflection, during the tracking, remains just within the measuring range of the link deflection sensor. The total displacement of the end point is $5158.5\,mm$ arc length, which corresponds to one motor revolution. The final position should be reached after 2.06 seconds.

Figure 2.13 shows the control results. The horizontal dashed lines indicate the steady state error tolerance of $\pm 0.1mm$. The vertical

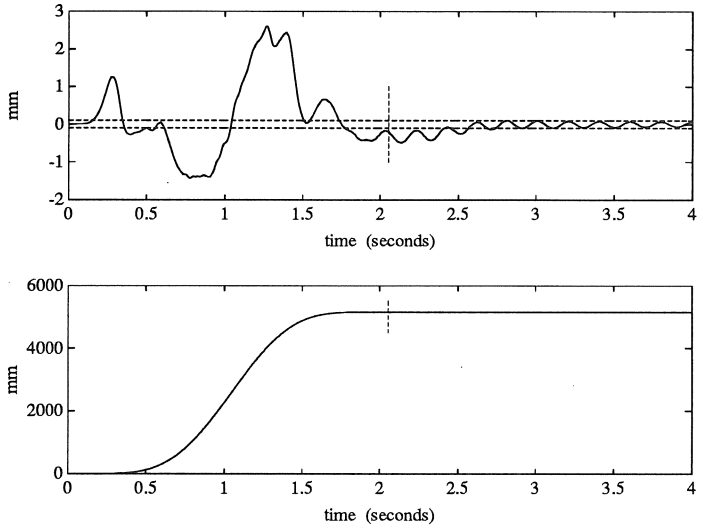

Figure 2.13: Control results. Top figure: tracking error. Bottom figure: desired end effector trajectory.

dashed line indicates the time instant at which the desired final position should be reached ($2.06s$). The maximum tracking error is less than $3mm$. The magnitude of the small oscillation at the frequency of the anti-resonance frequency is less than $0.1mm$. The steady state error is within the tolerance of $\pm 0.1mm$.

An increase of the payload ($3kg$) with a mass of ($0.085kg$) doubles the maximum tracking error and introduces an overshoot of $1.0mm$, but does not increase the small oscillations at the destination point. This proves that the model and feedforward signal are very accurate, but also that the tracking accuracy is very sensitive to modelling errors. The disturbance rejection ability, function of the feedback gains, however is less sensitive to modelling errors.

2.3.3 Workspace analysis

Workspace analysis, based on the developed compliance model of the robot, allows to select best robot posture and workpiece position with respect to the robot arm for a given task.

Based on the compliance model developed in section 2.2, the soft-

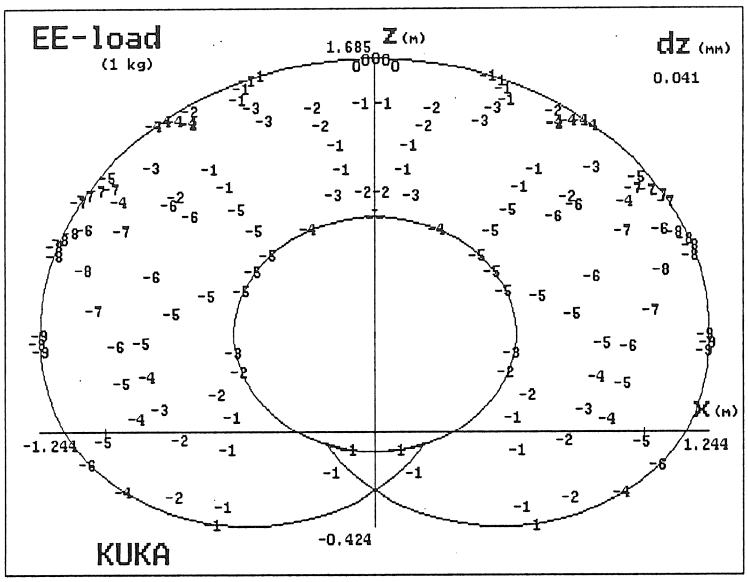

Figure 2.14: Graphical representation of a workspace analysis.

ware described within section 2.4.4 allows to analyze the spatial deformation behaviour of a robot within its workspace. In every point of the robot workspace, the program calculates the spatial deformation (X-, Y- and Z-component, defined within the robot baseframe) of the robot end-effector due to: (1) proper gravity loads, and (2) known end-effector loads. Figure 2.14 gives a graphical representation of a workspace analysis performed on the KUKA IR 361/8.0 industrial robot. This figure takes into consideration only the flexibility of the first three joints (section 2.4.3). The figure shows the Z-component of the spatial deformation of the robot end-effector, dz, for a static end-effector load of $1kg$; no proper gravity loads are considered. The highest deformation, in the Z-direction, encountered in the robot workspace is $0.041mm$. The solids lines represent the limits of the robot workspace. The figures, between "0" and "9", within the workspace correspond to a certain deformation level: "0" corresponds to the lowest deformation encountered in the robot workspace, while "9" corresponds to the highest deformation, $0.041mm$. The "+" and "-" refer to the sign of the value of the deformation.

Workspace analysis also allows to assess the suitability of the robots intrinsic elastic compliance for a given task and to determine the need

for additional external compliance to achieve the desired adaptability. For example, in small parts assembly, errors on the order of $1mm$ are often encountered, so the use of a remote center compliance (RCC) [55] becomes necessary to achieve successfully the assembly task. Information on the robots intrinsic elastic compliance for this task is useful to choose an appropriate RCC.

2.4 Experiments

In this section, the quasi-static compliance breakdown of a beam and of an industrial robot will be discussed. The experiment on the beam is used to verify the accuracy of the quasi-static compliance breakdown method.

2.4.1 Measuring equipment

To perform the experiments, following equipment has been used:

- for exciting the beam with a sinusoidal force, a vibration exciter BRÜEL & KJÆR type 4809 [56]; for the robot, a vibration exciter BRÜEL & KJÆR type 4801 with a big table head type 4813 [57];
- for measuring the excitation force, a piezo-electric load cell KISTLER type 9031 [58] and a charge amplifier KISTLER type 5007 [59];
- for measuring the accelerations at the structural points of the excited structure, a triaxial translational servo accelerometer Mini-Pal - SUNDSTRAND [35] and a 3-channel analog evaluation circuit to convert the accelerometer analog current outputs in voltage;
- for filtering the measured data, a 4-channel GEPA lowpass filter [60];
- for controlling the excitation frequency and excitation force, for acquiring the (filtered) measured data, and for determining the accelerations and forces at the considered frequency, an 8-channel Data-Harvester [61];
- for running the software package, a DATEC AT microcomputer [62].

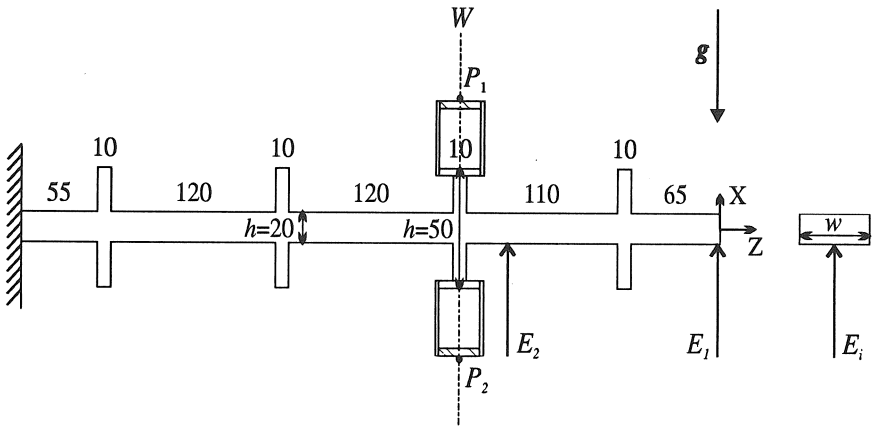

Figure 2.15: Geometry of the clamped-free beam.

2.4.2 Quasi-static compliance breakdown of a beam

A flexible, clamped-free beam is the ideal structure to verify the accuracy of the quasi-static compliance breakdown method. In this case, the quasi-static compliances of the beam can be easily compared to the theoretical and to the statically determined compliances of the beam. By applying vertical loads at the center of the beam, only the compliances in the vertical plane need to be considered.

2.4.2.1 Geometry and material properties of the beam

Figure 2.15 shows the dimensions of the beam in the vertical plane. The width w is uniform for the whole beam, with w=51.7mm. All subsequently determined compliances: theoretical, static and quasi-static, will be defined with respect to the reference plane W of the beam. To measure larger displacements and to allow if necessary measurements at different locations on the beam, the height of the beam is not uniform.

The material properties of the beam are:

material = AlSiMg 1,

Young's modulus of elasticity $E = 66.6GPa$,

shear modulus $G = 25.6GPa$.

2.4.2.2 Theoretical compliances of the beam

For a beam with a length L, a uniform width w and a uniform height h, the theory of elasticity [34] gives following equations for the beam compliances in the vertical plane (Section 2.2.2.1):

$$\begin{aligned} c1 &= \frac{L^3}{3\,E\,I_y}, \\ c5 &= \frac{L}{E\,I_y}, \\ c7 &= \frac{L^2}{2\,E\,I_y}; \end{aligned}$$

with

$$I_y = \frac{w\,h^3}{12}.$$

For the beam used for the quasi-static compliance breakdown (figure 2.15), taking into consideration the different heights, the theoretical beam compliances are:

$$\begin{aligned} c1 &= 4.41\ 10^{-6}\ m/N, \\ c5 &= 129.13\ 10^{-6}\ rad/Nm, \\ c7 &= 20.69\ 10^{-6}\ 1/N. \end{aligned}$$

2.4.2.3 Static compliances of the beam

For a clamped-free beam, the compliances of the beam in the vertical plane are easily determined applying vertical static forces. The vertical displacement of the beam is measured by a dial gauge, while the rotation of the beam in the vertical plane is measured by an autocollimator.

The statically determined beam compliances are:

$$\begin{aligned} c1 &= 4.62\ 10^{-6}\ m/N, \\ c5 &= 130.95\ 10^{-6}\ rad/Nm, \\ c7 &= 20.59\ 10^{-6}\ 1/N. \end{aligned}$$

Comparing the statically determined compliances of the beam to the theoretical ones (table 2.1), following remark can be drawn:

- the static compliances $c1$ and $c5$ of the beam are bigger than the theoretical ones. This difference is caused by the clamp. To determine the theoretical compliances, the clamp is considered

compl.	unit	theoretical	static	$\Delta\frac{t}{s}$
$c1$	N/m	$4.41\ 10^{-6}$	$4.62\ 10^{-6}$	4.4%
$c5$	rad/Nm	$129.13\ 10^{-6}$	$130.95\ 10^{-6}$	1.4%
$c7$	$1/N$	$20.69\ 10^{-6}$	$20.59\ 10^{-6}$	-0.5%

Table 2.1: Static vs. theoretical compliances of the beam.

to be infinitely stiff. However, in practice no clamp is infinitely stiff, and this causes an increase of the compliances. Especially compliance $c1$ is very sensitive to the compliance of the clamp, because for $c1$ the influence of the compliance of the clamp is multiplied by the total length of the beam.

So, to verify the accuracy of the quasi-static compliance breakdown method, the quasi-static compliances of the beam should be compared to the statically determined compliances of the beam.

2.4.2.4 Global stiffness characteristic of the beam

The global stiffness characteristic is linear at the unloaded case. A static preload F_0 is not necessary for the quasi-static measurements.

2.4.2.5 Frequency response of the beam

The beam is excited by a vertical sinusoidal force at point E_1, and the accelerations are measured at point P_1. Figure 2.16 shows the frequency response of the beam. The magnitude in the figures is the ratio between the vertical displacement, derived by integrating twice the measured vertical acceleration, and the measured excitation force.

The beam has its first natural frequency at 38 Hz. The quasi-static range extends up to 8 Hz. To assure the quality of the measurements, the excitation frequency f_{qs} is chosen at 4 Hz. This gives a desired accuracy of 1% (cf. appendix A).

2.4.2.6 Quasi-static compliances of the beam

The aluminium beam is excited by a vertical, sinusoidal force with an amplitude F_a of $10N$ and a frequency f_{qs} of 4 Hz. No static preload F_0

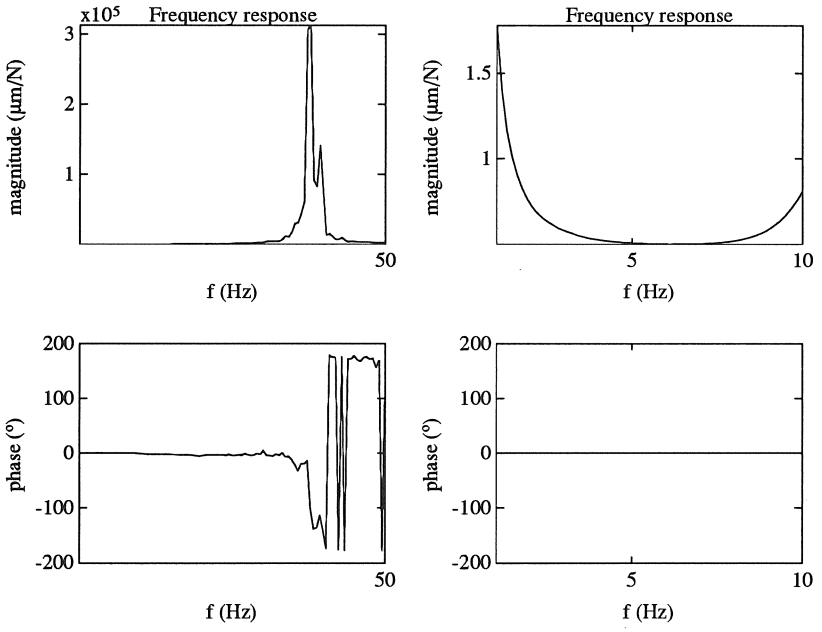

Figure 2.16: Frequency response of the clamped-free beam.

compl.	unit	static	quasi-static	Δ_s^q
$c1$	N/m	$4.62\ 10^{-6}$	$4.76\ 10^{-6}$	-3.0%
$c5$	rad/Nm	$130.95\ 10^{-6}$	$129.51\ 10^{-6}$	1.1%
$c7$	$1/N$	$20.59\ 10^{-6}$	$20.87\ 10^{-6}$	-1.3%

Table 2.2: Quasi-static vs. static compliances of the beam.

is applied. The excitation force is successively applied at two different points E_i at the center of the beam, and is measured by a piezo-electric load cell. The accelerations are measured at the two points P_i of the beam (figure 2.15).

The results of the quasi-static compliance breakdown of the beam are:

$$\begin{aligned} c1 &= 4.76\ 10^{-6}\ m/N, \\ c5 &= 129.51\ 10^{-6}\ rad/Nm, \\ c7 &= 20.87\ 10^{-6}\ 1/N. \end{aligned}$$

The comparison between the quasi-static compliances of the beam and the statically determined ones (table 2.2) shows that the accuracy of the quasi-static compliance breakdown method is very good. Again, part of the inaccuracy is caused by the behaviour of the clamp which in the case of the quasi-static compliance breakdown of complex mechanical structures will be taken into account.

To check the influence of the inertial forces on the quasi-static compliance breakdown, the beam has been excited by a sinusoidal force with an amplitude of $10N$ and a frequency of $7\ Hz$, which is still within the quasi-static region. As the inertial forces are proportional to the realised accelerations, and the accelerations are quadratically proportional to the used excitation frequency, this experiment should indicate if the inertial forces need to be considered for the quasi-static compliance breakdown. The quasi-static compliances resulting from this measurement ($f_{qs} = 7\ Hz$) only differed about 2% from the quasi-static compliances resulting from the previous measurement ($f_{qs} = 4\ Hz$). This can be however totally explained by the results of appendix A. So, this proves that the influence of the inertial forces on the quasi-static compliance breakdown can be neglected.

2.4.2.7 Conclusion

The conclusions of this experiment are:

- The accuracy of the quasi-static compliance breakdown method is very good. As the compliances of the beam in the vertical plane are decoupled from the other compliances of the beam, the accuracy of the quasi-static compliance breakdown method can be extrapolated to the global set of compliances of the beam. For most complex mechanical structures, an exception should be made for the longitudinal compliance of the component as in the longitudinal direction most components are very stiff, with respect the other directions, and the corresponding compliance becomes too small to determine. However, neglecting this compliance does not influence the accuracy of the quasi-static compliance breakdown method.
- Always determine the quasi-static compliances of a component of a structure from the absolute movement of **both** reference planes characterizing the compliant component.
- The influence of the inertial forces on the results of the quasi-static compliance breakdown is negligible, provided that the excitation frequency and the amplitude of the sinusoidal force are well chosen.

2.4.3 Quasi-static compliance breakdown of a KUKA IR 361/8.0 industrial robot

To demonstrate the general applicability of the quasi-static compliance breakdown method, the method has been used to determine the compliance model of a complex mechanical structure, such as an industrial robot. The robot used in this experiment is the KUKA IR 361/8.0 industrial robot with long wrist. Figure 2.17 shows, for a certain configuration, the KUKA IR 361.8.0 robot with its different joint frames (figure 2.17).

2.4.3.1 Kinematics of the KUKA robot

Table 2.3 contains the Denavit-Hartenberg parameters which describe the kinematics of the KUKA IR 361/8.0 robot in its reference con-

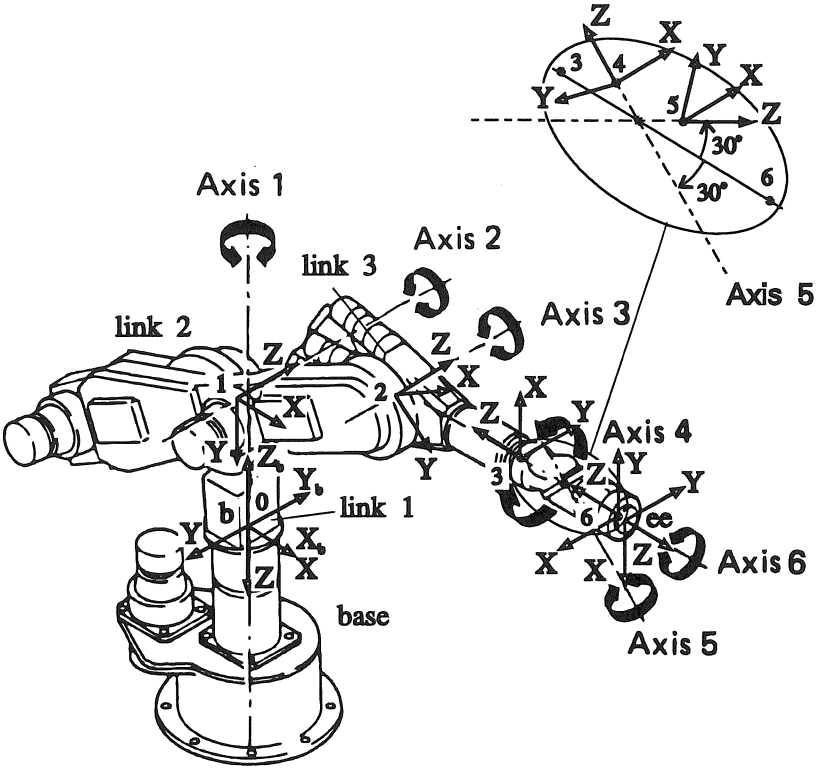

Figure 2.17: KUKA IR 361/8.0 industrial robot with its joint frames.

Joint frames					
joint	$\theta(0)$ (°)	d (mm)	a (mm)	α (°)	z_t (mm)
0	0	0.0	0.0	180	0.0
1	0	-440.0	0.0	90	-79.0
2	-90	0.0	480.0	0	-2.0
3	-90	81.0	0.0	90	-514.0
4	90	-131.0	0.0	30	46.2
5	0	-46.2	0.0	120	46.2
6	180	-46.2	0.0	150	-104.0
7	-90	-16.0	0.0	180	0.0

Table 2.3: Denavit-Hartenberg parameters of joint frames for KUKA IR 361/8.0 robot.

Link frames					
link	θ (°)	d (mm)	a (mm)	α (°)	z_t (mm)
0	0	0	0	180	0
1	0	79	0	90	0
2	90	-92	0	90	0
3	180	0	0	180	0

Table 2.4: Denavit-Hartenberg parameters of link frames for KUKA IR 361/8.0 robot.

figuration. In this configuration the robot is in an upright position. These parameters are defined in appendix D. To apply the Denavit-Hartenberg approach, the second joint of the triple-roll wrist of the KUKA robot (figure 2.18), or the fifth joint of the robot, needs to be decomposed into two separate joints, which operate always together. This results in seven joints for a six degrees-of-freedom robot, with q_5 always equaling q_6.

Table 2.4 contains the Denavit-Hartenberg parameters which describe the link frames with respect to the joint frames (see figure 2.19). For the compliance breakdown of the KUKA robot, only links 1 up to 3 are described since the other links can be considered rigid.

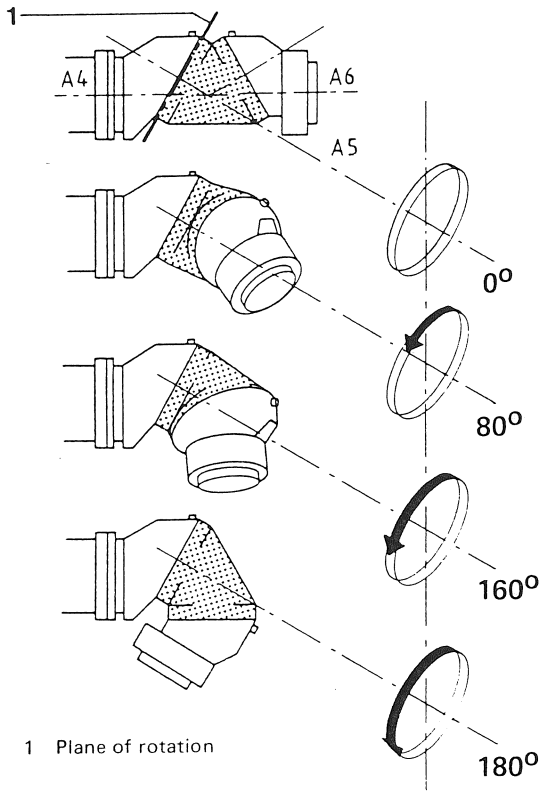

Figure 2.18: Triple-roll wrist of the KUKA robot.

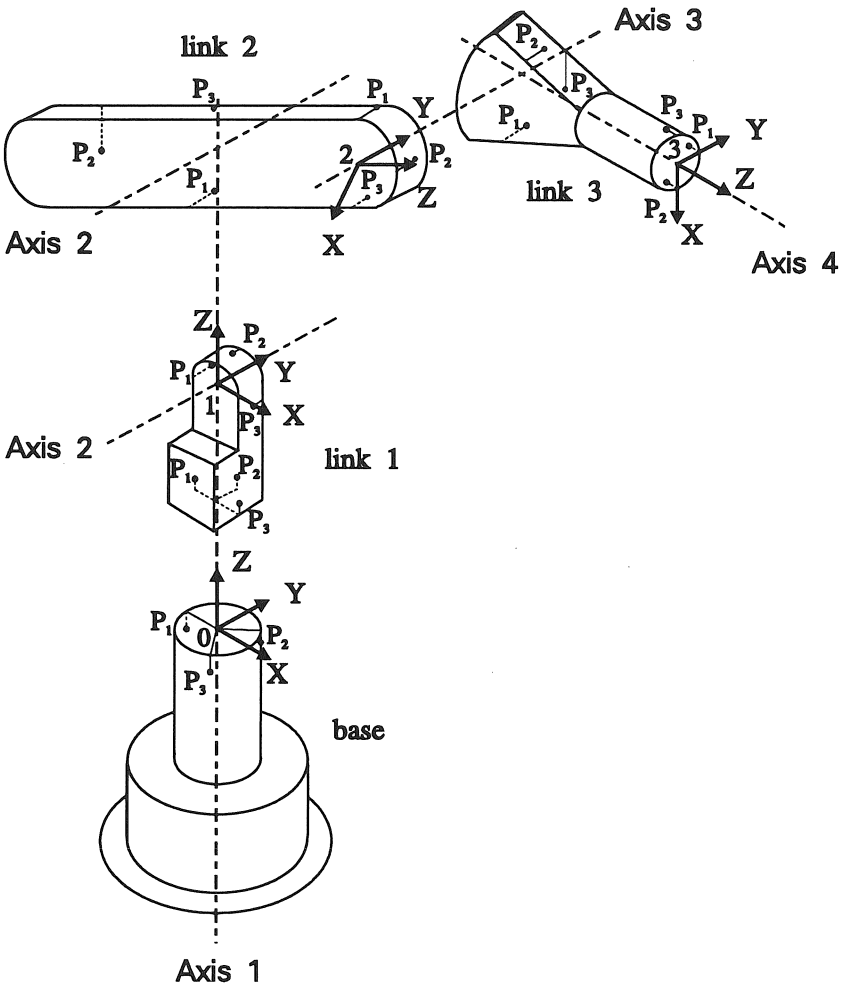

Figure 2.19: Schematic representation of the considered measuring points on the KUKA robot and of the corresponding link frames.

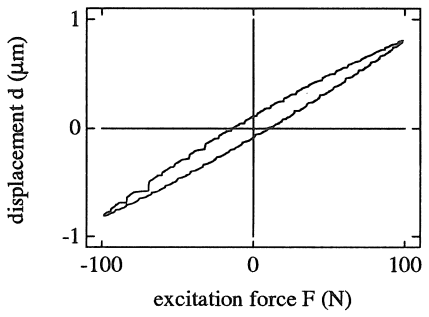

Figure 2.20: Global stiffness characteristic of the KUKA robot.

2.4.3.2 Static compliances of the joints of the KUKA robot

For a robot, the compliances of the joints are determined applying a static force at the end-effector. The torque at the joint is calculated using the geometry of the robot, while the rotation of the joint is calculated as the difference between the rotation about the joint axis of the link following the joint and the rotation about the joint axis of the link preceding the joint. Both rotations are measured by an autocollimator. For the compliance breakdown of the KUKA robot, only the compliance of the first three joints is measured.

The statically determined joint compliances are:

$$\begin{aligned} c_{j1} &= 2.281\ 10^{-6}\ rad/Nm, \\ c_{j2} &= 1.310\ 10^{-6}\ rad/Nm, \\ c_{j3} &= 3.715\ 10^{-6}\ rad/Nm. \end{aligned}$$

2.4.3.3 Global stiffness characteristic of the KUKA robot

Figure 2.20 shows the global stiffness characteristic of the KUKA robot. This characteristic is clearly characterized by hysteresis, so a static preload is necessary for the quasi-static measurements. The maximal permissible dynamic load for the KUKA IR 361/8.0 robot is $8kg$, while the maximal permissible static load is $15kg$. This results in following forces: a static preload F_0 with an amplitude of $80N$, and a quasi-static force with an amplitude of the sinusoidal part, F_a, of $40N$.

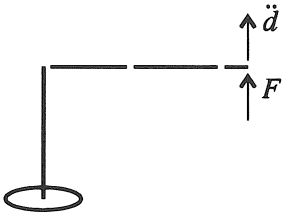

$$q_2 = 90°$$
$$q_3 = 0°$$

Figure 2.21: Schematic representation of the considered robot configuration.

2.4.3.4 Frequency response of the KUKA robot

Figure 2.21 gives a schematic representation of the considered robot configuration. The KUKA robot is excited by a vertical sinusoidal force at its end-effector. The accelerations are also measured at the end-effector. Figure 2.22 shows the frequency responses of the KUKA robot. The magnitude in the figures is the ratio between the displacement of the robot, derived by integrating twice the measured acceleration, and the measured excitation force. In the figures at the left, the horizontal displacement of the robot is considered while in the figures at the right the vertical displacement is considered.

The KUKA robot has its first natural frequency at 13 Hz, corresponding to a vibration mode in the horizontal plane, and its second natural frequency at 18 Hz, corresponding to a vibration mode in the vertical plane. The quasi-static range extends up to 5 Hz. To assure the quality of the measurements, the excitation frequency f_{qs} is chosen at 3 Hz. This gives a desired accuracy of 5% for compliances which cause deformations in the horizontal plane, and 3% for those which cause deformations in the vertical plane (cf. appendix A).

2.4.3.5 Quasi-static compliances of the KUKA robot

The KUKA robot is excited by a sinusoidal force with an amplitude F_a of $40N$ and a frequency f_{qs} of 3 Hz. A static preload F_0 of $80N$ is ap-

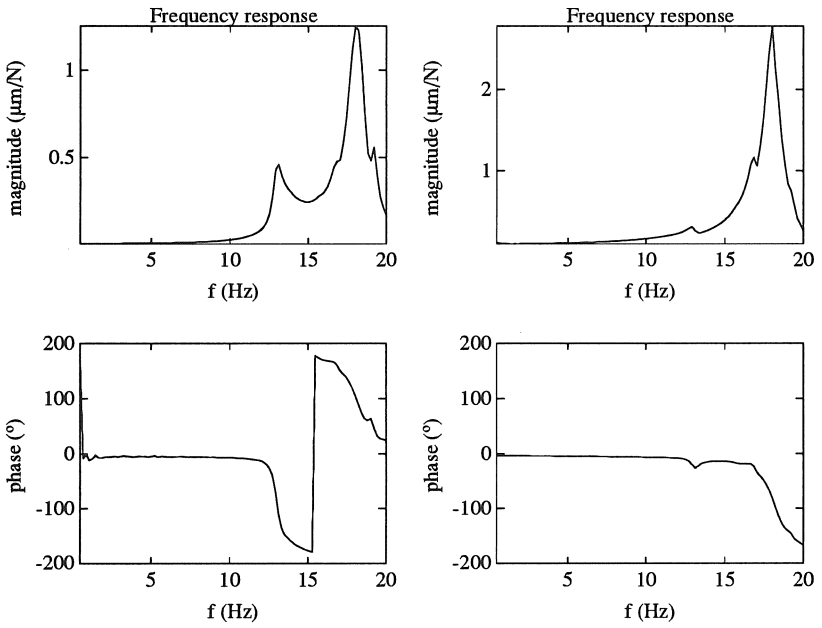

Figure 2.22: Frequency response of the KUKA robot. Left figures: horizontal displacement; right figures: vertical displacement.

Joint angles in °							
config.	q_1	q_2	q_3	q_4	q_5	q_6	q_7
1	-0.02	111.30	-21.69	0.00	-0.02	-0.02	-0.05
2	-0.10	116.16	-20.48	-29.90	-54.41	-54.41	-0.05
3	-0.10	80.09	43.79	-29.90	0.06	0.06	-0.15

Table 2.5: Robot configurations for the quasi-static measurements.

plied. The excitation force, applied at the end-effector of the robot, is measured by a piezo-electric load cell. The quasi-static measurements are performed for three independent robot configurations (table 2.5): The accelerations are measured at the different points located on the reference planes characterizing the compliant components of the robot (figure 2.19).

The results of the quasi-static compliance breakdown of the KUKA robot are discussed separately for:

- the joints of the robot;
- the links of the robot;
- the base of the robot.

2.4.3.5.1 Joints of the robot

For practical reasons, the compliance of the different joints has been measured with the brakes on and the robot controller off. As the brakes are fixed directly on the actuator shafts the brakes on or off do not influence the compliance of the mechanical transmission between the actuator and the joint. As mentioned earlier, only the compliance of the first three joints is measured.

The results of the quasi-static compliance breakdown of the joints are:

$$\begin{aligned} c_{j1} &= 2.393\ 10^{-6}\ rad/Nm, \\ c_{j2} &= 1.295\ 10^{-6}\ rad/Nm, \\ c_{j3} &= 3.789\ 10^{-6}\ rad/Nm. \end{aligned}$$

The comparison between the quasi-static compliances of the joints of the KUKA robot and the statically determined ones (table 2.6) shows that the accuracy of the quasi-static compliance breakdown

joint	unit	static	quasi-static	$\Delta\frac{q}{s}$
c_{j1}	*rad/Nm*	2.281 10^{-6}	2.393 10^{-6}	-4.7%
c_{j2}	*rad/Nm*	1.310 10^{-6}	1.295 10^{-6}	1.1%
c_{j3}	*rad/Nm*	3.715 10^{-6}	3.789 10^{-6}	-2.0%

Table 2.6: Quasi-static vs. static compliances of the joints of the KUKA robot.

method, used to determine the compliance of the joints of a complex mechanical structure, is very good.

2.4.3.5.2 Links of the robot

As mentioned earlier, only links 1 up 3 are measured; the other links can be considered rigid. At least two independent robot configurations are necessary to determine the 8 parameters of a compliant link (section 2.2.2.3): link 1 is measured in two independent robot configurations, links 2 and 3 are measured in three independent robot configurations.

Table 2.7 shows the results of the quasi-static compliance breakdown of the links for different combinations of robot configurations. Some combinations of robot configurations for link 2 and 3 are not given because almost the same loads are applied to the links. In this table, the longitudinal compliance of the link, $c3$, is not given because it is too small to be measured; $c3$ is set automatically equal to zero.

An examination of this table reveals that, for different combinations of configurations (cf. link 2) different values are found for the compliances, and that for some compliances even negative values are found, which have been replaced by —. So, the accuracy of the quasi-static compliance breakdown method, used to determine the compliances of the links of a complex mechanical structure, is poor. The reasons for these poor results are:

1. The measured links are very rigid so the deformations are very small; the difference between the translations of the two reference planes characterizing the compliant link is only a few micrometers for the applied force.

2. The determination of the absolute movement of the reference plane, characterizing the compliant component, out of the trans-

		Link 1	Link 2		Link 3
		config.	config.	config.	config.
compl.	unit	2+3	1+2	1+3	2+3
$c1$	$10^{-6}\ m/N$	0.20	1.56	—	0.97
$c2$	$10^{-6}\ m/N$	0.01	2.29	2.60	0.61
$c4$	$10^{-6}\ rad/Nm$	1.52	4.83	5.68	18.68
$c5$	$10^{-6}\ rad/Nm$	0.36	3.85	—	7.27
$c6$	$10^{-6}\ rad/Nm$	0.64	1.36	3.69	3.78
$c7$	$10^{-6}\ 1/N$	0.18	—	3.79	—
$c8$	$10^{-6}\ 1/N$	—	—	—	—

Table 2.7: Results of the quasi-static compliance breakdown of the links of the KUKA robot.

lational acceleration measurements is badly conditioned. Especially, the determination of the rotation angles of the reference plane poses a lot of problems because (1) the contribution of these angles to the measurements is very small with respect to those of the translations (about 1%), and (2) the accuracy of the position and orientation data of the measuring points with respect to the reference plane frame influences the accuracy of the determination. The determination of the compliances of the link also being based on these rotation angles explains for the greater part the poor results of the quasi-static compliance breakdown of the links of the robot.

3. The measured links are not really *ideal* beams (see figure 2.17).

Recently, *angular* accelerometers [63, 64] have become commercially available. Such a triaxial angular accelerometer can measure **directly** the rotation angles of a reference plane. This makes the determination of the absolute movement of the reference plane a lot easier, and, more important, a lot more accurate. This solves the biggest problem for having an accurate quasi-static compliance breakdown of the links of a complex mechanical structure.

2.4.3.5.3 Base of the robot

Table 2.8 shows the results of the quasi-static compliance breakdown of the base of the robot. For the compliance breakdown, a diagonal

compl.	unit	config.1	config.2	config.3
$c1_b$	$10^{-6}\ m/N$	14.62	—	—
$c2_b$	$10^{-6}\ m/N$	24.92	0.08	0.10
$c3_b$	$10^{-6}\ m/N$	0.02	0.03	0.03
$c4_b$	$10^{-6}\ rad/Nm$	48.34	14.29	1.73
$c5_b$	$10^{-6}\ rad/Nm$	0.21	0.20	0.17
$c6_b$	$10^{-6}\ rad/Nm$	—	—	—

Table 2.8: Results of the quasi-static compliance breakdown of the base of the KUKA robot.

base compliance matrix has been used.

Like for the quasi-static compliance breakdown of the links of the robot, the determination of the absolute movement of the base plane of the robot poses the biggest problem for having an accurate quasi-static compliance breakdown of the base of a complex mechanical structure. Using at one measuring point of the base plane a triaxial angular accelerometer could solve this problem.

2.4.3.6 Conclusion

The experiment with the KUKA robot shows that the quasi-static compliance breakdown method is very appropriate to determine the compliance of the joints of a complex mechanical structure. On the other hand, the determination of the compliance parameters of the links and of the base of the robot poses some problems. The use of a triaxial *angular* accelerometer, which has become only recently available, besides the triaxial *translational* accelerometer solves the biggest problem for having an accurate quasi-static compliance breakdown of the links and of the base of a complex mechanical structure. However, the, for the moment, commercially available angular accelerometers are not suited for this type of application: especially their sensitivity to rotational accelerations is far too low. The choice of the most appropriate compliance model for the different components of the complex mechanical structure remains very important.

2.4.4 The corresponding software

The software package, developed within this thesis, determines a static compliance model of an industrial robot based on quasi-static measurements. This software package is called **ROBOFLEX**.

The software is robot-independent, with the restriction that only serial driven robots can be modelled. The different components for which an appropriate compliance model is available are: prismatic long links, revolute joints, and robot bases with a diagonal compliance matrix. However, the software is built modular so other components and other compliance models can be easily added.

The program consists of three parts: (1) a data initialization part, (2) a quasi-static measurement part, and (3) a compliance modelling part. In this third part, an analysis of the compliance of the robot within its workspace is implemented. Section 2.3.3 shows an example of such a workspace analysis. The data transfer between the different parts is realized through ASCII files. Appendix E gives a more detailed description of this software package.

The corresponding software has been developed in Turbo Pascal 5.0 [65].

2.5 Conclusion

The *quasi-static* compliance breakdown technique that has been developed, implemented and tested within this chapter allows to determine *configuration-independently* the compliances of the different components of complex mechanical structures. This new method permits to determine the compliances of a component without measuring the whole robot.

In this thesis, the compliance breakdown of serial driven industrial robots has been emphasized. For this type of robots following components have been considered: prismatic long links, revolute joints and the robot base. Because of the modular structure of this technique other types of components and other compliance models can be easily included.

To perform an accurate compliance breakdown, a new method has been developed to correct the influence of gravitation on translational accelerometer measurements. The author is not aware of the existence

of any other method which compensates the influence of gravitation on translational accelerometer measurements, although it is essential. In fact, all people using translational accelerometer measurements encounter this phenomenon, but as they measure at higher frequencies they neglect, in many cases without knowing, this influence.

The results of the compliance breakdown contribute to potential improvement of robot precision in several ways; such as in robot design improvement, in the prediction and compensation of robot end-point deflection, or in the selection of, for a given task, best robot posture and best workpiece position with respect to the robot arm. For those different applications, some approaches encountered in literature are discussed. For the latter application, software has been developed which allows to analyze the spatial deformation behaviour of a robot within its workspace.

The experimental compliance breakdown performed on a clamped-free beam shows that the accuracy of the quasi-static compliance breakdown method is very good, and that the influence of the inertial forces on the results of the quasi-static compliance breakdown is negligible, provided that the excitation frequency is well chosen. The experimental compliance breakdown performed on an industrial robot shows that the quasi-static compliance breakdown method is very appropriate to determine the compliance of the joints of a complex mechanical structure. On the other hand, the determination of the compliance parameters of the links and of the base of the robot poses some problems. Theoretically, the use of an angular accelerometer beside the already used translational accelerometer could solve the biggest problem for having an accurate quasi-static compliance breakdown of the links and of the base of a complex mechanical structure. However, the at the moment commercially available angular motion sensors are not usable for this type of application: especially their sensitivity to angular motion is far too low. The choice of the most appropriate compliance model for the different components of the complex mechanical structure remains very important. Based on the experiences with these experiments, following important conclusions can be drawn:

- the quasi-static measurement and the compliance breakdown should be *performed very carefully*;
- the quasi-static measurement could be improved using beside

translational accelerometers also *angular* accelerometers.

For both the quasi-static measurement and the compliance breakdown, some general precautions to prevent errors are discussed.

Finally, within this thesis a software package, called **ROBOFLEX**, has been developed which allows to determine a static compliance model of an industrial robot based on quasi-static measurements. The software is robot-independent, with the restriction that only serial driven robots can be modelled. The different components for which an appropriate compliance model is available are: prismatic long links, revolute joints, and robot bases with a diagonal compliance matrix. However, the software is built modular so other components and other compliance models can be easily added.

Chapter 3

Real-time link deflection measurement

3.1 Introduction

To control the structural deflections and vibrations of a flexible link, the knowledge of the position of the tip of the link is essential [21]. The position of the tip of a flexible link can be determined by using the information of the encoder or by measuring the structural deflections at the tip of the link.

Section 1.3 has shown that strain gauges and optical detectors are suitable devices to build a link deflection sensor. In this chapter, both methods are investigated and tested for the desired features of a link deflection sensor, which should be able to determine in *real-time* the *spatial* structural deflections of a flexible link.

3.2 Flexible link deflections

The deflections to measure are those at the tip of each flexible link of the robot. This measurement is crucial because those deflections determine the position of the tip of the link, and affect the position and orientation of the robot end-effector [46]. Figure 3.1 defines those deflections. Frame $\{X_0, Y_0, Z_0\}$, $= \{0\}$, represents the tip of the straight link before deflection. The Z-axis is in the direction of the neutral axis of the link. The frame $\{X_{0'}, Y_{0'}, Z_{0'}\}$, $= \{0'\}$, represents the tip

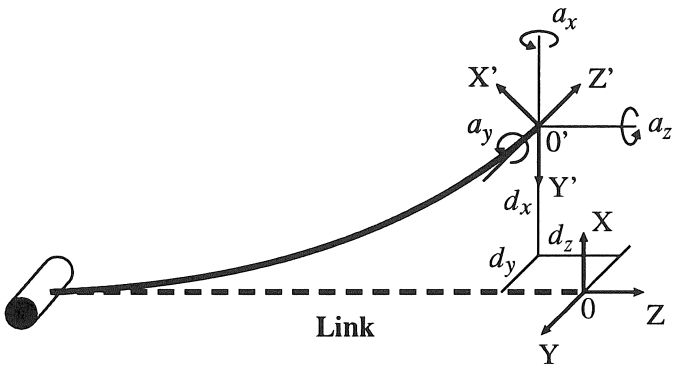

Figure 3.1: Structural deflections of a robot link.

of the link after deflection. The description of the deformed link frame {0'} with respect to the undeformed link frame {0} is given by the homogeneous transform ${}^0\mathbf{A}_{0'}$ (appendix B), defined by:

$$ {}^0\mathbf{A}_{0'} = \begin{bmatrix} c_z c_y & -s_z c_x + c_z s_y s_x & s_z s_x + c_z s_y c_x & d_x \\ s_z c_y & c_z c_x + s_z s_y s_x & -c_z s_x + s_z s_y c_x & d_y \\ -s_y & c_y s_x & c_y c_x & d_z \\ 0 & 0 & 0 & 1 \end{bmatrix}, \quad (3.1) $$

where c_i=cos a_i and s_i=sin a_i, for i=x, y, z, and where d_x, d_y, d_z, a_x, a_y and a_z are the deflections to be measured. d_x, d_y and d_z are the components, along the proper axes of the undeformed link frame {0}, of the translation of frame {0'} relative to frame {0}. a_x, a_y and a_z are the components, about the proper axes of the undeformed link frame {0}, of the rotation of frame {0'} relative to frame {0}.

For very small rotations, the trigonometrical functions are linearized, for i=x, y, z,

$$ \begin{aligned} c_i &= 1, \\ s_i &= a_i; \end{aligned} $$

and higher order terms like $s_y s_x$, $s_z s_x$ and $s_z s_y$ can be neglected. The homogeneous transform ${}^0\mathbf{A}_{0'}$ becomes

$$ {}^{0}\mathbf{A}_{0'} = \begin{bmatrix} 1 & -a_z & a_y & d_x \\ a_z & 1 & -a_x & d_y \\ -a_y & a_x & 1 & d_z \\ 0 & 0 & 0 & 1 \end{bmatrix}. \tag{3.2} $$

3.3 Strain gauges based link deflection measurements

In this section, a method is investigated to determine the structural deflections of a robot arm by means of strain gauges. Strain gauges do not measure the deflections directly. The relation between the strain measured at a particular point of the link and the structural deflections at the tip of the link is not unique, but depends on how the strain changes along the link. However, this change is uniquely determined by the loads acting on the link. A number of strain gauge measurements are used to reconstruct the same number of loads acting on the link directly as a weighted sum. The combination of these loads with an extended compliance model of the link, cf. section 2.2.2.1, results in the desired deflections.

This shows that with link deflection measurements based on strain gauges the knowledge of the loads acting on the link is important, contrary to for instance optical link deflection measurement systems.

3.3.1 Relation between strain gauges measurements and structural deflections

3.3.1.1 Loads acting on a link

A link of a robot is considered a clamped-free beam. The clamping corresponds to the rigid connection between the joint and the link. The load acting on a link in motion generally consists of a force and a moment applied at the tip of the link, and of inertial and gravity forces which involve a distributed load for the beam. Not all components are always as significant, but a general approach should take into account all occurring influences.

However, the load acting on a link in motion is not known and should be measured. This is possible because each external load corresponds to a specific internal stress distribution. By measuring the

stress on different places on the structure, the different external loads can be determined. Stress itself cannot be measured; on the other hand strain can be measured using strain gauges. The stress follows from HOOKE's law:

$$\begin{aligned} \sigma &= e\,E, \\ \tau &= \gamma\,G, \end{aligned}$$

where : σ : yield stress;
e : strain;
E : YOUNG's modulus of elasticity;
τ : shear stress;
γ : shear angle;
G : shear modulus.

The material is supposed to be homogeneously isotropic. The application of this theory on composite materials is not obvious.

The loads and corresponding deflections are considered into two groups:

1. along and about the main axes of inertia of a cross section of the beam;
2. along and about the longitudinal axis of the beam.

The loads along and about the main axes of inertia of a cross section of the beam result in a bending of the beam. These loads include the force components along and the moment components about the X- and Y-axis at the tip of the beam (figure 3.1), and the inertial and gravity forces. The force component along the Z-axis results in an elongation or a shortening of the beam. The elongation or shortening of the beam, d_z is difficult to measure and is not considered. Since d_z is usually very small compared to the other deflections, neglecting d_z causes no real error. The moment component about the Z-axis results in a torsion of the beam.

3.3.1.1.1 Loads along and about the main axes of inertia of a cross section of the beam

Since the strains encountered within this application are very small, it is important to measure those strains which are the largest. Strains due

to yield stress are the obvious strains to measure. For links, yield stress usually is a magnitude larger than shear stress. By putting several strain gauges into one bridge, cross influences, for instance due to shear stress, and influences of temperature, are eliminated. Furthermore, yield stress contains all information about the loads along and about the main axes of inertia of a cross section of the beam. By considering the loads along and about the main axes of inertia of a cross section of the beam, the formulas from the theory of strength of materials for bending are valid. The NAVIER formula defines the relation between the local yield stress and the local bending moment:

$$\sigma_{z'}(z') = \frac{M_{by}(z')\,x}{I_{yy}},$$

where : z' : distance along $-Z$-axis;
$M_{by}(z')$: local bending moment about Y-axis;
x : distance to Y-axis;
I_{yy} : moment of inertia about Y-axis.

The local strain becomes:

$$e_y(z') = \frac{M_{by}(z')\,x}{E\,I_{yy}}.$$

This formula only considers the bending about the Y-axis. For the bending about the X-axis, the same formulas are valid, but then related to the X-axis instead of the Y-axis. Both cases can be dealt with individually.

The bending moment M_{by} is caused by the force components along the X-axis and the moment components about the Y-axis at the tip of the beam, as well as by the inertial and gravity forces. On condition that a perfect elastic stress-strain behaviour can be assumed, the bending moment M_{by} can be considered a linear superposition of the bending moments due to the different load components. The different influences are:

- due to load components at the tip of the beam

$$M_{by}(z') = F_x\,z' + M_y;$$

- due to gravity forces

$$M_{by}(z') = \int_0^{z'} g\,\cos\theta_y\,\rho\,A(z')\,z'\,dz';$$

- due to inertial forces

$$M_{by}(z') = \int_0^{z'} [a_{0x} + r\,\dot{\omega}_y + r\,(\omega \times \omega)_y]\,\rho\,A(z')\,z'\,dz',$$

where : θ_y : angle between the X-axis and the gravity vector about the Y-axis;
ρ : specific mass of the material;
$A(z')$: area of the cross section through x-y;
a_{0x} : x-component of translational acceleration of the beam;
r : $l - z'$, with l the length of the beam;
$\dot{\omega}_y$: y-component of rotational acceleration of the beam;
ω : rotational velocity vector of the beam.

The velocity and acceleration components of the beam are due to the motion of the previous links of the robot and due to the own motion, and are independent of z'.
The resulting local strain becomes:

$$e_y(z') = b_i^{F_x} F_x + b_i^{M_y} M_y + b_i^{a_{0x}} a_{0x} + b_i^{g_x} g \cos\theta_y + b_i^{\dot{\omega}_y} \dot{\omega}_y + b_i^{\omega_y} (\omega \times \omega)_y. \tag{3.3}$$

These formulas are valid across the whole length of the beam. The strain can be measured at each point on the beam. The proportionality factors can be calculated by means of the formulas from the theory of strength of materials, taking into account the geometry of the beam, the material properties and the position of the strain gauges. The equations to calculate the proportionality factors b for strain gauge i, located at a distance z' from the tip of the link and at a distance $\frac{h}{2}$ to the Y-axis, are:

$$\begin{aligned}
b_i^{F_x} &= \frac{z'\,h}{2\,E\,I_{yy}}; \\
b_i^{M_y} &= \frac{h}{2\,E\,I_{yy}}; \\
b_i^{g_x} &= \frac{h}{2\,E\,I_{yy}} \int_0^{z'} z'\,dm; \\
b_i^{a_{0x}} &= \frac{h}{2\,E\,I_{yy}} \int_0^{z'} z'\,dm;
\end{aligned}$$

$$b_i^{\omega_y} = \frac{h}{2\,E\,I_{yy}} \int_0^{z'} (l - z')\, z'\, dm;$$
$$b_i^{\dot{\omega}_y} = \frac{h}{2\,E\,I_{yy}} \int_0^{z'} (l - z')\, z'\, dm; \tag{3.4}$$

where : h : height of the beam;
dm : $\rho\, A(z')\, dz'$.

However, the proportionality factors $b_i^{g_x}$ and $b_i^{a_{0x}}$ on the one hand, and $b_i^{\omega_y}$ and $b_i^{\dot{\omega}_y}$ on the other hand are equal. So, equation 3.3 becomes simplified:

$$e_y(z') = b_i^{F_x} F_x + b_i^{M_y} M_y + b_i^{ga_{0x}} (g \cos\theta_y + a_{0x}) + b_i^{\omega\dot{\omega}_y} [(\boldsymbol{\omega} \times \boldsymbol{\omega})_y + \dot{\omega}_y] \tag{3.5}$$

and written in matrix notation, for n different values of z':

$$\mathbf{e}_y = \mathbf{B}_y\, \mathcal{F}_y \tag{3.6}$$

where :

$$\mathcal{B}_y = \begin{bmatrix} b_1^{F_x} & b_1^{M_y} & b_1^{ga_{0x}} & b_1^{\omega\dot{\omega}_y} \\ \vdots & \vdots & \vdots & \vdots \\ b_n^{F_x} & b_n^{M_y} & b_n^{ga_{0x}} & b_n^{\omega\dot{\omega}_y} \end{bmatrix}, \tag{3.7}$$

$$\mathcal{F}_y = \begin{bmatrix} F_x \\ M_y \\ g\cos\theta_y + a_{0x} \\ (\boldsymbol{\omega} \times \boldsymbol{\omega})_y + \dot{\omega}_y \end{bmatrix}. \tag{3.8}$$

Only four unknown load components remain and should be determined in *real-time*. By measuring the strain at four different positions, the system is completely determined (i=1-4). Inverting equation 3.6 gives the desired loads:

$$\mathcal{F}_y = \mathbf{B}_y^{-1}\, \mathbf{e}_y \tag{3.9}$$

or with $\mathbf{B'}_y = \mathbf{B}_y^{-1}$

$$\mathcal{F}_y = \mathbf{B'}_y\, \mathbf{e}_y. \tag{3.10}$$

Most of the on-line calculations can be done in advance: for each setup the proportionality factors b are constant and the inversion

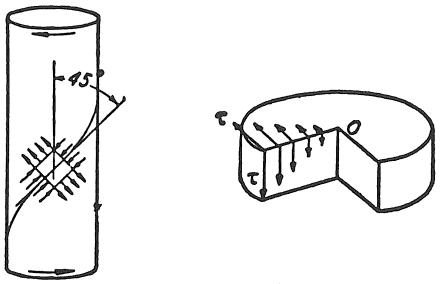

Figure 3.2: Shear stress due to pure torsion.

should only happen once, off-line. The on-line calculations are limited to the product $\mathbf{B'}_y\,\mathbf{e}_y$, which corresponds to 12 additions and 16 multiplications for each main axis of inertia.

A better method to determine the proportionality factors b is by calibration. For a *given* set of loads the strain at the different positions is measured. Solving the system of equations gives the proportionality factors b. Some advantages are: the geometry and the material properties of the beam, and the position of the strain gauges should not be known accurately, in addition this procedure takes into account the offset errors of the measurement equipment.

3.3.1.1.2 Loads about the longitudinal axis of the beam

As mentioned above, the influence of forces along the longitudinal axis is negligible. Only the moment component about the longitudinal axis is considered.

A load about the longitudinal axis can produce large deformations. An external moment of torsion is kept balanced by an internal moment of torsion. This internal moment produces shear stresses, lying in a plane perpendicular to the longitudinal axis. These stresses are zero at the axis and maximal at the surface (figure 3.2). The value of the maximal shear stresses depends on the shape of the cross section. However, shear stresses cannot be measured directly. From the circle of Mohr (figure 3.3) follows that these shear stresses give rise for yield stresses which are maximal at an angle of 45° with respect to the shear stresses [66].

In the theory of strength of materials, or in the theory of elasticity of materials, there exists no general formula to calculate the shear

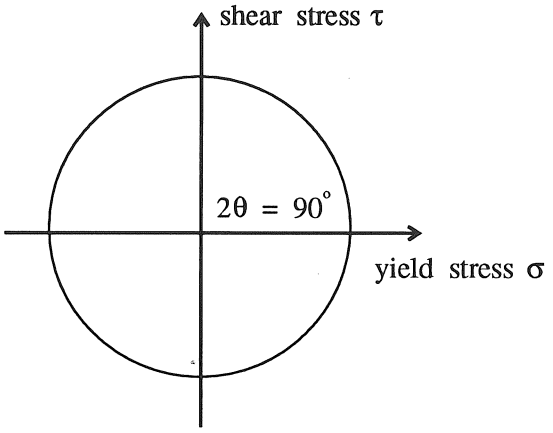

Figure 3.3: Circle of Mohr for pure torsion.

stresses due to pure torsion. All depends on the cross section of the beam. However, the relation between the shear stress and the moment of torsion is linear:

$$\tau = b^{\tau}_{M_z} M_z.$$

For a strain gauge, put at an angle of 45° with respect to the longitudinal axis, following relations apply:

$$\begin{aligned} \sigma &= b^{\sigma}_{M_z} M_z, \\ e_z &= b^{e}_{M_z} M_z. \end{aligned} \tag{3.11}$$

Calibration is again the appropriate way to determine $b^{e}_{M_z}$.

3.3.1.1.3 Loads acting on the link

Using equation 3.10 for both main axes of inertia of a cross section, and equation 3.11 for the longitudinal axis, determines in combination with the 9 strain measurements the global load acting on the link:

$$\begin{bmatrix} \mathcal{F}_x \\ \mathcal{F}_y \\ M_z \end{bmatrix} = \begin{bmatrix} \mathbf{B'}_x & & \\ & \mathbf{B'}_y & \\ & & b'_{M_z} \end{bmatrix} \begin{bmatrix} \mathbf{e}_x \\ \mathbf{e}_y \\ e_z \end{bmatrix}. \tag{3.12}$$

Theoretically, the blank elements of the matrix are zero. Due to misalignment errors, non-linearities and other error sources, those elements are not zero because the strain gauges also measure strains due to the other forces and moments. Those cross-influences are determined by calibrating the *global* strain gauges measurement system (equation 3.12).

3.3.1.2 Extended compliance modelling

The loads acting on the link in combination with an extended compliance model of that link give the desired structural deflections of the link.

The relation between the structural deflections of a beam and the loads applied at the tip of the beam is described in section 2.2.2.1. Links can be modelled as long, symmetric beams. The standard beam theory provides the compliance matrix $\mathbf{C}_{tip}$. As mentioned above, the elongation of the beam, d_z, and the influence of the force along the longitudinal axis, F_z, is negligible. The relation becomes:

$$\begin{bmatrix} d_x \\ d_y \\ a_x \\ a_y \\ a_z \end{bmatrix} = \begin{bmatrix} c_{d_x}^{F_x} & 0 & 0 & c_{d_x}^{M_y} & 0 \\ 0 & c_{d_y}^{F_y} & c_{d_y}^{M_x} & 0 & 0 \\ 0 & c_{a_x}^{F_y} & c_{a_x}^{M_x} & 0 & 0 \\ c_{a_y}^{F_x} & 0 & 0 & c_{a_y}^{M_y} & 0 \\ 0 & 0 & 0 & 0 & c_{a_z}^{M_z} \end{bmatrix} \begin{bmatrix} F_x \\ F_y \\ M_x \\ M_y \\ M_z \end{bmatrix} \tag{3.13}$$

or written in matrix notation:

$$\mathcal{D}_{tip} = \mathbf{C}_{tip}\,\mathcal{F}_{tip}.$$

Section 2.2 describes a method to calibrate the compliance factors c.

To take into account the inertial and gravity forces working on the beam, the compliance matrix $\mathbf{C}_{tip}$ need to be extended. The equations to calculate the structural deflections taking into account the inertial and gravity forces are:

$$d_x = c_{d_x}^{F_x} F_x + c_{d_x}^{M_y} M_y + c_{d_x}^{a_{0x}} a_{0x} + c_{d_x}^{g_x} g \cos\theta_y + c_{d_x}^{\dot{\omega}_y} \dot{\omega}_y + c_{d_x}^{\omega_y} (\boldsymbol{\omega} \times \boldsymbol{\omega})_y,$$

$$a_y = c_{a_y}^{F_x} F_x + c_{a_y}^{M_y} M_y + c_{a_y}^{a_{0x}} a_{0x} + c_{a_y}^{g_x} g \cos\theta_y + c_{a_y}^{\dot{\omega}_y} \dot{\omega}_y + c_{a_y}^{\omega_y} (\boldsymbol{\omega} \times \boldsymbol{\omega})_y.$$

Again, the proportionality factors c^{g_x} and $c^{a_{0x}}$ on the one hand, and c^{ω_y} and $c^{\dot{\omega}_y}$ on the other hand are equal. The equations become simplified:

$$d_x = c_{d_x}^{F_x} F_x + c_{d_x}^{M_y} M_y + c_{d_x}^{ga_{0x}} (g \cos\theta_y + a_{0x}) + c_{d_x}^{\omega\dot{\omega}_y} [(\boldsymbol{\omega} \times \boldsymbol{\omega})_y + \dot{\omega}_y], \tag{3.14}$$

$$a_y = c_{a_y}^{F_x} F_x + c_{a_y}^{M_y} M_y + c_{a_y}^{ga_{0x}} (g \cos\theta_y + a_{0x}) + c_{a_y}^{\omega\dot{\omega}_y} [(\boldsymbol{\omega} \times \boldsymbol{\omega})_y + \dot{\omega}_y]. \tag{3.15}$$

These equations only consider the bending about the Y-axis. For the bending about the X-axis, the same equations are valid, but then related to the X-axis instead of the Y-axis.
The compliance factors c related to the inertial and gravity forces are calibrated by applying a *given* set of translational and rotational accelerations to the beam and by measuring at the same time the deflections at the tip of the beam using accelerometers. Solving the system of equations yields the desired compliance factors.

The extended compliance matrix $\mathbf{C}$ becomes:

$$\mathbf{C} = \begin{bmatrix} & & c_{d_x}^{ga_{0x}} & 0 & 0 & c_{d_x}^{\omega\dot{\omega}_y} \\ & & 0 & c_{d_y}^{ga_{0y}} & c_{d_y}^{\omega\dot{\omega}_x} & 0 \\ \mathbf{C}_{tip} & & 0 & c_{a_x}^{ga_{0y}} & c_{a_x}^{\omega\dot{\omega}_x} & 0 \\ & & c_{a_y}^{ga_{0x}} & 0 & 0 & c_{a_y}^{\omega\dot{\omega}_y} \\ & & 0 & 0 & 0 & 0 \end{bmatrix}. \tag{3.16}$$

The link deflections are given by the scalar equation

$$\mathcal{D}_{tip} = \mathbf{C}\,\mathcal{F} \tag{3.17}$$

where :

$$\mathcal{F} = \begin{bmatrix} \mathcal{F}_{tip} \\ \\ g \cos\theta_y + a_{0x} \\ g \cos\theta_x + a_{0y} \\ (\boldsymbol{\omega} \times \boldsymbol{\omega})_x + \dot{\omega}_x \\ (\boldsymbol{\omega} \times \boldsymbol{\omega})_y + \dot{\omega}_y \end{bmatrix}.$$

3.3.1.3 Strain gauges based link deflection measurements

To use equation 3.12 in combination with equation 3.17, the rows of equation 3.12 should be rearranged. The force vectors of both equations contain the same elements but in a different order. Equation 3.12 becomes:

$$\mathcal{F} = \mathbf{B}'\,\mathbf{e}. \tag{3.18}$$

The general equation relating the desired structural deflections to the strain gauges measurements is found by combining equation 3.17 with equation 3.18.

$$\begin{aligned} \mathcal{D}_{tip} &= \mathbf{C}\,\mathcal{F} \\ \mathcal{F} &= \mathbf{B}'\,\mathbf{e} \end{aligned}$$

or,

$$\mathcal{D}_{tip} = \mathbf{C}\,\mathbf{B}'\,\mathbf{e} \tag{3.19}$$

The matrix $\mathbf{C}$ contains the extended compliance factors of the link, the matrix $\mathbf{B}'$ contains the proportionality factors between the strains and the loads on the link. Both matrices are constant for each setup. The multiplication of both matrices should only happen once, off-line. The on-line calculations are limited to the product $(\mathbf{C}\,\mathbf{B}')\,\mathbf{e}$, which corresponds to 40 additions and 45 multiplications.

3.3.2 Experimental setup

A flexible, clamped-free beam is the ideal structure to verify the above proposed theory. It allows

1. to compare the calibrated proportionality and compliance factors to the theoretical determined ones,
2. to verify the applicability of strain gauges based link deflection measurements.

For reasons of symmetry, only deflections in the vertical plane and torsion are considered.

3.3.2.1 Description of the experimental setup

Figure 3.4 gives a top view of the experimental setup. The values mentioned in the figure are expressed in *mm*. The setup consists of

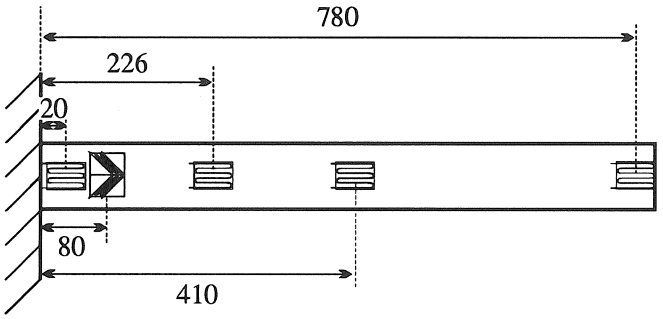

Figure 3.4: Top view of the experimental setup.

a flexible clamped-free beam. Four strain gauge measurements are used to determine the deflections in a vertical plane. One strain gauge measurement is used to determine the torsion angle. To increase the sensitivity of the strain measurements, for each strain measurement not one but four strain gauges are used: two on top of the beam and two at the underside of the beam. Putting for both pair of strain gauges the two strain gauges mounted at the same side of the beam into two opposite branches of a Wheatstone bridge multiplies by four the measured strain. Beside the multiplication of the measured strain this method automatically compensates for the influences of traction and compression, and of temperature. For the measurement of the torsion angle special strain gauges which measure yield stresses at 45° and −45° with respect to the longitudinal axis are used.

3.3.2.2 Results of the experiments

Only the results of the experiments will be described within this section. A more detailed description of the experiments is given in [67].

3.3.2.2.1 Comparison between the calculated and the calibrated proportionality and compliance factors

The calculation of the proportionality and compliance factors is based on the formulas from the theory of strength of materials. The calibration is based on three different methods:

- the factors due to forces and moments are calibrated by applying pure forces and moments at the end of the beam;

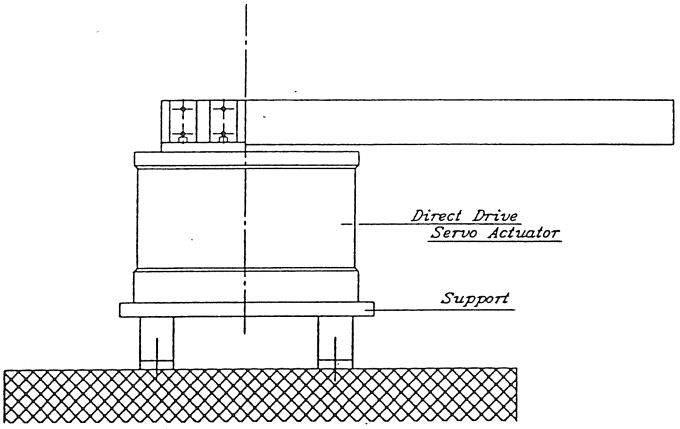

Figure 3.5: Beam mounted on a direct drive motor.

- the factors due to translational accelerations are calibrated by measuring both the strains with the beam in a vertical position and in a horizontal position. The difference between the strains measured in both positions divided by $9.81\frac{m}{s^2}$ gives the desired factors;
- the factors due to rotational accelerations are calibrated by mounting the beam on a direct drive motor (see figure 3.5), which realizes a pure sinusoidal rotational acceleration.

The theoretical and the experimental determined values of the proportionality and compliance factors correspond very well: $< 10\%$. Calibration of the different factors offers the possibility to determine cross-influences. Those cross-influences appear to be very important. However, most of these cross-influences can be explained by misalignment errors. For precision strain gauges [68], a cross-influence of about 1% is specified.

In this case only a simple structure is considered. For more complex structures, like for example a robot, both the theoretical and the experimental determination of these factors, and of the corresponding cross-influences, becomes much more complicated, for certain factors perhaps almost impossible.

3.3.2.2.2 Link deflection measurements

With this setup only deflections due to forces and moments applied at the end of the beam could be considered. Both for pure bending

and pure torsion the errors are about 1%. In the case of arbitrary applied forces and moments at end of the beam these errors increase significantly (about 10%). This shows the importance of the cross-influences.

3.3.2.3 Conclusions

The conclusions of these experiments are:

1. Strain gauges based deflection measurement of a robot link is feasible.

2. The accuracy of the measurements is limited since for practical applications the many factors of proportionality and compliance need to be determined with calibration procedures which are in this case difficult to carry out with adequate precision.

3. The measured strain is very small; the strain gauges are used at one to five percent of their range. Parasitic effects become important. Strain gauges based link deflection measurement becomes interesting for very flexible or very large robot links, such as the links of space robots, since other methods are not able to measure such large deflections.

4. A major disadvantage of this system is the impossibility to determine the deflections due to unexpected loads; a force applied not at the tip of the link is misinterpreted.

These conclusions demonstrate that link deflection measurement based on strain gauges is not the most ideal method.

3.3.3 Applicability of strain gauges for link deflection measurements

It is important to highlight that strain gauges based link deflection measurements are *indirect* measurements. Strain gauges measure the strain of a certain fibre at a certain point of the beam. However, with a limited number of calculations the structural deflections of the beam can be determined from these local measurements. Actually the robot link, equipped with strain gauges, becomes a force sensor.

For this application, strain gauges are used within a small part of their measuring range; the relative variation of the electric resistance due to the applied force is very small. The strain should be measured at points of maximal strain to reduce all kinds of parasitic influences, such as influences of temperature. Following list summarizes the advantages and disadvantages of the use of strain gauges for deflection measurement:

Advantages

1. Strain gauges are well known and have been used effectively.
2. Strain gauges are relatively inexpensive.
3. Strain gauges have a very low mass; they change neither the load on the link, nor the dynamic properties of the link.
4. The range of the measuring system is high.
5. The bandwidth of the measuring system is high.

Disadvantages

1. They are sensitive to fatigue; however the fatigue limit is sufficiently high.
2. Due to overload strain gauges can be damaged.
3. Cross-influences due to other loads can be important.
4. The glueing of the strain gauges is very delicate; misalignment errors have a big influence on the accuracy of the system [69]. However, calibration could for the greater part solve this problem.
5. Industry is sceptical about the use of strain gauges in a manufacturing environment; they are fragile and difficult to install. Theoretically the strain gauges can be installed inside the robot arm, but practically this is very difficult and the to be measured strains decrease.

3.4 Optical link deflection measurements

In this section, a laser diode optical system is investigated for the real-time measurement of all spatial structural deflections of a flexible

link, except for the elongation of the link. Neglecting the elongation causes only a second order error. Different optical transducers and light sources are compared to determine which optical transducer and which light source should be used in the link deflection measurement system. Based on the results of this comparison, a measurement setup is defined and the equations which define the relation between the structural deflections of the link and the optical transducers measurements are determined. Finally, an accuracy analysis which has been carried out on this optical measurement system is discussed and the requirements for a practical optical measurement system are established.

3.4.1 Optical transducers and their light sources

When a light spot hits the sensitive area of the considered optical displacement transducer, an electric charge proportional to the light energy is generated at the incident position. This electric charge creates a photocurrent on the basis of which the position of the light spot on the transducer can be determined. For the link deflection measurement problem only two-dimensional optical transducers are considered:

- Quadrant Detector;
- Charge Coupled Device (CCD);
- Position Sensing Detector (PSD).

To get good results from the transducers, the type of light source is important. The light sources have to comply the following requirements:

- their wavelength should be appropriate to the used transducer;
- they should generate at the appropriate distance a small and stable light spot, according to the requirements of the transducer;
- to use them on a robot arm their dimensions should be as small as possible.

For this application HeNe lasers and semiconductor lasers seem to be the most suitable light sources.

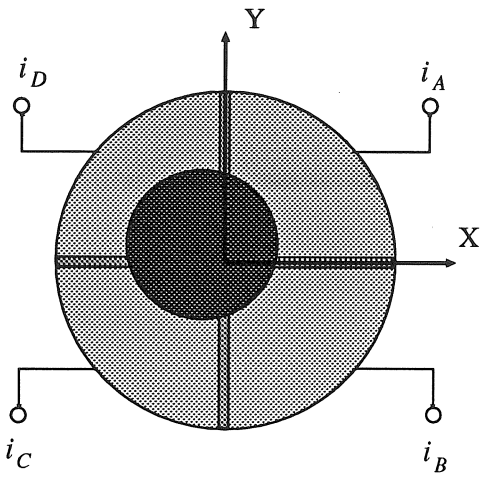

Figure 3.6: Quadrant detector.

3.4.1.1 Optical transducers

3.4.1.1.1 Quadrant detector

A quadrant detector is an analog optical transducer which consists of four separate but identical photodiodes integrated on a single circular silicon slice. The four photodiodes are electrically insulated from each other by a metallurgical separation (figure 3.6) [70].
Each quadrant generates a photocurrent proportional to the amount of light energy which incidents on the quadrant. If a light spot of known intensity distribution and of sufficient size to give an output from each quadrant hits the active surface of the detector then its position in a $\{X, Y\}$-frame is proportional to the difference of the quadrant outputs:

$$x \propto i_x = \frac{(i_A+i_B)-(i_C+i_D)}{i_A+i_B+i_C+i_D}$$

$$y \propto i_y = \frac{(i_A+i_D)-(i_B+i_C)}{i_A+i_B+i_C+i_D}.$$

Usually, a laser beam has a circular or elliptical cross section and a Gaussian intensity profile. This results in a non-linear change of the outputs as the laser beam moves. For that reason, quadrant detectors are mostly used as null-point devices. In such a situation, a radially symmetrical light spot is used and the detector is moved until the

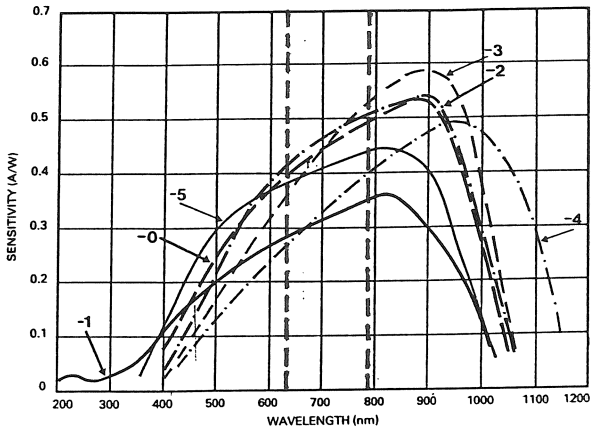

Figure 3.7: Spectral responses of quadrant detectors. The dashed vertical lines indicate the spectral lines of a red HeNe laser ($632.8nm$) and of a PHILIPS semiconductor laser ($790nm$).

output from each quadrant is equal; these tasks do not require the detector output to be highly linear.

In order to produce any two-dimensional measuring effect, the light spot must be of sufficient size to give an output from each quadrant. Greater signal sensitivity can be produced by using spot sizes close to the minimum level, but an extended measuring range can be obtained using a larger spot. The finite area of the quadrant detector dictates the optimum light spot size which determines the size of the measuring region in the field of view. YUANHAI [71] presents an algorithm to determine this optimum light spot size. Usually the laser beam needs to be expanded to reach this optimum light spot size. This expansion increases the cost of the measuring system, as well as the dimensions.

Quadrant detectors are commercially available within a wide range of spectral responses which makes HeNe lasers or semiconductor lasers very appropriate light sources. Figure 3.7 shows the spectral response of some CENTRONIC quadrant detectors [70]. The suffixes -0, -1, -2, -3, -4, -5 specify the spectral response of different quadrant detectors which have been optimized for a specific wavelength. The dashed vertical lines indicate the spectral lines of a red HeNe laser ($632.8nm$) and of a PHILIPS semiconductor laser ($790nm$) [81].

The major advantages of quadrant detectors are their low price and fast response. The disadvantages are their non-linear behaviour

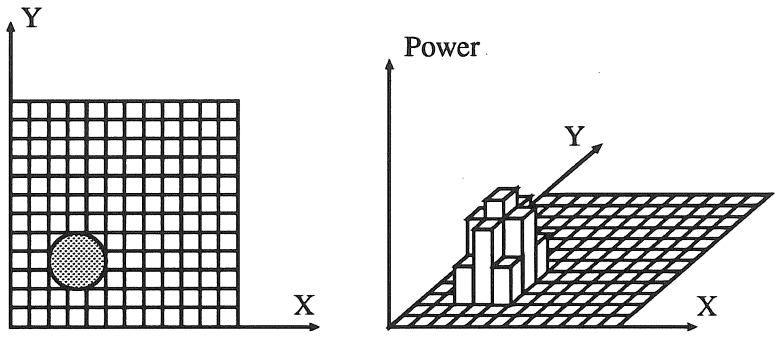

Figure 3.8: Charge coupled device.

and the required light spot size.

PREVOST and PAVLIN [33] use quadrant detectors to build an optical skeleton which is able to measure the deformation of each part of the robot and the final error of the position of the end-effector wherever in space.

3.4.1.1.2 Charge coupled device (CCD)

A CCD is a metal-oxide-semiconductor (MOS) structure which can collect, store and transfer localized packets of electric charge, generated by the incident light. Processing of these localized packets of information yields an image of the profile of the incident light [72].

Figure 3.8 gives a schematic representation of the principle of a CCD. A CCD consists of a matrix of very small photodiodes which are positioned very close to each other. Typical values for the dimensions of a single photodiode are $12 \times 18 \mu m$. The different photodiodes are precisely positioned $30 \mu m$ horizontally and $18 \mu m$ vertically from each other. For a CCD of $8.8 \times 11.4 mm$ this gives vertically 488 and horizontally 380 photodiodes, or in all 185440 photodiodes. Each of these photodiodes generates a photocurrent proportional to the amount of incident light energy.

CCD's are sensitive to light with a wavelength varying between $400 - 700 nm$, which makes most types of semiconductor lasers not very appropriate light sources. One of the biggest disadvantages of a CCD is its slow response. The access time for one photodiode is $50 ns$,

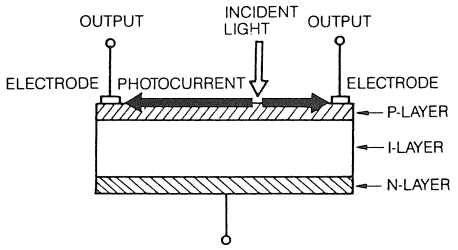

Figure 3.9: PSD sectional view.

which results in a global access time for the whole CCD of $\pm 10ms$. This is very slow compared the other optical displacement transducers. Moreover, this time should be increased with the time necessary for the processing of all the information, and this processing can be very complex. Besides, CCD's are expensive.

Because of this slow response and complex processing, CCD's are not the appropriate sensors for the intended application. CCD's are mostly used in commercial video cameras and in much industrial and scientific light sensitive and video recording equipment.

MULDERS ET AL. [31] use a CCD to measure the position of the free end of a robot arm. The biggest disadvantage of their measurement system is that the detection of the position of the laser beam in the matrix of pixels is too time-consuming, about $20ms$.

3.4.1.1.3 Position sensing detector (PSD)

A PSD is an optoelectronic sensor that provides two analog outputs representing x and y position information. The PSD senses the centre of a light spot on its sensitive area, and provides the continuous analog outputs as the light spot traverses this area.

As shown in figure 3.9 the PSD consists of three layers: P-layer, N-layer underneath, and I-layer in-between, all placed over a planar silicon substrate. Incident light falling on the PSD is converted photoelectrically and detected by the two electrodes on P-layer (P- and N-layers for duo-lateral types) as photocurrent [73].
When a light spot hits the PSD, an electric charge proportional to the light energy is generated at the incident position. This electric charge is driven through the resistive P-layer and collected by the electrodes. Since the resistivity of the P-layer is uniform, the photocurrent col-

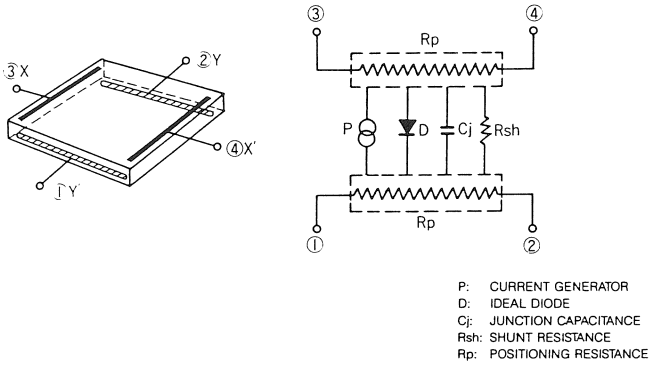

a. Structure b. Equivalent circuit

Figure 3.10: Duo-lateral type.

lected by an electrode is inversely proportional to the distance between the incident position and the electrode.

The two-dimensional PSD is classified by structure into two types: duo-lateral type and tetra-lateral type.

Duo-lateral type

As shown in figure 3.10.a, the duo-lateral type has electrodes on both surfaces (upper surface and under surface) of a photodiode. As shown in the equivalent circuit in figure 3.10.b, each position signal (photocurrent) is only divided into two parts by two resistive layers, and therefore, this type has a high position detecting ability (smaller position detection error and higher resolution).

Tetra-lateral type

As shown in figure 3.11.a, this type has four electrodes on the upper surface of a photodiode. Photocurrent is divided into four parts by the same resistive layer and output as a position signal (see figure 3.11.b). As compared with the duo-lateral type, this type has a distortion that is greater at the circumference. However, it features a bias that can be applied easier, a dark current that is smaller, and a response time that is faster.

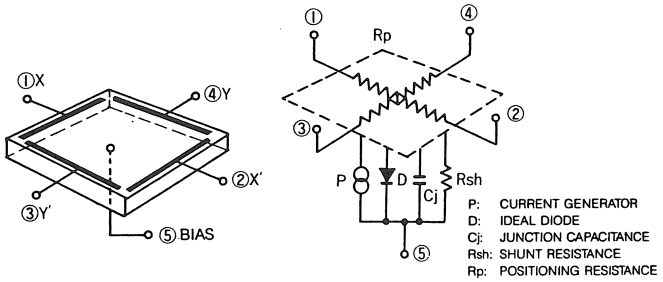

a. Structure b. Equivalent circuit

Figure 3.11: Tetra-lateral type.

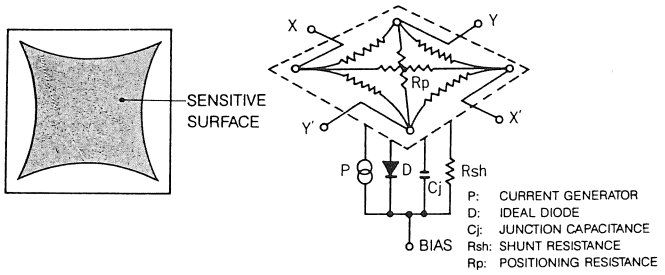

a. Structure b. Equivalent circuit

Figure 3.12: Pin-cushion type.

Pin-cushion type (improved tetra-lateral type)

This is the improved tetra-lateral type, with the improved sensitive surface and electrodes (figure 3.12). In addition to small dark current, fast response and easy bias application, which are advantages of the tetra-lateral type, distortion in the circumference has been greatly reduced. Figure 3.13 shows the distortions patterns of the different types of PSD's.

The position of the light spot on the PSD can be found by expressions 3.20 and 3.21, where X_1, X_2, and Y_1, Y_2 represent the output signals (photocurrent) of each electrode, and x, y are the co-ordinate positions of the centre of the intensity distribution of the light spot.

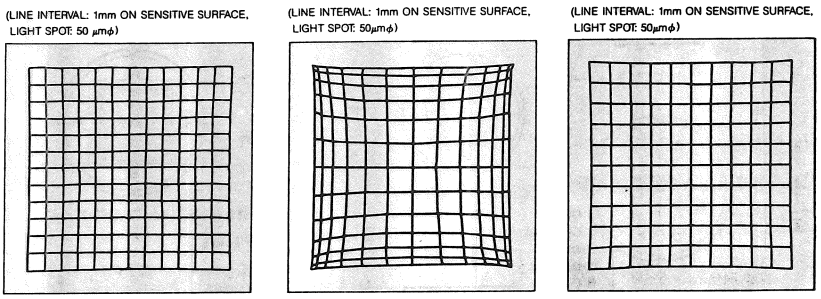

Figure 3.13: Distortion patterns of different types of PSD's.

Square type PSD

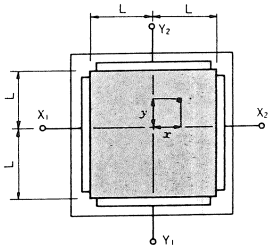

$$\frac{X_2-X_1}{X_1+X_2} = \frac{x}{L}$$
$$\frac{Y_2-Y_1}{Y_1+Y_2} = \frac{y}{L} \qquad (3.20)$$

Pin-cushion type PSD

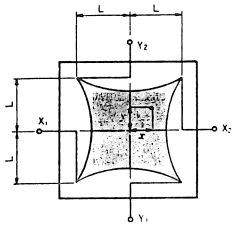

$$\frac{(X_2+Y_1)-(X_1+Y_2)}{X_1+X_2+Y_1+Y_2} = \frac{x}{L} \qquad (3.21)$$
$$\frac{(X_2+Y_2)-(X_1+Y_1)}{X_1+X_2+Y_1+Y_2} = \frac{y}{L}$$

PSD's are commercially available within a wide range of spectral response sensitivities which makes HeNe lasers or semiconductor lasers very appropriate light sources. Figure 3.14 shows the spectral response of two types of PSD's [73]. The dashed vertical lines indicate the spectral lines of a red HeNe laser ($632.8nm$) and of a PHILIPS semiconductor laser ($790nm$) [81]. The biggest advantages of PSD's are their high position resolution (up to $1\mu m$), highly linear behaviour or small position detection error ($< 1\%$), fast response speed, simple operating

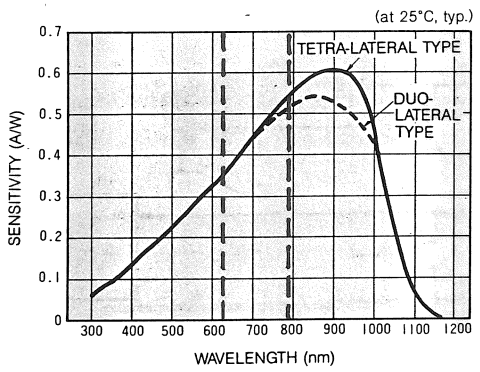

Figure 3.14: Spectral response of a PSD. The dashed vertical lines indicate the spectral lines of a red HeNe laser ($632.8nm$) and of a PHILIPS semiconductor laser ($790nm$).

circuits, independence of light spot focus, simultaneous measurement of light intensity and position, and the possibility to use modulation [73, 83].

However, to permit a reasonable displacement range for a given PSD the light spot size should be kept as small as possible. The displacement range, $\pm d_{max}$, is defined by:

$$d_{max} = \frac{r_{lin}.l_{PSD}}{2} - r_{ls} \tag{3.22}$$

where : $r_{lin}.l_{PSD}$: true effective length of PSD;
r_{lin} : linear portion sensitive area of PSD (0–1);
l_{PSD} : length sensitive area of PSD;
r_{ls} : radius of the light spot.

The decrease of the light spot size is restricted by a lower limit, since by decreasing the light spot size the incident power per square millimetre increases quadratically. The incident power per square millimetre is limited to prevent saturation of the sensor. A reduction of the total power in the beam, for instance by means of an optical filter, allows to decrease the light spot size further.

CANNON and SCHMITZ [21] use a linear fast acting silicon photodetector to measure the position of the tip of a flexible link. The photodetector is mounted, behind a focusing lens, $1m$ above the light bulb which is attached to the tip of the flexible link. UCHIYAMA and

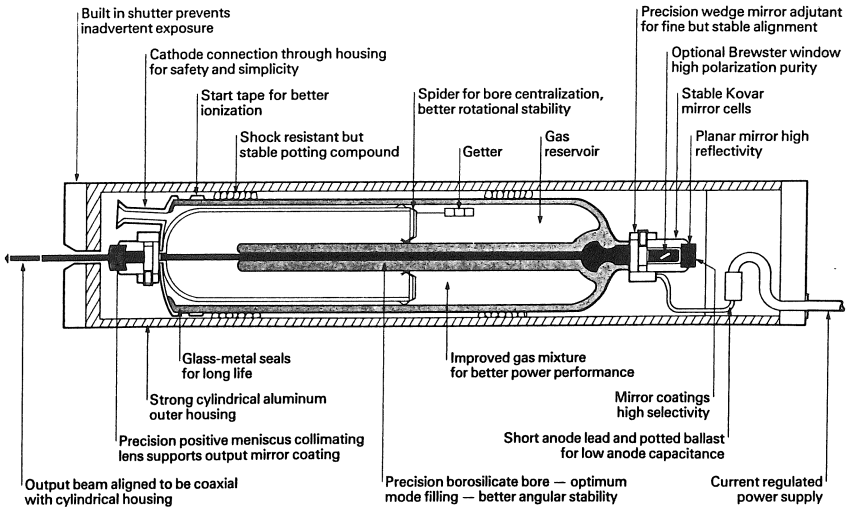

Figure 3.15: Cross-sectional view of a HeNe laser.

KONNO [32] use three PSD's mounted on one end of a robot link, and three semiconductor lasers mounted on the other end of the link, to measure the *spatial* structural deflections of a flexible link of a robot. The deflections which are measured are those at the tip of the link.

3.4.1.2 Light sources

Some specific terms related to laser theory are explained in appendix F.

3.4.1.2.1 HeNe laser

The most obvious light source is the HeNe laser. It generates at a sufficiently long distance a small and stable light spot.

Figure 3.15 shows the cross-sectional view of a HeNe laser head showing the details of the plasma tube [74].

The red HeNe laser is the most frequently used laser in industrial applications. Its characteristics are: [74]

- a collimated, coherent beam of red radiation at $632.8nm$;
- a beam diameter $2w_0$ varying between 0.59–$1.02mm$;
- a beam divergence 2θ varying between 0.79–$1.35mrad$ (equation F.3).

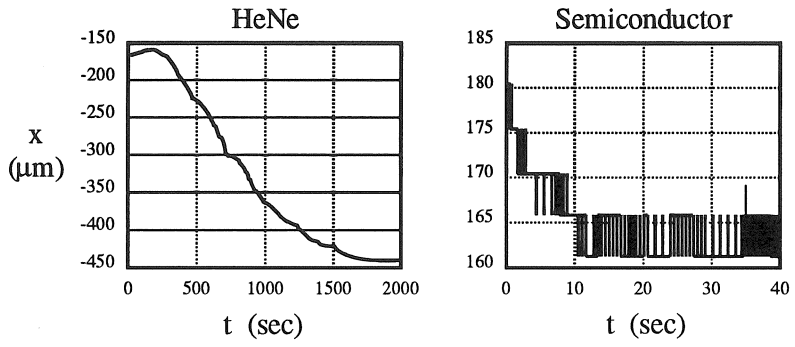

Figure 3.16: Thermal drift of a laser beam.

with w_0 the radius of the $1/e^2$ irradiance contour of the laser beam at the plane where the wave front is flat, and θ the angular radius of the cone which asymptotically approaches the $1/e^2$ irradiance contour (cf. figure F.3). Over a distance of $1m$, the diameter of the laser beam varies between $1.29mm$ and $1.49mm$ (equation F.1). As mentioned above, PSD's work independent of light spot size, but to permit a reasonable displacement range for a given PSD the light spot size should be kept as small as possible. So, the laser beam needs to be focused.

A HeNe laser is, due to several reasons, unsuitable as light source for the optical measurement system. First, its dimensions are too big to be built in in a robot arm. A common HeNe laser is $200mm$ to $300mm$ long, and has a diameter of about $30mm$. Secondly, if the laser beam need to be focused the necessary focusing optics increase strongly the dimensions of the HeNe laser system. Third, the unequal warming up of the cavity causes an angular drift of the mirrors, and of the laser beam. Figure 3.16 shows the values measured by the x-output of a PSD for a HeNe laser, and for a semiconductor laser, which have been started up cold at the moment t=0. The HeNe laser beam stabilizes only after half an hour.

For this application, atmospheric influences, as mentioned by KOEBNER [75], are negligible. They only become important in open air and at long distances.

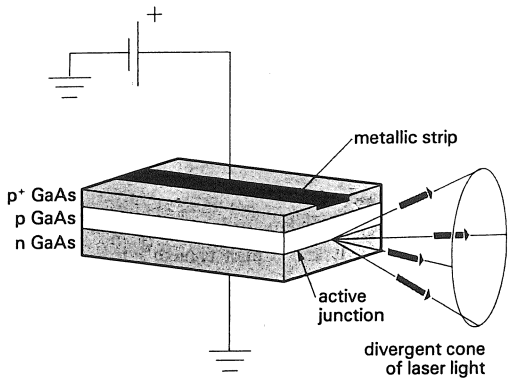

Figure 3.17: Structure of a simple gallium arsenide semiconductor laser.

3.4.1.2.2 Semiconductor laser

Semiconductor lasers, also called laser diodes, have all the general advantages and convenience of semiconductor and solid-state devices. They are compact, efficient, cost effective, suited for mass production, and in many ways superior to their non-solid-state counterparts. They present a good alternative for HeNe lasers.

Figure 3.17 shows the structure of simple gallium arsenide semiconductor laser. This is currently the most common type of semiconductor laser, and can be prepared so as to emit anywhere in the $700 - 850nm$ wavelength region. The active region of a semiconductor laser junction is not only small, but is also quite asymmetric. Typically, the junction of a gallium arsenide semiconductor laser has an effective thickness of only 0.1 micron, but the active region may be five micron wide. This leads to a very small and asymmetric beam waist, which is the place where the wave front is flat. Consequently, the beam divergence is severe and also asymmetric. Half-angle beam divergence in the direction perpendicular to the active layer (junction) is typically between 12 and 30 degrees. Divergence in the plane parallel to the layer is a factor of two to six times less than this.
Failure to correct the ellipticity of the beam is sometimes unimportant, but if the beam is to be collimated or focused for a particular application, the far-field laser beam will be different in the two directions. Usually, this asymmetric behaviour of the laser beam can be corrected by expanding the minor axis of the output.

The characteristics of a semiconductor laser are:

- a beam diameter $2w_0$ varying between 2–8mm;
- a beam divergence 2θ varying between 0.2–0.6$mrad$, dependent on the wavelength of the emitted light.

Again, the light spot size is too big and the laser beam needs to be focused.

The semiconductor laser is the ideal type of light source to be used in the the optical measurement system. First, a semiconductor laser is very compact. There exist semiconductor lasers which are 17mm long, and have an outside diameter of 8mm. This includes all circularization optics and focusing optics. This makes a semiconductor laser extremely appropriate to build in in a robot arm. Secondly, a semiconductor laser is cheap. Third, semiconductor lasers exist with a wide power range: from 0.5mW to 100mW. Fourth, the semiconductor laser beam stabilizes already after 20 seconds (figure 3.16). Since they are small solid-state devices, semiconductor lasers respond extremely fast to changes in driving current. If necessary, the output of a semiconductor laser can therefore be modulated at very rapid rates. One disadvantage of a semiconductor laser beam is its invisibility to the human eye. Semiconductor lasers with an output wavelength of 670nm are already available but they are much more expensive. However, this visibility is not necessary for the working of the optical link deflection measurement system. It is only useful to the alignment of the measurement system. The infrared laser beam can be visualized temporarily by using an infrared phosphor screen [76]. When the excited phosphor is irradiated by infrared energy in the range 700 to 1300nm, it emits visible energy. This visible emission is orange-coloured.

3.4.1.3 Conclusion

For the intended application, PSD's are the most appropriate from all the existing optical, two-dimensional transducers. Compared to the other transducers, the PSD features high position resolution, highly linear behaviour, fast response speed, simple operating circuits, independence of light spot focus and wide range of spectral response.

From the different light sources, semiconductor lasers are most

appropriate. Compared to the HeNe lasers, semiconductor lasers are very compact, including all circularization optics and focusing optics, have a longer expected lifetime (about 50.000 hours, with respect to 20.000 hours for a HeNe laser [74]) and so extremely appropriate to build in in a robot arm. Further, a semiconductor laser is cheaper, and the laser beam stabilizes instantaneous. The big disadvantage of the invisibility of the laser beam is not a significant disadvantage for the optical deflection measurement system.

3.4.2 Measurement setup

This section describes the measurement setup to measure the structural deflections d_x, d_y, a_x, a_y and a_z of a flexible link. The previous section has shown that position sensing detectors (PSD's) in combination with semiconductor lasers are the most appropriate devices to build the link deflection measurement system.

Figure 3.18 shows the optical link deflection measurement system. The elongation of the link, d_z, cannot be measured. Since d_z is usually very small compared to the other deflections, neglecting d_z causes only second order errors. The system consists of three semiconductor laser systems mounted at one end of the link and three two-dimensional PSD's, one mounted in the focal plane of a lens, at the other end. Since the laser beams follow a straight line independent of the deflections of the link, the positions of the spots of the semiconductor lasers on the PSD's contain all information regarding the structural deflections of the link. The semiconductor laser beams are the reference for the link deflection measurements.

The problem of determining five structural deflections out of six co-ordinates can be divided into two subproblems. The structural deflections d_x, d_y and a_z are calculated by combining the measurements of the *PSD's used without a lens.* The influence of the structural deflections a_x and a_y on these measurements should first be eliminated. The structural deflections a_x and a_y are calculated out of the measurements of the *PSD mounted in the focal plane of a lens.* As this PSD is mounted in the focal plane of the lens, the structural deflections d_x and d_y do not affect the position of the laser spot on this PSD (figure 3.19). The influence of the structural torsion, a_z, can be avoided if the structural deflections a_x and a_y are defined with respect to the *rotated* link frame.

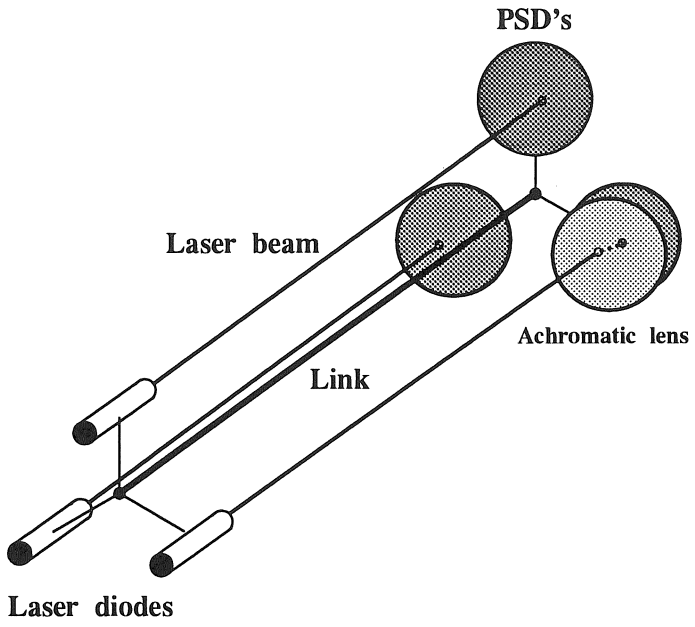

Figure 3.18: Schematic representation of the optical link deflection sensor system.

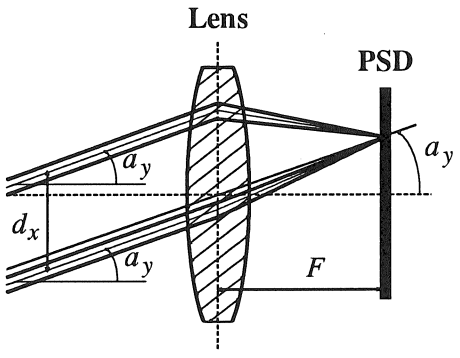

Figure 3.19: PSD in focal plane of lens only measuring angular deformations.

3.4.3 Relation between optical transducers measurements and structural deflections of a flexible link

This section investigates the relation between the structural deflections of a flexible link and the co-ordinates of the laser spots on the PSD's which form part of the optical link deflection measurement system proposed in the previous section. Within the equations describing this relation, system parameters appear beside the co-ordinates measured by the PSD's. Some calibration methods are proposed to determine those system parameters.

3.4.3.1 Equations describing relation between structural deflections and laser spot co-ordinates

To determine the equations describing the relation between the structural deflections of a flexible link and the co-ordinates of the laser spots on the PSD's, homogeneous transforms are used and four co-ordinate frames are introduced: a reference co-ordinate frame, a sensor co-ordinate frame, a corrected sensor co-ordinate frame and a measuring co-ordinate frame. Homogeneous transforms are defined in appendix B, the four co-ordinate frames are defined in subsequent section. Further assume that the PSD's used without a lens get the subscript 1 and 2, and the PSD equipped with a lens get the subscript 3.

3.4.3.1.1 Co-ordinate frames for deflection measurement

To derive the relation between the structural deflections and the co-ordinates of the laser spots on the PSD's, four co-ordinate frames are used: the reference co-ordinate frame, the sensor co-ordinate frame, the corrected sensor co-ordinate frame and the measuring co-ordinate frame. The reference co-ordinate frame is attached to the straight link and is unique. The sensor, the corrected sensor and the measuring co-ordinate frame are attached to the PSD and exist for each PSD.

Before deflection, the Z-axis of all these co-ordinate frames is parallel to the longitudinal axis of the straight link. The X-axis, the Y-axis and the origin of these co-ordinate frames are located in the plane described by the three PSD's at the tip of the link. This plane is perpendicular to the longitudinal axis of the straight link. Figure 3.20

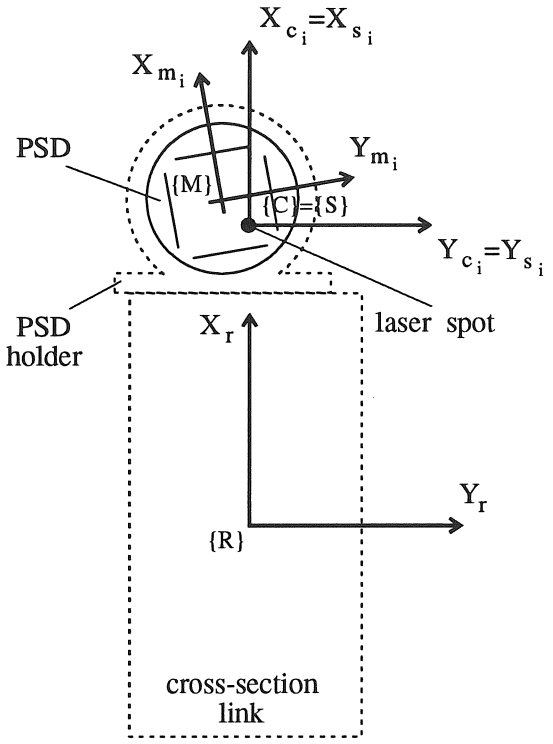

Figure 3.20: Co-ordinate frames for deflection measurement.

illustrates the definitions of the co-ordinate frames before deflection. Figure 3.21 illustrates the difference between the sensor and the corrected sensor co-ordinate frame. Before deflection, both co-ordinate frames coincide. Due to the structural deflections a_x and a_y, the sensor co-ordinate frame moves away from the corrected sensor co-ordinate frame.

Reference co-ordinate frame $\{X_r, Y_r, Z_r\} = \{\mathbf{R}\}$

Its origin coincides with the centre of the straight link, its Z-axis is parallel to the longitudinal axis of the straight link, its X-axis is determined by calibration, and its Y-axis is formed by the right hand rule to complete the frame (figure 3.20). The structural deflections d_x, d_y and a_z are defined with respect to this frame.

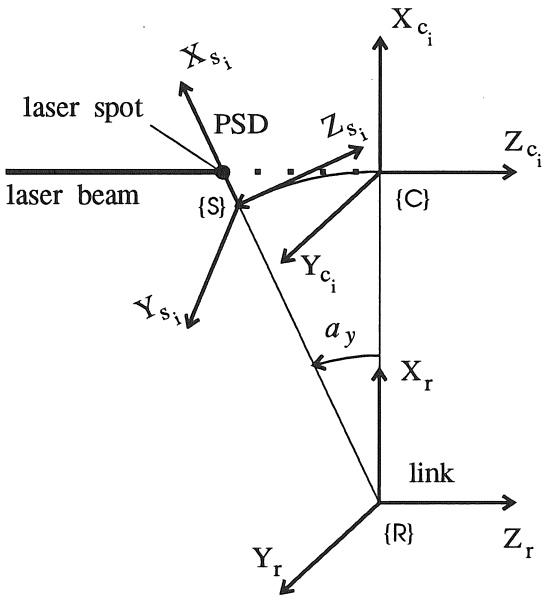

Figure 3.21: Difference between the sensor and the corrected sensor co-ordinate frame.

Sensor co-ordinate frame $\{X_{s_i}, Y_{s_i}, Z_{s_i}\} = \{\mathrm{S}\}$

Before deflection, the axes of this co-ordinate frame are parallel to the axes of the reference co-ordinate frame, and its origin coincides with the point where the laser beam falls on the PSD (figure 3.20 and 3.21). This co-ordinate frame is fixed to the PSD.

Measuring co-ordinate frame $\{X_{m_i}, Y_{m_i}, Z_{m_i}\} = \{\mathrm{M}\}$

Its origin coincides with the electrical zero of the PSD, its X- and Y-axis correspond to the co-ordinate axis of the PSD, and its Z-axis is perpendicular to the transducer surface (figure 3.20). The co-ordinates of the laser spot on the PSD are defined with respect to this frame.

Corrected sensor co-ordinate frame $\{X_{c_i}, Y_{c_i}, Z_{c_i}\} = \{\mathrm{C}\}$

This co-ordinate frame is the transformed sensor co-ordinate frame. The transformation is defined by the structural deflections a_x and a_y. Its XY-plane coincides with the XY-plane of the reference co-ordinate frame. Its Z-axis remains parallel to the longitudinal axis of the straight link (figure 3.20 and 3.21). This co-ordinate frame is only needed for the PSD's without a lens.

3.4.3.1.2 Structural deflections d_x, d_y, a_z

Suppose that the flexible link is submitted to the structural deflections d_x, d_y and a_z, and that initially the bending angles a_x and a_y are zero. In this case, the corrected sensor co-ordinate frame $\{X_{c_i}, Y_{c_i}, Z_{c_i}\}$ coincides with the sensor co-ordinate frame $\{X_{s_i}, Y_{s_i}, Z_{s_i}\}$. The problem of determining the equations can be regarded as a two-dimensional problem: the deflections take place in the plane perpendicular to the longitudinal axis of the link. Only the PSD's used without a lens are considered.

Figure 3.22 shows the geometrical relation between the link and the PSD's. The reference frame $\{X_r, Y_r\}$ represents the link, the corrected sensor frame $\{X_{c_i}, Y_{c_i}\}$ represents a PSD, for i=1,2. For an undeformed link, the origin of the corrected sensor frame coincides with the position of the laser spot on the PSD. This origin is situated at a distance S_i to the origin of the reference frame. From the same figure follows the definition of the structural angle α_i which is measured positively clockwise.

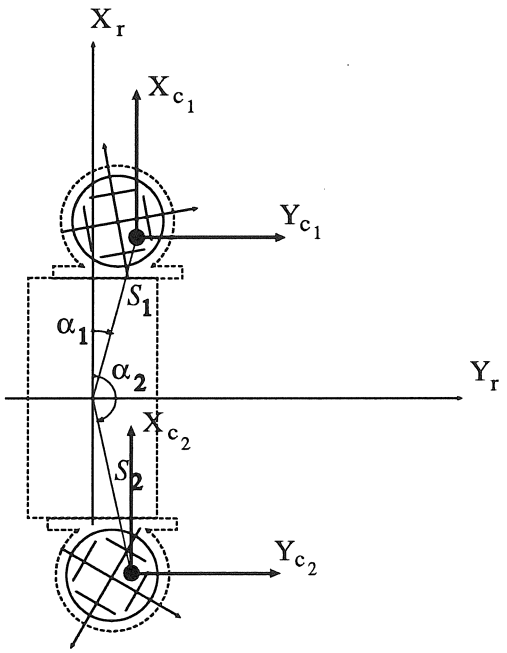

Figure 3.22: Geometrical relation between the link and the PSD's.

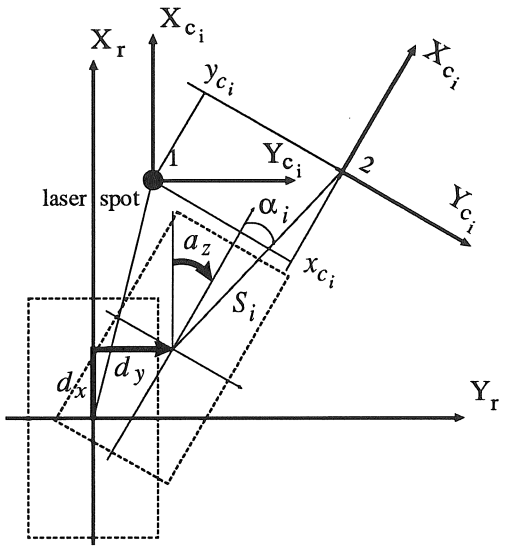

Figure 3.23: Geometrical relation between the measured transducer co-ordinates and the structural deflections d_x, d_y and a_z.

Due to the structural deflections d_x, d_y and a_z, the corrected sensor frame moves from position 1 to position 2. On the other hand, the laser beam remains in the very same place with respect to the reference frame but moves relative with respect to the corrected sensor frame (figure 3.23). The co-ordinates of the laser spot in the new corrected sensor frame are determined by making use of the homogeneous transforms between the different co-ordinate frames. Appendix G.2 describes in detail the derivation of the equations.
The co-ordinates of the laser spot x_{c_i} and y_{c_i} are given by:

$$\begin{aligned} x_{c_i} &= -S_i c_i - c_z(d_x - S_i c_i) - s_z(d_y - S_i s_i) \\ y_{c_i} &= -S_i s_i + s_z(d_x - S_i c_i) - c_z(d_y - S_i s_i), \end{aligned} \tag{3.23}$$

where : $c_i = \cos\alpha_i$, $s_i = \sin\alpha_i$;
$c_z = \cos a_z$, $s_z = \sin a_z$.

Combining the measurements of the two PSD's used without a lens (i=1,2) gives four co-ordinates: (x_{c_1}, y_{c_1}) and (x_{c_2}, y_{c_2}). Solving the four equations 3.23 for the four unknowns d_x, d_y, s_z and c_z yields the

structural deflections d_x, d_y and a_z. Appendix G.3 describes in detail the derivation of the equations.
The unknowns s_z and c_z are given by:

$$\begin{aligned} s_z &= [(S_2s_2 - S_1s_1)(x_{c_2} + S_2c_2 - x_{c_1} - S_1c_1) \\ &\quad - (S_2c_2 - S_1c_1)(y_{c_2} + S_2s_2 - y_{c_1} - S_1s_1)]/\Delta; \qquad (3.24) \\ c_z &= [(S_2c_2 - S_1c_1)(x_{c_2} + S_2c_2 - x_{c_1} - S_1c_1) \\ &\quad + (S_2s_2 - S_1s_1)(y_{c_2} + S_2s_2 - y_{c_1} - S_1s_1)]/\Delta; \qquad (3.25) \\ \Delta &= (y_{c_2} + S_2s_2 - y_{c_1} - S_1s_1)^2 + (x_{c_2} + S_2c_2 - x_{c_1} - S_1c_1)^2. \\ & \qquad (3.26) \end{aligned}$$

The structural deflections d_x, d_y and a_z are given by, for i=1,2:

$$\begin{aligned} d_x &= S_ic_i - c_z(x_{c_i} + S_ic_i) + s_z(y_{c_i} + S_is_i); \qquad (3.27) \\ d_y &= S_is_i - s_z(x_{c_i} + S_ic_i) - c_z(y_{c_i} + S_is_i); \qquad (3.28) \\ a_z &= \arctan\frac{s_z}{c_z}. \qquad (3.29) \end{aligned}$$

3.4.3.1.3 Bending angles a_x, a_y

Suppose that the flexible link is submitted to the structural deflections a_x and a_y too. The reference co-ordinate frame is translated along its X- and Y-axis over the distance d_x, respectively d_y, and is rotated about the Z-axis over an angle a_z. With respect to this new, rotated co-ordinate frame $\{X_r', Y_r', Z_r'\}$ the bending angles a_x and a_y are defined. In this case, the co-ordinates of the laser spot on the PSD, which is mounted in the focal plane of a lens, only depend on the structural deflections a_x and a_y. For this PSD, i=3, the corrected sensor frame is not needed.

Figure 3.24 shows the relation between the structural deflections a_x and a_y, and the position of the laser spot on the PSD which is mounted in the focal plane of a lens. The cross-influence of a_x on a_y, and vice versa, is neglected. This assumption is reasonable since the deflections of the links of a flexible robot are usually small. The co-ordinates of the laser spot in the sensor frame are given by

$$\begin{aligned} x_{s_3} &= -L\tan a_y \qquad (3.30) \\ y_{s_3} &= L\tan a_x \qquad (3.31) \end{aligned}$$

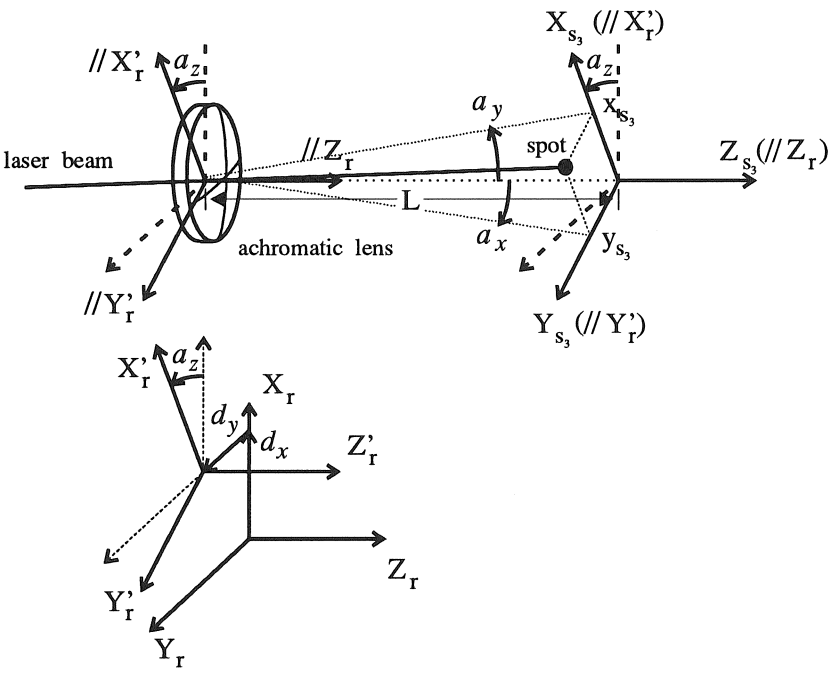

Figure 3.24: Relation between the structural bendings and the position of the laser spot on the PSD mounted in the focal plane of a lens.

where L is the distance between the lens and the PSD. Appendix G.4 gives the complete derivation of these equations and establishes the structural requirements of the lens-sensor system: these equations are only valid if:

- the laser beam is nearly parallel to the Z-axis of the reference frame ($\alpha \ll 1$),
- before deflection the optical axis of the lens is nearly parallel to the Z-axis of the reference frame ($\beta \ll 1$),
- L equals the focal length of the lens F;

with α the angle between the laser beam and the Z-axis of the reference frame, and β the angle between the optical axis of the lens and the Z-axis of the sensor frame, which is before deflection parallel to the Z-axis of the reference frame, as defined in section G.4.

The structural deflections a_x and a_y are calculated from equation 3.31, respectively equation 3.30, and are defined with respect to the *rotated* reference frame by following equations:

$$a_x = \arctan \frac{y_{s_3}}{F} \tag{3.32}$$

$$a_y = \arctan \frac{-x_{s_3}}{F}. \tag{3.33}$$

If a_x and a_y are small the equations become simplified:

$$a_x = \frac{y_{s_3}}{F} \tag{3.34}$$

$$a_y = \frac{-x_{s_3}}{F}. \tag{3.35}$$

3.4.3.1.4 Correction of d_x, d_y, a_z

For a general deflection of the flexible link, with the bending angles a_x and a_y different from zero, the corrected sensor co-ordinate frames $\{X_{c_i}, Y_{c_i}, Z_{c_i}\}$ of the PSD's used without a lens (i=1,2) do not coincide with the sensor co-ordinate frame $\{X_{s_i}, Y_{s_i}, Z_{s_i}\}$. The equations to calculate the structural deflections d_x, d_y and a_z are based on the co-ordinates defined in the corrected sensor frame. However, the co-ordinates of the laser spot on the PSD are measured in the sensor frame.

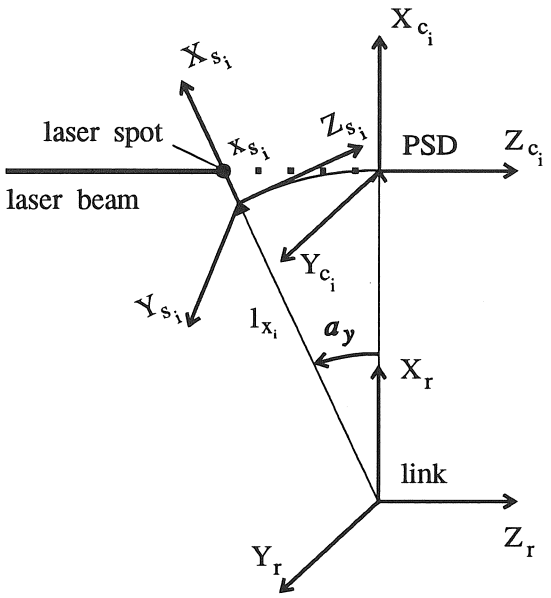

Figure 3.25: Influence of the bending angle a_y on the co-ordinates of the laser spot.

Figure 3.25 shows the influence of the structural deflection a_y on the co-ordinate x_{c_i}. The relation between the corrected co-ordinate x_{c_i} and the sensor co-ordinate x_{s_i} is given by:

$$x_{c_i} = (x_{s_i} + l_{x_i})c_y - l_{x_i}; \tag{3.36}$$

the corrected co-ordinate y_{c_i} is calculated in a similar way:

$$y_{c_i} = (y_{s_i} + l_{y_i})c_x - l_{y_i}. \tag{3.37}$$

The distances l_{x_i} and l_{y_i} are defined by

$$l_{x_i} = S_i\,|c_i| \tag{3.38}$$
$$l_{y_i} = S_i\,|s_i|, \tag{3.39}$$

where $|\bullet|$ means the absolute value of $\bullet$.

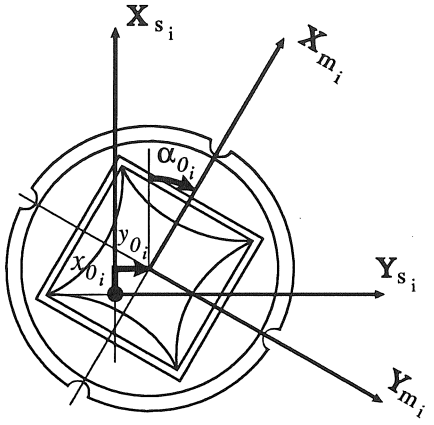

Figure 3.26: Geometrical relation between the measuring frame and the sensor frame.

3.4.3.1.5 From measuring co-ordinate frame to sensor co-ordinate frame

In reality, the measuring frame of the PSD does not always coincide with the assumed sensor frame. The structural deflections are calculated from the sensor frame co-ordinates whereas the co-ordinates of the laser spot on the PSD are measured in the measuring frame. This applies to all PSD's (i=1–3).

Figure 3.26 shows the geometrical relation between the measuring frame and the sensor frame. The homogeneous transform ${}^{s_i}\mathbf{A}_{m_i}$ transforms the co-ordinates measured in the measuring frame to their corresponding co-ordinates in the sensor frame.

$$\begin{bmatrix} x_{s_i} \\ y_{s_i} \\ 1 \end{bmatrix} = \underbrace{\begin{bmatrix} \cos\alpha_{0_i} & -\sin\alpha_{0_i} & x_{0_i} \\ \sin\alpha_{0_i} & \cos\alpha_{0_i} & y_{0_i} \\ 0 & 0 & 1 \end{bmatrix}}_{{}^{s_i}\mathbf{A}_{m_i}} \begin{bmatrix} x_{m_i} \\ y_{m_i} \\ 1 \end{bmatrix} \tag{3.40}$$

where x_{0_i} and y_{0_i} are the co-ordinates in the sensor frame of the origin

of the measuring frame. The definition of the structural angle α_{0_i} follows from figure 3.26; α_{0_i} is measured positively clockwise.

The co-ordinates in the measuring frame are derived from the voltages measured by the PSD. The conversion of those measured voltages to the corresponding co-ordinates is done by the sensitivity factors G_{x_i} and G_{y_i} of the PSD. The unit of those sensitivity factors is $\frac{m}{V}$.

$$x_{m_i}(m) = G_{x_i}.x_{psd_i}(V) \quad (3.41)$$

$$y_{m_i}(m) = G_{y_i}.y_{psd_i}(V) \quad (3.42)$$

3.4.3.2 Calculation of the structural deflections

The calculation of the structural deflections d_x, d_y, a_x, a_y and a_z consists of five steps that are executed consecutively:

1. measurement of the co-ordinates of the laser spot on the PSD in the measuring frame with conversion of the units from V to m, for i=1–3 (equations 3.41 and 3.42);

2. transformation of the co-ordinates in the measuring frame to their corresponding co-ordinates in the sensor frame, for i=1–3 (equation 3.40);

3. calculation of the bending angles a_x and a_y (equations 3.32 and 3.33);

4. transformation of the co-ordinates in the sensor frame to their corresponding co-ordinates in the corrected sensor frame, for i=1,2 (equations 3.36 and 3.37);

5. calculation of the structural deflections d_x, d_y and a_z (equations 3.26, 3.27, 3.28 and 3.29).

3.4.3.3 Calibration of the measurement setup

Within the previous equations, which describe the relation between the structural deflections of a flexible link and the co-ordinates of the laser spots on the PSD's, some system parameters appear beside the co-ordinates measured by the PSD's. Those system parameters are:

1. the sensitivity factors G_{x_i} and G_{y_i}, which transform the voltages measured by the PSD to the corresponding co-ordinates in the measuring frame, for i=1–3;

2. the rotation angle α_{0_i} and the co-ordinates (x_{0_i}, y_{0_i}) from the homogeneous transform ${}^{s_i}\mathbf{A}_{m_i}$ which transforms the co-ordinates measured in the measuring frame to their corresponding co-ordinates in the sensor frame, for i=1–3;

3. the structural distance S_i, between the origin of the reference frame and the origin of the corrected sensor frame, and the angle α_i, which this distance vector makes with respect to the X-axis of the reference frame, for i=1,2;

4. the distance F, between the lens and the PSD, for i=3.

To be able to calculate the structural deflections, the system parameters should first be calibrated. An on-line method, developed within this thesis, to calibrate the system parameters S_i and α_i, α_{0_i}, and F is proposed in [51, 67, 77]. The big disadvantage of this method is that it requires an extensive measuring equipment. In this section, a method to calibrate those system parameters off-line is proposed. This method is most suited for industrial implementation of the optical link deflection measurement system, and most of the calibrations can be carried out by the manufacturer of the optical measurement system. The calibration of the sensitivity factors G_{x_i} and G_{y_i}, and of the co-ordinates of the origin of the measuring frame x_{0_i} and y_{0_i} is discussed in a separate section. This calibration is the same for the on-line method as for the off-line method.

3.4.3.3.1 Calibration of the sensitivity factors and of the co-ordinates of the origin of the measuring frame

The sensitivity factors G_{x_i} and G_{y_i} are calibrated by measuring the voltages generated by the PSD as a function of the displacement of the laser beam. This is done for both axes of the PSD. Figure 3.27 shows such sensitivity characteristics; the sensitivity factors are about $0.1\frac{mm}{V}$. The sensitivity factors G_{x_i} and G_{y_i} are found as the reciprocal of the slope of the linear part of the sensitivity curve. The linear part of this curve determines also the measuring range of the PSD: in the

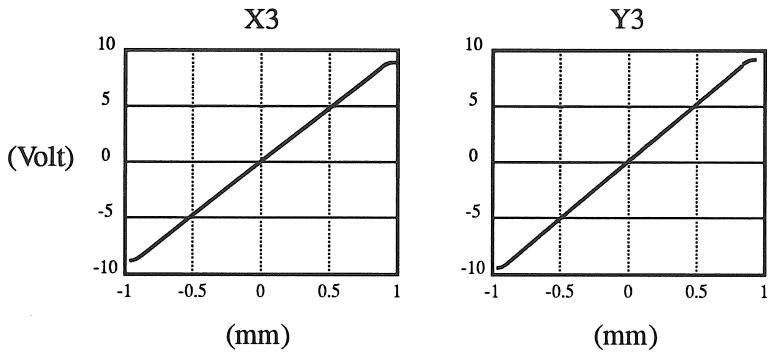

Figure 3.27: Sensitivity characteristics of the PSD, and its electronics, mounted in the focal plane of a lens.

above figure the measuring range is about $\pm 0.8mm$. This calibration is done off-line.

The co-ordinates in the sensor frame of the origin of the measuring frame, x_{0_i} and y_{0_i}, are automatically calibrated by the measurement system. The position where the laser spot falls on the PSD depends on the mounting of the PSD, the mounting of the laser and the deflection of the flexible link. To calibrate those system parameters, the robot should be brought in a reference position where no deflections occurs: then the measurement of the co-ordinates of the laser spot on the PSD determines the origin of the sensor frame with respect to the measuring frame. In this case, solving equation 3.40 for the co-ordinates x_{0_i} and y_{0_i} yields:

$$\begin{bmatrix} x_{0_i} \\ y_{0_i} \end{bmatrix} = \begin{bmatrix} -\cos\alpha_{0_i} & \sin\alpha_{0_i} \\ -\sin\alpha_{0_i} & -\cos\alpha_{0_i} \end{bmatrix} \begin{bmatrix} xs_{m_i} \\ ys_{m_i} \end{bmatrix} \tag{3.43}$$

where xs_{m_i} and ys_{m_i} are the co-ordinates in the measuring frame of the laser spot on the PSD before deflection, or of the origin of the sensor frame. The calibration of these system parameters requires that the orientation angle α_{0_i} is known.
If nevertheless some deflections occur in the reference position, all further determined structural deflections are defined relative with respect to those initial deflections.

3.4.3.3.2 Off-line calibration of the system parameters S_i, α_i and α_{0_i}, and F

For the off-line calibration of the system parameters, the calibration procedure is subdivided into a separate calibration of the components of the optical link deflection measurement system, and a calibration of the components mounted on the flexible link. For the focal distance F, a separate calibration is always necessary. This method exhibits clearly advantages with respect to the on-line method.

The combined calibration of the system parameters S_i, α_i, x_{0_i}, y_{0_i} and α_{0_i} consists of four steps. If however the measurement system could be integrated into the design of the link, only step 4 is necessary.

Step 1 determines the position of the PSD within its holder frame. The PSD is mounted, by the manufacturer of the measurement system, within a holder. This PSD holder is characterized by a co-ordinate frame attached to a specific point of the holder. This frame is called the holder frame $\{X_h, Y_h, Z_h\} = \{\mathrm{H}\}$. The relation between the measuring frame of the PSD and its holder frame is described by the homogeneous transform ${}^{h_i}\mathbf{A}_{m_i}$:

$$ {}^{h_i}\mathbf{A}_{m_i} = \begin{bmatrix} \cos\alpha_{m0_i} & -\sin\alpha_{m0_i} & x_{m0_i} \\ \sin\alpha_{m0_i} & \cos\alpha_{m0_i} & y_{m0_i} \\ 0 & 0 & 1 \end{bmatrix}. \qquad (3.44) $$

Figure 3.28 shows the geometrical relation between the two frames. The calibration of x_{0m_i}, y_{0m_i} and α_{0m_i} is carried out off-line, by the manufacturer of the measurement system. For the PSD mounted in the focal plane of a lens, only α_{0m_i} should be calibrated.

Step 2 determines within the measurement setup the position of the holder frame of the PSD's with respect to the reference frame of the link (figure 3.28). The relation between these two frames is described by the homogeneous transform ${}^{r_i}\mathbf{A}_{h_i}$:

$$ {}^{r_i}\mathbf{A}_{h_i} = \begin{bmatrix} \cos\alpha_{h0_i} & -\sin\alpha_{h0_i} & x_{h0_i} \\ \sin\alpha_{h0_i} & \cos\alpha_{h0_i} & y_{h0_i} \\ 0 & 0 & 1 \end{bmatrix}. \qquad (3.45) $$

The parameters x_{0h_i}, y_{0h_i} and α_{0h_i} are derived from the construction

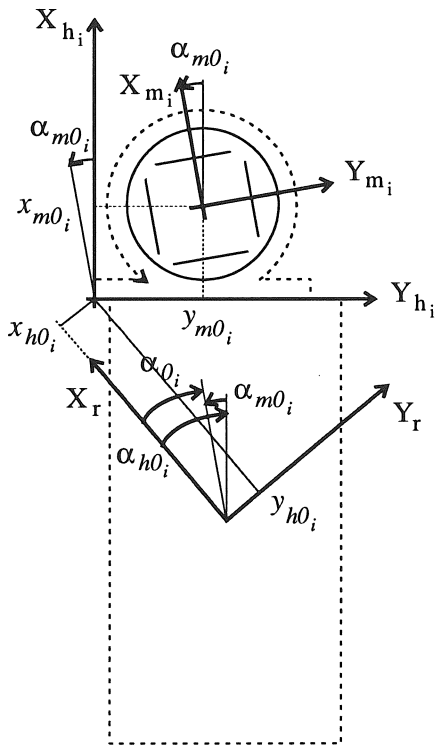

Figure 3.28: Geometrical relation between the measuring frame of the PSD, the holder frame attached to the PSD holder and the reference frame of the link.

drawings of the link. For the PSD mounted in the focal plane of a lens, only α_{0h_i} should be calibrated.

Step 3 combines the results from step 1 and 2 to transform the co-ordinates measured in the measuring frame of the PSD to their corresponding co-ordinates in the reference frame of the link. This is only necessary for the PSD's used without a lens.

$$\begin{bmatrix} x_{r_i} \\ y_{r_i} \\ 1 \end{bmatrix} = \underbrace{{}^{r_i}\mathbf{A}_{h_i}\,{}^{h_i}\mathbf{A}_{m_i}}_{{}^{r_i}\mathbf{A}_{m_i}} \begin{bmatrix} x_{m_i} \\ y_{m_i} \\ 1 \end{bmatrix}. \tag{3.46}$$

In this step, also the system parameter α_{0_i} is calibrated (figure 3.28), for i=1–3:

$$\alpha_{0_i} = \alpha_{m0_i} + \alpha_{h0_i}. \tag{3.47}$$

From step 3, all calculations are done on-line and automatically by the software which belong to the measurement system.

Step 4 is called the zero point calibration. The system parameters S_i and α_i are, by definition, derived from the position of the origin of the corrected sensor frame within the reference frame before deflection. Before deflection, the corrected sensor frame coincides with the sensor frame, so the origin of the corrected sensor frame coincides with the laser spot on the PSD. Now, section 3.4.3.3.1 determines the co-ordinates in the measuring frame of the laser spot on the PSD, (xs_{m_i},ys_{m_i}), while step 3 determines the transformation from the measuring frame to the reference frame. So, the co-ordinates in the reference frame of the origin of the corrected sensor frame, (xc_{r_i},yc_{r_i}), are given by:

$$\begin{bmatrix} xc_{r_i} \\ yc_{r_i} \\ 1 \end{bmatrix} = {}^{r_i}\mathbf{A}_{m_i} \begin{bmatrix} xs_{m_i} \\ ys_{m_i} \\ 1 \end{bmatrix}. \tag{3.48}$$

The system parameters S_i and α_i are derived from, for i=1,2:

$$S_i = \sqrt{{xc_{r_i}}^2 + {yc_{r_i}}^2} \tag{3.49}$$

$$\alpha_i = \arctan \frac{yc_{r_i}}{xc_{r_i}}. \tag{3.50}$$

Out of the measurements xs_{m_i} and ys_{m_i}, and the system parameter α_{0_i}, also the system parameters x_{0_i} and y_{0_i} are calculated, for i=1–3 (equation 3.43).

Usually, the system parameter F is given by the lens manufacturer. However, the value provided by the manufacturer is only determined within two percent of its nominal value. Appendix G.5 describes a method to calibrate F more accurately and to test if L=F.

3.4.4 Guidelines for the construction of an accurate optical link deflection measurement system

This section investigates the requirements to build an accurate optical link deflection measurement system. The construction of the measurement system consists of two phases: a design phase and a mounting- and calibration phase. The first subsection discusses the choice of the components of the measurement system. The second subsection establishes the guide-lines for mounting the measurement system.

3.4.4.1 Design of the optical link deflection measurement system

The design of the optical link deflection measurement system starts from following specifications:

- the dimensions of the link;
- the expected structural deflections of the link and the maximal tolerance on them;
- the circumstances in which the measurements take place;
- the sampling rate of the robot controller;
- the maximal cost price of the measurement system.

The expected structural deflections can be estimated from a compliance breakdown of the link (cf. section 2.2 and [78]). These specifications give rise to some criteria by which the parameters of the different components of the measurement system are tested:

- the resolution of the measurement system;

- the required accuracy of the calculated deflections;
- the combined measuring and calculation time of the deflections;
- the minimal and maximal dimensions of the components.

The resolution of the measurement system and the computation speed of the measurement system should be better than the values which are found for modern industrial robots: the resolution of the encoders used in industrial robots is about $2\mu rad$ [79], while the sampling rate of a modern robot controller varies from 200 to $1000Hz$.

3.4.4.1.1 Parameters which influence the choice of the components

Only those parameters are discussed which influence really the choice of the components. More general properties of the components have already been discussed in previous sections.

For the intended application, semiconductor lasers are the most appropriate light sources. The main parameters which determine the choice of *semiconductor laser* are:

- **power** P

  Semiconductor lasers exist with a power range from $0.5mW$ to $100mW$. The power of the semiconductor laser should be limited as the incident power per square millimetre on the optical transducer is limited to prevent saturation of the transducer. This incident power per square millimetre depends also on the size of the light spot on the transducer. The maximal power of the semiconductor laser is determined by:

$$\frac{P}{\pi w^2} < P_a, \tag{3.51}$$

  where w is the radius of the light spot, and P_a is the allowed incident power per square millimetre. A reduction of the total power in the beam is possible by means of an optical filter.

- **output wavelength** λ

  Only semiconductor lasers with an output wavelength below $900nm$ should be considered (see figure 3.14).

- **focal distance F_d**

  Semiconductor lasers have an output beam diameter varying between 2–8mm, and a beam divergence varying between 0.2–0.6mrad, dependent on the wavelength of the emitted light. So, the light spot size is too big and the laser beam needs to be focused. The minimal diameter of the laser beam is $2w_0$ [80]:

$$2w_0 = \frac{4\lambda F_d}{\pi D}, \tag{3.52}$$

  where D is the diameter of the output beam. Contrary to collimated semiconductor lasers, the focal distance of the focused semiconductor laser need to be adapted to the length of the link to get the minimal light spot on the PSD. So, for each new application, a different semiconductor laser is needed. However, it is possible to cover a wide range of lengths of a link with a limited number of semiconductor lasers. If the diameter of the light spot is assumed to remain smaller than $1mm$ for the range of lengths from 400 to $1000mm$, only two different semiconductor lasers are necessary: one with a focal distance of $500mm$, covering the range 400 to $600mm$, and one with a focal distance of $800mm$, covering the range 600 to $1000mm$ [81].

To measure the position of the light spot, two-dimensional optical transducers are used. From the different existing two-dimensional optical transducers, PSD's are the most appropriate. The main parameters which determine the choice of *PSD* are:

- **linearity lin_{psd}**

  Besides the linearity of a PSD, lin_{psd}, also the ratio of the linear part of the sensitive area of the PSD to the total sensitive area is very important. This ratio is represented by the parameter r_{lin}, which varies from 0 to 1.

- **effective sensitive area** $l_{psd} \times l_{psd}$

A PSD measures the centre of the incident laser beam on the its surface. The area which is needed to keep the laser spot entirely on the PSD is the minimal effective sensitive area of the PSD. This area is a function of the deflection range of the link, the radius of the light spot and the linear part of the sensitive area of the PSD. For the PSD's used without a lens, solving equation 3.22 for the detector length, l_{psd}, yields

$$l_{psd} = \frac{2\,d_{max} + 2\,w_0}{r_{lin}}, \tag{3.53}$$

where $\pm d_{max}$ is the displacement range of the link. For the PSD mounted in the focal plane of a lens, l_{psd} is calculated as follows:

$$l_{psd} = \frac{2\,F\,a_{max} + 2\,w_0}{r_{lin}}, \tag{3.54}$$

where $\pm a_{max}$ is the range of the bending angles of the link, and F is the focal length of the lens. The size of the necessary effective sensitive area determines largely the price of the PSD.

- **true effective range** rd_{psd}, ra_{psd}

The true effective range of the PSD is the linear part of the PSD which can be used to measure the structural deflections. Previous equations show that the detector length l_{psd} not really indicates the true effective range of the PSD. The influence of the linearity of the PSD can be very important. The true effective range, rd_{psd}, is calculated as follows:

$$rd_{psd} = \pm\frac{r_{lin}\,l_{psd}}{2}. \tag{3.55}$$

For the PSD mounted in the focal plane of a lens, also an angular true effective range can be defined. This angular true effective range, ra_{psd}, is calculated as follows:

$$ra_{psd} = \pm\frac{r_{lin}\,l_{psd}}{2\,F}. \tag{3.56}$$

- **position resolution** PSD_{res}

One of the criteria by which the parameters of the different components of the measurement system are tested is their resolution. The resolution should be better than the resolution of the encoders which are used in modern industrial robots. For the PSD's used without a lens the resolution is not so critical. Particularly for the PSD of the lens-PSD system, its resolution is very important. The necessary resolution is calculated as follows:

$$a_{res} = \frac{PSD_{res}}{F} \quad < enc_{res}, \tag{3.57}$$

where a_{res} is the resolution of the bending angles and enc_{res} is the resolution of the encoders used in the robot.

The optical link deflection measurement system uses a lens in combination with a PSD to measure pure bending angles. The main parameters which determine the choice of *lens* are:

- **focal length** F

In order that the angular resolution of the measurement system should be as small as possible, the focal length of the lens should be as big as possible (equation 3.57).

- **lens diameter** ϕ

The expected area described by the laser beam determines the lens diameter. The effective area of a lens for laser beams which deviate from the optical axis of the lens up to 4° is limited to 60% of its global area. Beams which incident outside this effective area are deformed. The lens diameter is calculated as follows:

$$\phi > \frac{2\,d_{max} + w_l}{0.6}, \tag{3.58}$$

where w_l is the diameter of the light spot on the lens.

- **price**

For this optical measurement system, precision laser-grade optimized achromatic lenses are recommended. They are more expensive than other achromatic lenses but they have been designed with an optimization criterion adapted to laser light. Also, they are manufactured to tighter tolerances and better surface quality.

A last component which should be considered is the A/D converter. The main parameters which determine the choice of *A/D converter* are:

- **number of bits n**

  There is no point to choose the resolution of the A/D converter much higher than the resolution of the transducers. The resolution of a A/D converter is determined by its number of bits. The necessary number of bits is calculated as follows:

$$A/D_{res} = \frac{l_{psd}}{2^n - 1} \quad < \quad PSD_{res}, \tag{3.59}$$

  where A/D_{res} is the resolution of the A/D converter. Thermal drift, due to induced thermocouple voltages at the input of the A/D converter limits the attainable resolution of the A/D converter. This problem becomes critical for A/D converters with a word length of 16 bits [82].

- **conversion time A/D_t**

  The conversion by an A/D converter results in a time delay between the analog and the digital signal due to the required conversion time. The measurement of the structural deflections requires six PSD measurements. If these measurements are read in sequentially, the global time delay between the first and the last measurement can cause some errors. Therefore, the use of one A/D converter for each measurement can prevent these problems. The conversion by the A/D converter is the limiting factor for the bandwidth of the measurement system.

3.4.4.1.2 Choice of the components

Previous paragraphs discuss the main parameters of the components of the measurement system and the main design criteria which the choice of the different components should meet. Figure 3.29 and figure 3.30 show schematically the algorithms to choose the different components on the base of these design criteria.

Figure 3.29 shows the algorithm to choose the components to measure the structural deflections d_x, d_y and a_z. The measurement setup to measure these structural deflections requires two focused semicon-

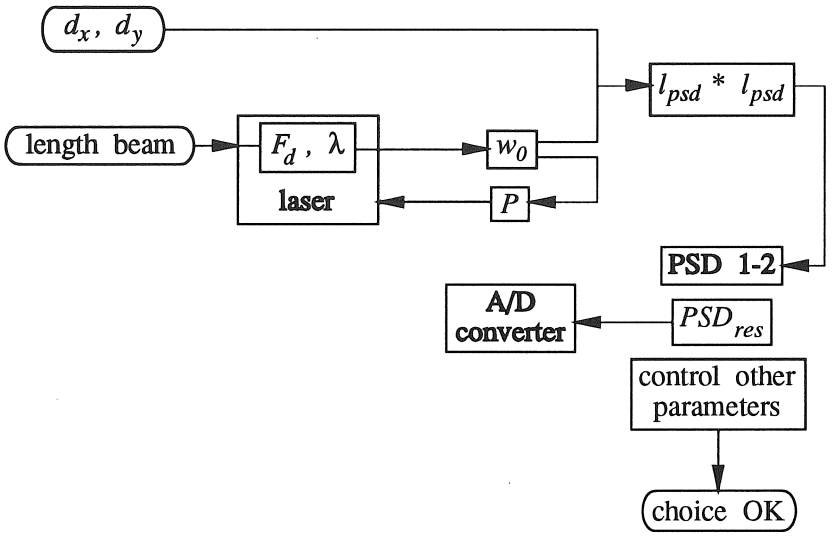

Figure 3.29: Algorithm to choose the components to measure the structural deflections d_x, d_y and a_z.

ductor lasers, two PSD's, a multiplexer and an A/D converter. The choice of the components starts from the length of the link and the expected structural deflections of the link.

Figure 3.30 shows the algorithm to choose the components to measure the structural deflections a_x and a_y. For these structural deflections, the measurement setup consists of a focused semiconductor laser, a PSD, an achromatic lens and an A/D converter. The choice of the components starts from the length of the link, the expected structural deflections of the link and the desired angular resolution of the measurement system. The PSD should be mounted in the focal plane of the lens to filter out the influence of the structural deflections d_x and d_y. Due to the combination of a focused laser beam with an achromatic lens, the minimal cross-section of the laser beam occurs not on the PSD but somewhere between the lens and the PSD. The place where the minimal cross-section occurs and the real cross-section of the light spot on the PSD are derived in appendix G.6.

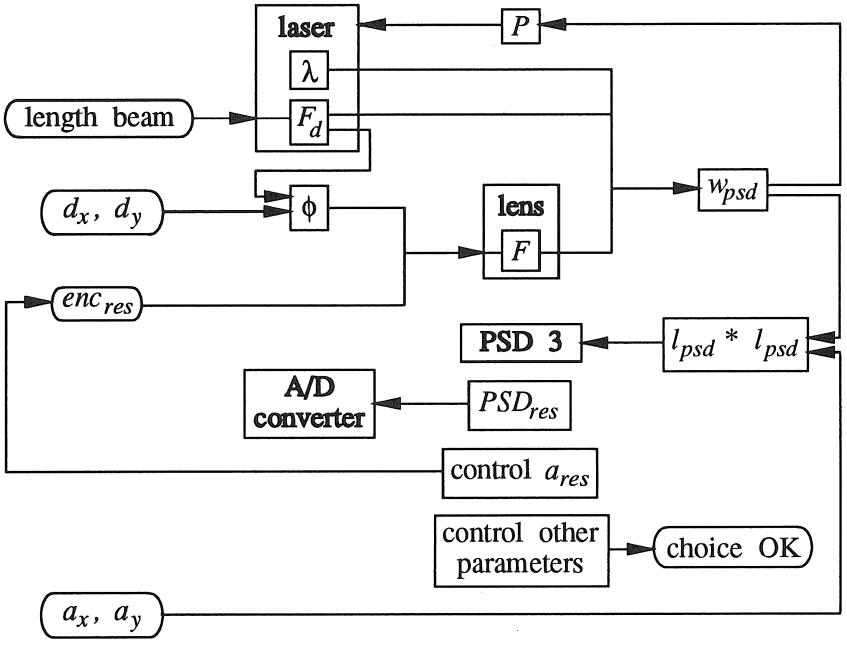

Figure 3.30: Algorithm to choose the components to measure the structural deflections a_x and a_y.

3.4.4.2 Mounting the optical link deflection measurement system

Structural guide-lines for mounting the optical link deflection measurement system, which minimize the errors on the measured structural deflections, can be derived from an accuracy analysis carried out on the equations derived in section 3.4.3. Such an accuracy analysis has been carried out in [77]. The outcome of this research is given hereafter.

Those guide-lines are:

1. The angle α_1, at which the first sensor is located with respect to the reference frame, does not influence the error on the structural deflections.

2. The second sensor is located optimally at 180° with respect to the first sensor: $\alpha_2 = \alpha_1 + 180°$.

3. The angle α_3, at which the lens-sensor system for the measurement of the bending angles is located with respect to the reference frame, is arbitrary.

4. The structural distances S_1 and S_2, between the sensors and the reference frame, are optimally equal to each other and as large as possible.

5. The focal length F of the lens, of the lens-sensor system, is optimally as large as possible.

6. The mounting distance L, between the lens and the sensor, is very critical and is optimally equal to the focal length F of the lens.

7. Special attention should be paid to the zero point calibration and to the stability of the laser beam.

3.4.4.3 Summary of the conditions for an error free measurement

Figure 3.31 gives a schematic overview of the global optical link deflection measurement system. The numbers in the figure refer to the undermentioned conditions for an error free measurement.

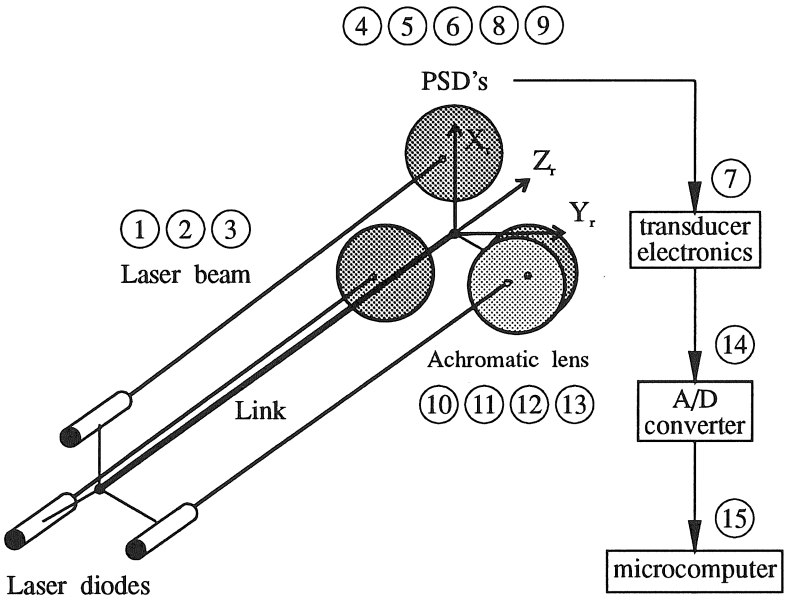

Figure 3.31: Overview of the optical link deflection measurement system.

To get an error free measurement, the optical link deflection measurement system should meet following conditions:

1. The laser beams exhibit a very low angular drift.
2. Atmospheric influences are negligible.
3. The laser beams are parallel to the Z-axis of the reference frame.
4. Ambient light does not influence the measurement.
5. The considered optical transducers are linear across their range.
6. The sensitivity factors of the considered optical transducers are accurately known.
7. The drift and the noise of the analog evaluation electronic circuits of the considered optical transducers should be very small.
8. Before deflection, the considered optical transducers are mounted perpendicular to the Z-axis of the reference frame: the laser beams incident perpendicular to the displacement transducers.
9. The considered optical transducers are mounted in a way that a maximum of the effective sensitive area of the transducer is used during the measurements.
10. The lens is properly aligned: before deflection, the optical axis of the lens is parallel to the Z-axis of the reference frame, and coincides with the longitudinal axis of the third laser beam.
11. The lens is a thin (achromatic) lens.
12. The optical transducer which measures the bending angles is mounted in the focal plane of the lens.
13. The A/D conversion introduces no quantization error and minimal time delays between the different measurements.
14. No significant rounding errors are introduced by the calculations.
15. The calibration yields exact parameters.

The equations to calculate the structural deflections have been derived for a measurement system which meets these conditions.

3.5 Alternative link deflection measurement methods

This section discusses two alternative methods to build a link deflection measurement system. Both methods are derived from the above proposed method. The first method combines the optical measurements with a strain gauge measurement, which saves one optical transducer. The second method uses three lens-PSD systems to build a measurement system which can measure larger structural deflections. This section only gives a brief description of the alternative systems. The advantages and disadvantages of these alternative systems can largely be derived from previous sections.

3.5.1 Combined strain gauges based and optical link deflection measurement

Section 3.3 discussed a method to determine the structural deflections of a robot link by means of strain gauges. A link deflection measurement system based on strain gauges has been built and tested, but it appears to suffer from a lot of disadvantages, making this method not quite advisable to measure structural deflections. However, if only the torsion angle a_z of the link should be measured, some of these disadvantages disappear, and the use of strain gauges to measure just the structural deflection becomes feasible. This measurement system requires only one set of strain gauges.

For the optical link deflection measurement method, two two-dimensional optical transducers are needed to measure the two structural displacements d_x and d_y, and the torsion angle a_z of the link. If however the torsion angle of the link could be derived from another measurement, the two structural displacements can be derived from the measurements of one two-dimensional optical transducer.

The combination of optical measurements for the other structural deflections of the link with a strain gauge based measurement of the torsion angle of the link can save one two-dimensional optical transducer, which reduces certainly the price of the global measurement system and also the computation time of all structural deflections.

3.5.2 Adapted optical link deflection measurement

Section G.4 mentioned already the possibility to build a measurement system which can measure larger structural deflections using three lens-PSD systems. One lens-PSD system, with the PSD mounted in the focal plane of the lens: $L{=}F$, is used to measure the bending angles, while the other lens-PSD systems are used to measure the remaining structural deflections. For these two lens-PSD systems, the PSD is mounted between the lens and the focal plane of the lens: $L{<}F$. In this case, the measurable deflection range is not only determined by the measuring range of the PSD's but also by the value of L, and F. However, the calculations of the structural deflections become much more complex because the value of the measured co-ordinate is not only function of the bending angles a_x or a_y but also of the displacements d_x and d_y. Also the construction of this measurement system becomes much more complex.

Figure 3.32 gives an example of a lens-PSD system with $L{<}F$. The PSD mounted at a distance L of the lens is represented by the co-ordinate frame $\{X_s, Z_s\}$, while the co-ordinate frame $\{X'_s, Z'_s\}$ represents the PSD mounted at a distance F of the lens. The figure shows that for a certain deformation (d_x, a_y) the co-ordinate measured by the first PSD, x_s, is smaller than the one measured by the second PSD, x'_s. With same size of PSD the lens-PSD system with $L{<}F$ realizes a larger measuring range. The value of L is determined by the desired measuring range and by the dimensions of the sensitive surface of the available PSD. The desired measuring range determines also the dimensions of the lens.

3.6 Experimental optical link deflection sensor

The purpose of the experimental optical link deflection sensor is to demonstrate the feasibility of this optical measurement system to determine in *real-time* the spatial structural deflections of a flexible link. This optical measurement system, including the corresponding software, is called **DIOMEDES**, which stands for "laser **DI**ode **O**ptical system for **ME**asuring structural **DE**flection**S**". In [52], this experimental optical link deflection sensor has been used to improve the

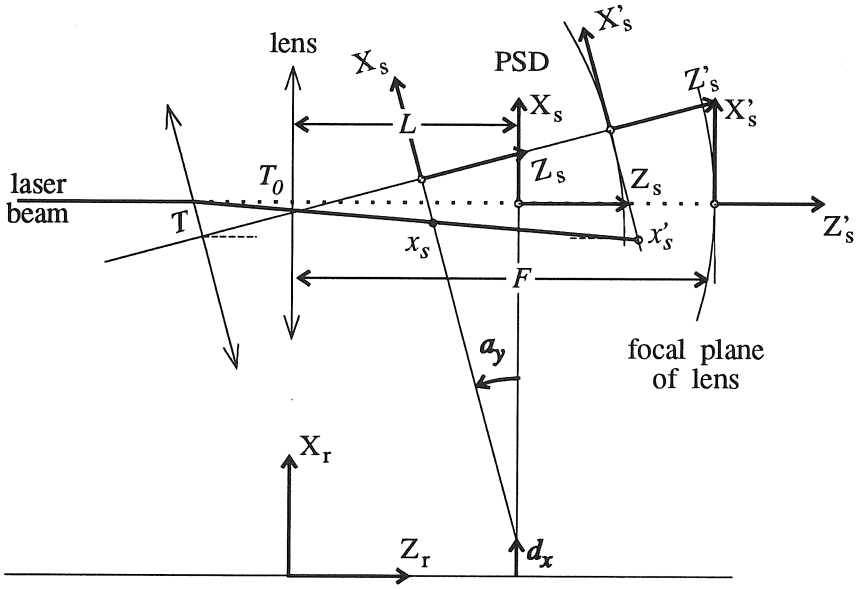

Figure 3.32: Adapted optical link deflection measurement system.

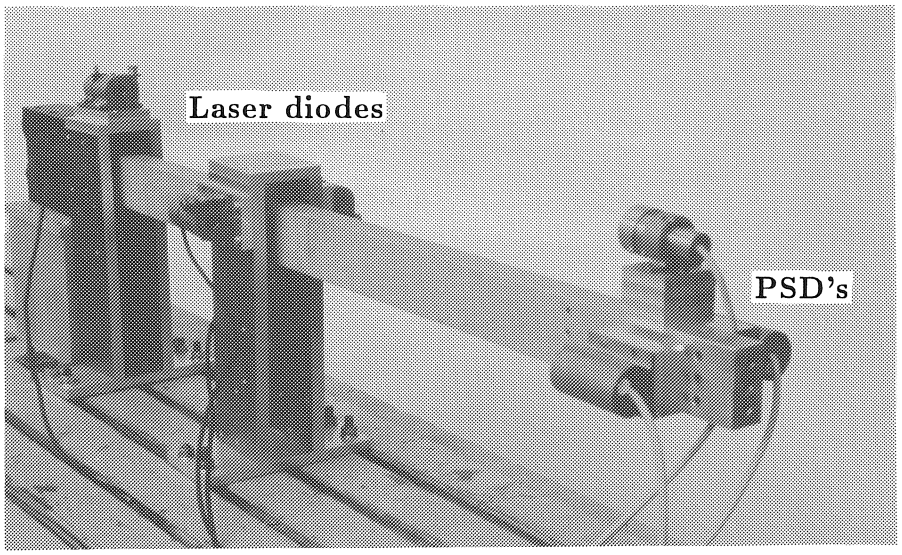

Figure 3.33: Experimental setup of **DIOMEDES**.

accuracy of the tracking control of a flexible one-link manipulator.

3.6.1 Experimental setup

Figure 3.33 shows the experimental setup of **DIOMEDES**. The link is a rectangular beam made of aluminium. Three semiconductor lasers are mounted at one end of the link. Three PSD's are mounted at the other end, among which one PSD is mounted in the focal plane of a lens. The construction drawings of the different components are given in [77].

3.6.1.1 The link

A simple clamped-free beam serves as a model for a flexible robot link. The beam is sufficiently flexible so deflections of several millime-

Flexible link	
characteristic	value
length of the projection	$800mm$
height	$49.6mm$
width	$24.8mm$
material	Al

Table 3.1: Characteristics of the flexible link.

Philips Small Size Collimator Pen CQL73		
characteristic	symbol	value
output power	P	$1mW$
output wavelength	λ	$790nm$
output beam diameter	D	$2mm$
focal distance	F_d	$500mm$ $(2\times)$
		$800mm$ $(1\times)$
length of laser		$17mm$
outside diameter		$8mm$

Table 3.2: Characteristics of semiconductor lasers.

tres can be realized. The characteristics of the beam are presented in table 3.1. The clamping of the beam is not infinitely stiff. By mounting the semiconductor lasers apart from the beam, the flexibility of the clamping is automatically included in the calculations of the structural deflections.

3.6.1.2 The semiconductor lasers

The semiconductor lasers are mounted apart from the beam, so the structural deflections measured by the optical measurement system can be compared with the measurements carried out by external displacements transducers. The characteristics of the three semiconductor lasers are presented in table 3.2 [81]. Each semiconductor laser is mounted in a holder. On the one hand, this holder can realize a fine adjustment of the laser beam, according to polar coordinates r and θ, so the spot of the laser beam on the PSD can be adjusted so that it coincides with the centre of the PSD, and the measurable deflection range becomes as large as possible. On the other hand, this holder

Hamamatsu PSD S1880		
characteristic	symbol	value
type		Pin-cushion
effective sensitive area	$l_{psd} \times l_{psd}$	$12 \times 12mm$
true effective range	r_{psd}	$\pm 5mm$
position resolution	PSD_{res}	$6\mu m$
linearity	lin_{psd}	A: 0.8–1.5%
		B: 1.5–2.5%

Table 3.3: Characteristics of PSD's used without a lens.

permits to align the laser beam to be parallel to the Z-axis of the reference frame.

3.6.1.3 The PSD's and the optics

The three PSD's are aligned in the same plane, perpendicular to the Z-axis of the reference frame. The two PSD's without a lens are identical, while the PSD which is mounted in the focal plane of a lens is much smaller and of a different type. The characteristics of the two PSD's used without a lens are presented in table 3.3 [73]. The linearity of these PSD's is defined within two circular zones A and B. Zone A has a radius of $2.5mm$, while zone B has a radius of $5mm$. These two PSD's are used to measure the two structural displacements d_x and d_y, and the torsion angle a_z, while the PSD mounted in the focal plane of the lens is used to measure the two bending angles a_x and a_y. The characteristics of this PSD are presented in table 3.4 [83]. The linearity of this PSD is valid within 80% of its effective sensitive area. Each semiconductor laser is mounted in a holder. Special attention deserves the manufacturing of the holder for the lens-PSD system as well as the mounting of the lens and the PSD into the holder. This should be done according to the conditions regarding the construction of the lens-PSD system, stated in section 3.4.4.3.

The characteristics of the lens, of the lens-PSD system, are presented in table 3.5 [74]. Calibrating the focal length of the lens, using the method described in appendix G.5, gave a value of $56.41mm$ which corresponds to the values given by the manufacturer.

Sitek PSD 2L2		
characteristic	symbol	value
type		Duo-lateral
effective sensitive area	$l_{psd} \times l_{psd}$	$2 \times 2mm$
true effective range	r_{psd}	$\pm 0.8mm$
angular true effective range	ra_{psd}	$\pm 14mrad = \pm 0.8°$
position resolution	PSD_{res}	$< 1\mu m$
linearity	lin_{psd}	$< 0.5\%$
allowed incident power density	P_a	$40\text{–}50 \frac{mW}{mm^2}$

Table 3.4: Characteristics of PSD mounted in focal plane of a lens.

Melles Griot Achromatic lens 01 LAO 068		
characteristic	symbol	value
lens diameter	ϕ	$19mm$
focal length	F	$56mm \pm 1\%$

Table 3.5: Characteristics of the lens.

3.6.1.4 The A/D converter

The co-ordinates are fed to the calculation algorithm in the micro-computer using a $12-bit$ Lab Master DMA board [84]. This Lab Master board can read up to 16 analog single ended signals, however this happens sequentially: it possesses only one A/D converter. The characteristics of this A/D converter are presented in table 3.6. The resolution of the A/D converter is defined in function of the length l_{psd} of the used PSD (equation 3.59). The time delay between the reading of the first voltage and the reading of the sixth voltage is $200\mu s$. For

$12-bit$ Lab Master DMA		
characteristic	symbol	value
number of bits	n	12
resolution	A/D_{res}	$2.93\mu m - 12mm$
		$0.49\mu m$ or $8\mu rad - 2mm$
conversion time	A/D_t	$30\mu s$

Table 3.6: Characteristics of the A/D converter.

			PSD 1 Hamamatsu	PSD 2 Hamamatsu	PSD 3 Sitek
Sensitivity factor	G_{x_i}	$\frac{mm}{V}$	0.6680	0.6760	0.1057
	G_{y_i}	$\frac{mm}{V}$	0.6749	0.6856	0.1054
PSD wrt {H}	x_{0m_i}	mm	16.0710	15.7900	
	y_{0m_i}	mm	20.8680	20.7500	
	α_{0m_i}	rad	1.5699	1.5577	-2.5200
Holder wrt {R}	x_{0h_i}	mm	-20.4700	20.6250	
	y_{0h_i}	mm	-32.0700	31.9750	
	α_{0h_i}	rad	-1.5700	1.5708	0.0000
PSD wrt {R}	α_{0_i}	rad	-0.0001	3.1285	-2.5200
Focal length lens	F	mm			56.4100

Table 3.7: Calibrated system parameters.

a sinusoidal signal at a frequency of $20Hz$, this time delay introduces already a phase shift of 1.44°. This explains the limited bandwidth of the measurement system. This problem becomes very important for the measurement of *dynamic* deformations of flexible links, especially when these deformations are used to control the motion of the flexible link.

3.6.1.5 The corresponding software

The software allows to calibrate the setup and to calculate, in real-time, the five structural deflections. The software implements the equations derived in the above described sections. On a PC-AT, operating at $8MHz$ and equipped with a floating point co-processor, it takes less than $5ms$ to measure the six co-ordinates and to calculate the five structural deflections. A graphical routine is available showing continuously the spatial deformation of the end of the flexible link. The corresponding software has been developed in Turbo Pascal 5.0 [77]

3.6.2 Calibration of system parameters

The description of the calibration procedures is given in section 3.4.3.3. The values of the calibrated system parameters are presented in table 3.7. Only those system parameters are mentioned which can be

determined by an off-line calibration. The remaining system parameters, x_{0_i} and y_{0_i}, and S_i and α_i, depend on the initial position of the laser spot on the PSD, and are automatically calibrated by the zero point calibration.

3.6.3 Accuracy of the deflection measurements

To test the accuracy of the optical measurement system, static deflections are imposed to the link, and are measured by the system. To verify these measurements, the applied static deflections are also measured by external transducers: the displacements are verified using dial gauges, while the rotations are verified using an autocollimator.

3.6.3.1 Structural deflections d_x, d_y and a_z

Figure 3.34 shows the deflection measurements of the structural deflections d_x, d_y and a_z. The accuracy of the measurements of d_x and d_y is 2%, and is rather stable over the entire range. This error can be mainly attributed to the noise on the electronics, which are used to amplify the PSD analog outputs. The accuracy of the measurements of a_z is about 10%, for large rotation angles. The accuracy analysis, carried out in [77], shows that the error on a_z is an order of magnitude larger than the error on d_x and d_y.

3.6.3.2 Bending angles a_x and a_y

Figure 3.35 shows the deflection measurements of the structural deflection a_x. As the structural deflection a_y is simultaneously measured by the same PSD, the conclusions for the structural deflection a_x are also valid for a_y. The accuracy of the measurements of the bending angles is worse for small angles than for large angles. This can be mainly attributed to the noise on the electronics, which are used to amplify the PSD analog outputs. For the small angles, the displacement of the laser spot on the PSD is about $10\mu m$, while the noise on the electronics, used for the Sitek PSD, is of an order of magnitude of $5\mu m$. For larger angles, this influence becomes relatively smaller.

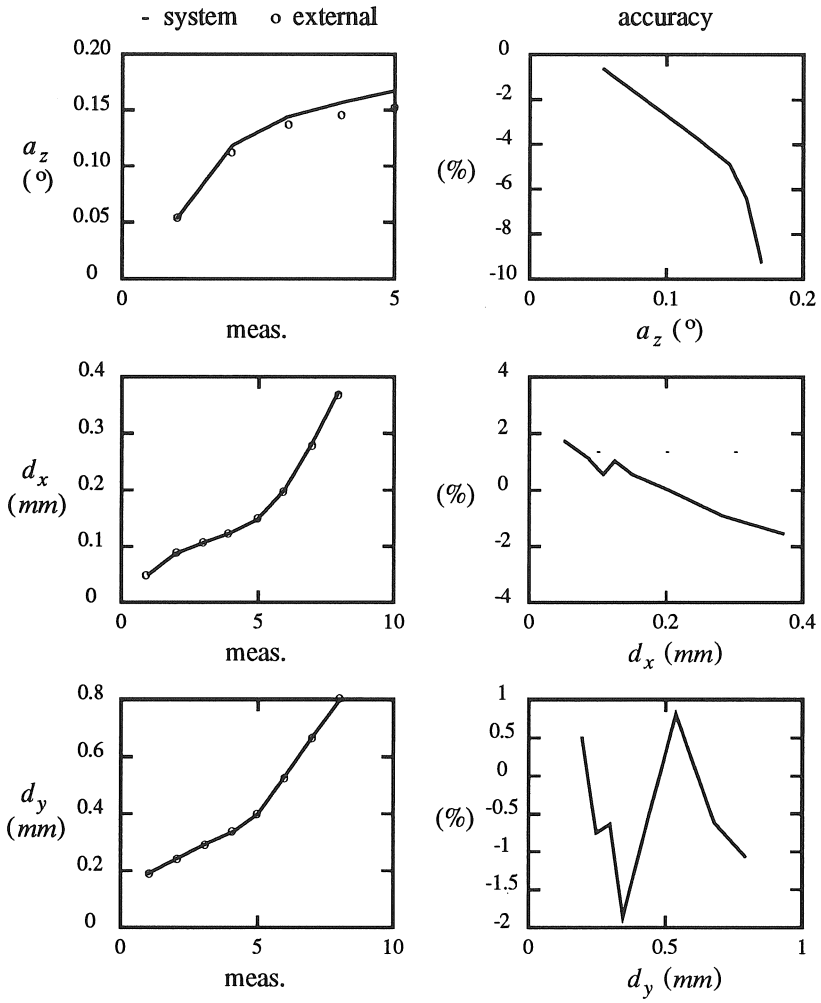

Figure 3.34: Accuracy deflection measurements d_x, d_y and a_z.

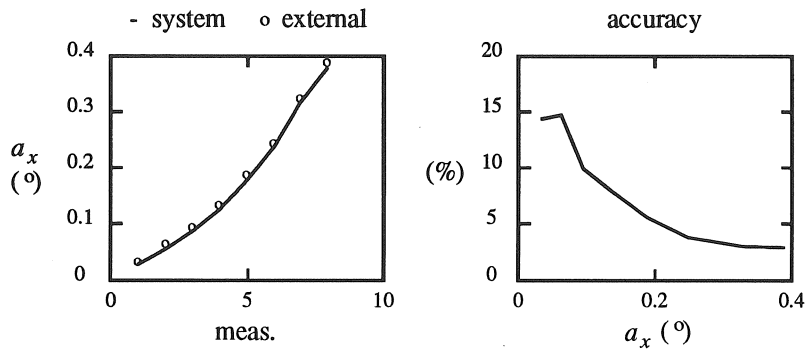

Figure 3.35: Accuracy deflection measurements a_x.

Deflection	Accuracy
d_x	2%
d_y	2%
a_x	2–15%
a_y	2-15%
a_z	10%

Table 3.8: Accuracy of optical link deflection measurement system.

3.6.4 Conclusion

Table 3.8 summarizes the accuracy of the optical link deflection measurement system. These results correspond to the predictions of the accuracy analysis, carried out in [77]. For the bending angles a_x and a_y, the accuracy improves for larger angles.

3.7 Conclusion

This chapter elaborates on the details of real-time link deflection measurements. Section 1.3 has showed that strain gauges and optical detectors are suitable devices to build a link deflection sensor. In this chapter, both methods are investigated and tested for the desired features of a link deflection sensor. The strain gauges based deflection measurement method appears to suffer from a lot of disadvantages, making this method not quite advisable to measure structural deflections. The within this chapter presented optical system meets most

of the required features. For some situations for which the presented optical system does not satisfy, alternative systems are proposed. Finally, an experimental laser diode optical link deflection sensor, called **DIOMEDES** (laser **DI**ode **O**ptical system for **ME**asuring structural **DE**flection**S**), demonstrates the feasibility of a laser diode optical system to determine in *real-time* the *spatial* structural deflections of a flexible link. The results are satisfactory: the accuracy of this measurement system varies between 2% and 10% for the different structural deflections. This could be even improved while most of the errors are due to noise of the electronics which amplifies the analog outputs of the PSD's. Also the real-time character of the measurement system has been proved: to measure the six co-ordinates and to calculate the five structural deflections it takes, on a PC-AT, less than $5ms$. The real-time measurement of the spatial structural deflections of a flexible link is crucial to improve the accuracy of the tracking control of flexible manipulators. This is shown in section 2.3.2.2.

Conclusions

This thesis presents a new experimental technique for the compliance breakdown of complex mechanical structures, including a new method to correct the influence of gravitation on translational accelerometer measurements, and demonstrates the feasibility of a strain gauges based system and of an optical transducers based system to determine in real-time the spatial structural deflections of a flexible beam.

The new quasi-static compliance breakdown technique presented within this thesis allows to identify and to quantify *experimentally* and *configuration-independently* the compliances of *all components* of complex mechanical structures. This new method permits to determine the compliances of a component without measuring the whole robot.

In this thesis, the compliance breakdown of serial driven industrial robots is emphasized. For this type of robots following components are considered: prismatic long links, revolute joints and the robot base. Because of the modular structure of this technique, and of the corresponding software package developed within this thesis, other types of components and other compliance models can be easily included.

To perform an accurate compliance breakdown, this thesis presents a new method to correct the influence of gravitation on translational accelerometer measurements. The author is not aware of the existence of any other method which compensates the influence of gravitation on translational accelerometer measurements, although it is essential. In fact, all people using translational accelerometer measurements encounter this phenomenon, but as they measure at higher frequencies they neglect, in many cases without knowing, this influence.

The results of the compliance breakdown contribute to potential improvement of robot precision in several ways; such as in robot de-

sign improvement, in the prediction and compensation of robot endpoint deflection, or in the selection of, for a given task, best robot posture and best workpiece position with respect to the robot arm. For the latter application, the software developed within this thesis allows to analyze the spatial deformation behaviour of a robot within its workspace.

The experimental compliance breakdown performed on a clamped-free beam shows that the accuracy of the quasi-static compliance breakdown method is very good, and that the influence of the inertial forces on the results of the quasi-static compliance breakdown is negligible, provided that the excitation frequency is well chosen. The experimental compliance breakdown performed on an industrial robot shows that the quasi-static compliance breakdown method is very appropriate to determine the compliance of the joints of a complex mechanical structure. On the other hand, the determination of the compliance parameters of the links and of the base of the robot poses some problems. In a future implementation, the use of an angular accelerometer beside the already used translational accelerometer could solve the biggest problem for having an accurate quasi-static compliance breakdown of the links and of the base of a complex mechanical structure. However, the at the moment commercially available angular motion sensors are not usable for this type of application.

This thesis also demonstrates the feasibility of a strain gauges based system and of an optical transducers based system to determine in *real-time* the *spatial* structural deflections of a flexible beam. The strain gauges based deflection measurement method appears to suffer from a lot of disadvantages, making this method not quite advisable to measure structural deflections. The within this thesis presented optical system meets most of the required features. For some situations for which the presented optical system does not satisfy, this thesis introduces two alternative systems which could be developed in future.

This thesis presents an experimental laser diode optical link deflection sensor, called *DIOMEDES* (laser *DI*ode *O*ptical system for *ME*asuring structural *DE*flection*S*) which is able to determine in *real-time* the *spatial* structural deflections of a flexible link. The results are satisfactory: the accuracy of this measurement system varies between 2% and 10% for the different structural deflections. This could be even

improved while most of the errors are due to noise of the electronics which amplifies the analog outputs of the PSD's. Also the real-time character of the measurement system has been proved: to measure the six co-ordinates and to calculate the five structural deflections it takes, on a PC-AT, less than $5ms$. The real-time measurement of the spatial structural deflections of a flexible link is crucial to improve the accuracy of the tracking control of flexible manipulators.

Bibliography

[1] D. TESAR, E. KAMEN, *Preliminary proposal: Control-in-the-small technology for enhanced precision under load for machining with industrial robots*, CIMAR, University of Florida, 1983.

[2] J.H. GILBY, G.A. PARKER, *Laser tracking system to measure robotarm performance*, Sensor Review, Vol. 2, October 1982, pp. 180-184.

[3] K. LAU, R.J. HOCKEN, W.C. HAIGHT, *Automatic laser tracking interferometer system for robot metrology*, Precision Engineering, Vol. 8, No. 1, 1986, pp. 3-8.

[4] B. BAES, P. BLANCKAERT, *Directe eindpuntmeting van robots* (in Dutch), Department of Mechanical Engineering, K.U.Leuven, 1988, 88EP26.

[5] J.Y.S. LUH, M.W. WALKER, R.P.C. PAUL, *On-line computational scheme for mechanical manipulators*, Transactions of ASME, Journal of Dynamic Systems, Measurement, and Control, Vol. 102, June 1980, pp. 69-76.

[6] E.I. RIVIN, *Compilation and compression of mathematical model for a machine transmission*, Design Engineering Technical Conference, Beverly Hills, CA, 1980.

[7] E.I. RIVIN, *Mechanical design of robots*, McGraw-Hill Book Company, New York, 1988.

[8] D.E. WHITNEY, C.A. LOZINSKI, J.M. ROURKE, *Industrial robot forward calibration methods and results*, Transactions of ASME, Journal of Dynamic Systems, Measurement, and Control, Vol. 108, March 1986, pp. 1-8.

[9] C.A. LOZINSKI, *Robot calibration*, Master's Thesis, Department of Mechanical Engineering, Massachusetts Institute of Technology, 1984.

[10] H.A. ELMARAGHY, B. JOHNS, *An investigation into the compliance of SCARA robots. Part II: Experimental and numerical validation*, Transactions of ASME, Journal of Dynamic Systems, Measurement, and Control, Vol. 110, March 1988, pp. 23-30.

[11] M.C. LEU, V. DUKOVSKI, K.K. WANG, *Effect of mechanical compliance on deflection of robot manipulators*, Annals of the CIRP, Vol. 36/1, 1987, pp. 305-309.

[12] M.E. SKLAR, *Metrology and calibration techniques for the performance enhancement of industrial robots*, Ph.D. Dissertation, Department of Mechanical Engineering, University of Texas, Austin, 1988.

[13] J. TLUSTY, E. STERN, *Use of a structural model in compensating for robot deflections*, Annals of the CIRP, Vol. 34/1, 1985, pp. 357-363.

[14] E.L. STERN, *Modeling of a robot structure for compensation of deflections in light machines*, Master's Thesis, University of Florida, Gainesville, 1985.

[15] F. BEHI, *Dynamic analysis and parametric identification for flexible serial manipulators*, Ph.D. Dissertation, University of Florida, Gainsville, 1985.

[16] A. KURTOGLU, *Holographic measurement of industrial robots*, Robotics & Computer-Integrated Manufacturing, Vol. 5, No. 2/3, 1989, pp. 145-152.

[17] A. KURTOGLU, *Holography-aided testing of industrial robots*, Journal of Manufacturing Systems, Vol. 8, No. 4, 1989, pp. 297-305.

[18] M. WECK, R. ECKSTEIN, *An examination technique to determine static weakpoints of machine tools*, Annals of the CIRP, Vol. 36/1, 1987, pp. 257-261.

[19] R. ECKSTEIN, *Beurteilung der Statischen Last-Verformungs-eigenschaften von Werkzeugmaschinen mit Hilfe der Quasi-statischen Messtechnik* (in German), Ph.D. Dissertation, WZL TH Aachen, 1988.

[20] M. WECK, R. ECKSTEIN, W. SCHÄFER, *An examination technique to determine static weakpoints of machine tools*, 13^{th} International Seminar on Modal Analysis, K.U.Leuven, September 1988.

[21] R. CANNON, E. SCHMITZ, *Initial experiments on the end-point control of a flexible one-link robot*, International Journal of Robotics Research, Vol. 3, No. 3, 1984, pp. 62-75.

[22] B. GEBLER, *Feed-forward control strategy for an industrial robot with elastic links and joints*, 1987 IEEE International Conference on Robotics and Automation, Raleigh, April 1987, pp. 923-928.

[23] S. RAMAKRISHNAN, *Experimental identification and control of the tip position of a flexible, single link manipulator*, Ph.D. Dissertation, Department of Mechanical Engineering, University of California, Berkeley, 1985.

[24] A.J. BAKER, *Analysis and design of a capacitive angle transducer*, Master of Engineering project paper, Department of Electrical Engineering, Bringham Young University, 1980.

[25] J. SWEVERS, D. TORFS, J. DE SCHUTTER, H. VAN BRUSSEL, *Accurate tracking control of a flexible one-link robot*, 15th International Seminar on Modal Analysis, K.U.Leuven, September 1990, pp. 353-366.

[26] J. SWEVERS, M. ADAMS, J. DE SCHUTTER, H. VAN BRUSSEL, H. THIELEMANS, *Limitations of linear identification and control techniques for flexible robots with nonlinear joint friction*, Experimental Robotics 1, Lecture notes in control and information science (1th International Symposium on Experimental Robotics, Montreal, Canada, 1989), Springer-Verlag, 1990, pp. 91-106.

[27] D. TORFS, J. SWEVERS, J. DE SCHUTTER, *Extended bandwidth zero phase error tracking control of non-minimal phase systems*,

accepted for publication in Transactions of the ASME, Journal of Dynamic Systems, Measurement and Control.

[28] J. SWEVERS, *Linear identification and control of flexible robots*, Ph.D. Dissertation, Department of Mechanical Engineering, K.U.Leuven, 1992, 92D1.

[29] W.J. BOOK, T.E. ALBERTS, G.G. HASTINGS, *Design strategies for high-speed lightweight robots*, Computers in Mechanical Engineering, Vol. 5, September 1986, pp. 26-33.

[30] A. ZALUCKY, D.E. HARDT, *Active control of robot structure deflections*, Transactions of ASME, Journal of Dynamic Systems, Measurement, and Control, Vol. 106, March 1984, pp. 63-69.

[31] P.C. MULDERS, A.C.H. VAN DER WOLFF, C.J. HEUVELMAN, M.P. SNIJDER VAN WISSEKERKE, *A robot-arm with compensation for bending*, Annals of the CIRP, Vol. 35/1, 1986, pp. 305-308.

[32] M. UCHIYAMA, A. KONNO, *Laser optical measurement of robot structural deflections*, International Conference on Advanced Mechatronics, Tokyo, May 1989, pp. 353-357.

[33] M. PREVOST, M. PAVLIN, *Le squelette optique: mesure et compensation des deformations d'une structure articulée*, Mesucora, 1985.

[34] S.P. TIMOSHENKO, J.M. GERE, *Mechanics of materials*, Van Nostrand Reinhold Company, 1971.

[35] N., *Mini-pal model 2180 servo accelerometer*, Sundstrand Data Control Inc., 1978.

[36] , *G.H. Golub, C.F. Van Loan, Matrix Computations*, North Oxford Academic Publishers Ltd, John Hopkins University Press, London, 1986.

[37] E.I. RIVIN, *Compliance break-down for robot structures*, 7^{th} Symposium on Engineering Applications of Mechanics, University of Toronto, 1984, pp. 56-67.

[38] M. WECK,*Analyse und Optimierung des statischen, dynamischen und thermischen lastverformungsverhaltens von handhabungsgeräten*, Ergebnisbericht des Sonderforschungsbereiches 208 "Grundlagen und komponenten flexibeler handhabungsgeräte im maschinenbau", RWTH Aachen, März 1988.

[39] M. WECK, H. STAVE, *A method of optimizing gantry robot stiffness*, 16^{th} International Symposium on Industrial Robots, Brussels, 1986, pp. 159-174.

[40] L. NUYTTENS, *Optimisation of gantry robots with F.E. methods*, Department of Mechanical Engineering, K.U.Leuven, WZL, RWTH Aachen, 1990, 90ER04.

[41] T. ROSENBAUER, H. VONDERHAGEN, *Programmsystem zur optimierung des lastverformungsverhaltens von industrierobotern*, Industrie-Anzeiger, No. 12, 1989, pp. 36-37.

[42] E.I. RIVIN, *Effective rigidity of robot structures: analysis and enhancement*, American Control Conference, 1985, pp. 381-382.

[43] H. WEST, H. ASADA, *Kinematic analysis and mechanical advantage of manipulators constrained by contact with the environment*, Robotics and Manufacturing Automation (Eds. M. Donath, M. Leu), Vol. PED-15, ASMA, New York, 1985, pp. 175-186.

[44] F. FEYERABEND, *Systematic optimisation of a robot arm structure*, The Industrial Robot, Vol. 15, No. 4, 1988, pp.219-222.

[45] D.A. FRESONKE, E. HERNANDEZ, D. TESAR, *Deflection prediction for serial manipulators*, 1988 IEEE International Conference on Robotics and Automation, Philadelphia, April 1988, pp. 482-487.

[46] D.A. FRESONKE, *Deflection prediction for quasi-static serial manipulators*, Ph.D. Dissertation, Department of Mechanical Engineering, University of Texas, Austin, 1985.

[47] M. SKLAR, D. TESAR, *Dynamic analysis of hybrid serial manipulator systems containing parallel modules*, Transactions of ASME, Journal of Mechanisms, Transmissions, and Automation in Design, Vol. 110, June 1988, pp. 109-115.

[48] C. BAGCI, *Computer-aided continuous correction of end-effector position and orientation errors in industrial robots due to elastic deformations*, ASME Mechanisms Conference, Cambridge, CA, 1984.

[49] J. HUDGENS, *Modeling and analysis of a fully- parallel six degree-of-freedom micromanipulator*, Master's Thesis, University of Florida, Gainesville, 1986.

[50] J.P. WANDER, D. TESAR, *Pipelined computation of manipulator modeling matrices*, IEEE Journal of Robotics and Automation, Vol. RA-3, No. 6, December 1987, pp. 556-566.

[51] F. DEMEESTER, H. VAN BRUSSEL, *Real-time optical measurement of robot structural deflections*, Mechatronics, Vol. 1, No. 1, 1991, pp. 73-86.

[52] J. SWEVERS, D. TORFS, F. DEMEESTER, H. VAN BRUSSEL, *Fast and accurate tracking control of a flexible one-link robot based on real-time link deflection measurements*, Mechatronics, Vol. 2, No. 1, 1992, pp. 29-41.

[53] M. TOMIZUKA, *Zero phase error tracking algorithm for digital control*, Transactions of ASME, Journal of Dynamic Systems, Measurement, and Control, Vol. 109, 1987, pp. 65-68.

[54] D. TORFS, J. SWEVERS, J. DE SCHUTTER, *An optimal continuous path control approach including a model based feedforward calculation*, Internal report, Department of Mechanical Engineering, K.U.Leuven, 1990.

[55] D.E. WHITNEY, *The remote center compliance*, The International Encyclopedia of Robotics, John Wiley & Sons, New York, 1988, pp. 1316-1324.

[56] N., *PM vibration exciter type 4809*, Brüel & Kjær.

[57] N., *Vibration exciter system V: Exciter body type 4801 and Big table head type 4813*, Brüel & Kjær.

[58] N., *Quartz load washers type 9001 ... 9091*, Kistler Instrumente AG.

[59] N., *Charge amplifier type 5007*, Kistler Instrumente AG.

[60] N., *TP-4X lowpass filter*, GEPA.

[61] H. VAN DER AUWERAER, *Development and evaluation of advanced measurement methods for experimental modal analysis*, Ph.D. Dissertation, Department of Mechanical Engineering, K.U.Leuven, 1987, 87D3.

[62] N., *PC AT 286/10*, DATEC.

[63] N., *Translational and angular acceleration measuring system TAP, type 8832*, Kistler Instrumente AG, 1990.

[64] N., *Angular motion velocity sensor, model 361A*, PCB Piezotronics Inc., 1990.

[65] B. COSAERT, H. DERACHE, *Experimentele identifikatie van de statische soepelheid bij industriële robots* (in Dutch), Department of Mechanical Engineering, K.U.Leuven, 1989, 89EP24.

[66] S. TIMOSHENKO, J.N. GOODIER, *Theory of elasticity*, McGraw-Hill Book Company, New York Toronto London Tokyo, 1951.

[67] K. BECKSTEDDE, C. VAN DER GUCHT, *Vervormingsmetingen van robotgelederen* (in Dutch), Department of Mechanical Engineering, K.U.Leuven, 1989, 89EP03.

[68] N., *Precision strain gauges*, Micro-Measurements Div., Measurements Group Inc.

[69] R.W. JAMES, *Strain-gage misalignment errors - a special case of interest*, Experimental Techniques, Vol. 12, June 1988, pp. 28-29.

[70] N., *High specification silicon photodetectors*, Centronic.

[71] Y. YUANHAI, *The design of echo spot and optical focusing in automatic laser tracking*, Optics and Laser Technology, Vol. 18, No. 2, 1986, pp. 75-79.

[72] N., *CCD solid state imaging technology*, Fairchild Weston, 1987.

[73] N., *Position-sensitive detectors*, Hamamatsu Photonics K.K., April 1987.

[74] N., *Optics 4*, Melles Griot, 1988.

[75] H. KOEBNER, *Industrial applications of lasers*, John Wiley & Sons, New York, 1984.

[76] N., *Kodak IR phosfor*, Eastman Kodak Company, 1980.

[77] J. ARRAS, W. PERSOONS, *Optisch meetsysteem voor het bepalen van statische en dynamische vervormingen van robotgelederen* (in Dutch), Department of Mechanical Engineering, K.U.Leuven, 1990, 90EP05.

[78] F. DEMEESTER, H. VAN BRUSSEL, *Experimental compliance breakdown of industrial robots*, Submitted for publication in Transactions of the ASME: Journal of Mechanisms, Transmissions, and Automation in Design.

[79] N., *Laser rotary encoder*, Canon U.S.A. Inc., 1989.

[80] D.C. O'SHEA, *Elements of modern optical design*, John Wiley & Sons, New York Toronto Singapore, 1985.

[81] N., *Small size collimator pen CQL73*, Philips N.V., 1989.

[82] N., *1989/90 Data conversion products databook*, Analog Devices Inc., 1989.

[83] N., *Position sensing detectors PSD*, Sitek Electro Optics, October 1988.

[84] N., *Lab Master DMA handbook*, Scientific Solutions Inc., 1987.

[85] J.J. CRAIG, *Introduction to robotics: Mechanics & Control*, Addison-Wesley, Reading, MA, 1986.

[86] J. DENAVIT, R.S. HARTENBERG, *A kinematic notation for lower pair mechanisms based on matrices*, Transactions of ASME, Journal of Applied Mechanics, Vol. 22, No. 3, June 1955, pp. 215-221.

[87] L. VAN AKEN, H. VAN BRUSSEL, *Software for solving the inverse kinematic problem for robot manipulators in real-time*, 1^{st} Conference on Advanced Software for Robotics, Liège, Belgium, 1983.

Appendix A

Relation between the dynamic and static compliance behaviour of a mechanical system

A.1 Introduction

Figure A.1 shows the frequency response of a flexible clamped-free beam (cf. section 2.4.2.5). The static compliance of the beam is evidently to be found at a frequency of $0Hz$. However, within a certain region, the so-called *quasi-static range*, the dynamic and static compliance behaviour of the beam are in a first order identical. In order to predict the accuracy of this identity, this appendix derives a mathematical expression to describe the relation between the dynamic and static compliance behaviour of a mechanical system.

A.2 Derivation of the mathematical expression

The dynamic behaviour of a mechanical system is derived using a single degree-of-freedom mass-spring-damper model (figure A.2). This type of model is satisfactory. A lumped mass model is to complex and would not improve a lot the accuracy of the derived equations.

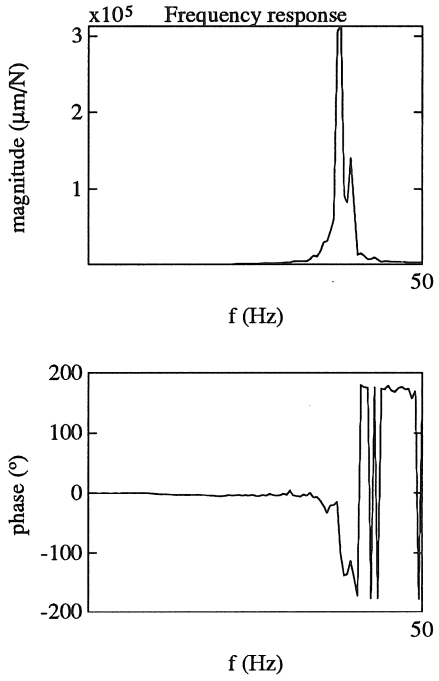

Figure A.1: Frequency response of a flexible clamped-free beam.

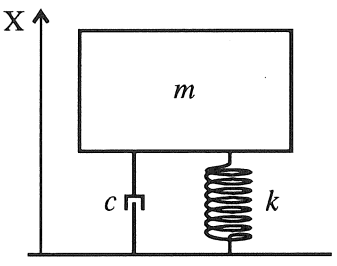

Figure A.2: Single degree-of-freedom mass-spring-damper system.

The dynamical behaviour of a single degree-of-freedom mass-spring-damper system is described by:

$$F = m\ddot{x} + c\dot{x} + kx, \tag{A.1}$$

with m the equivalent mass of the system, c the damping constant and k the static stiffness of the system. Transforming this equation to the frequency domain yields:

$$F = x[(-m\omega^2 + k) + jc\omega]. \tag{A.2}$$

Substituting the subsequent equations for the first natural frequency of the system, $f_n = \frac{\omega_n}{2\pi}$, and for the corresponding damping ratio, ζ:

$$\omega_n = \sqrt{\frac{k}{m}}, \tag{A.3}$$

$$\zeta = \frac{c}{2\sqrt{km}} = \frac{c}{2k}\omega_n, \tag{A.4}$$

into equation A.2 yields:

$$F = kx[(1 - \omega_{sn}^2) + 2j\zeta\omega_{sn}], \tag{A.5}$$

with

$$\omega_{sn} = \frac{\omega}{\omega_n}. \tag{A.6}$$

Using equation A.5, the dynamic compliance behaviour of the system is described by:

$$\frac{x}{F} = \frac{1}{k}\left[\frac{1}{(1 - \omega_{sn}^2) + 2j\zeta\omega_{sn}}\right], \tag{A.7}$$

where $\frac{1}{k}$ gives the static compliance of the system. For frequencies far below the first natural frequency ($\omega_{sn}^2 \ll 1$), and taking into consideration the small value of the damping ratio ζ, equation A.7 becomes:

$$\frac{x}{F} = \frac{1}{k}\left[\frac{1}{(1 - \omega_{sn}^2)}\right]. \tag{A.8}$$

With $\frac{1}{k}$ defining the static compliance of the system, and equation A.8 defining the corresponding dynamic compliance, the accuracy of the identity between the dynamic and static compliance behaviour of the

mechanical system for a certain excitation frequency is given by following formula:

$$\frac{1}{(1-\omega_{sn}^2)} - 1. \tag{A.9}$$

Following example demonstrates how to choose in the quasi-static compliance breakdown method for a desired accuracy the excitation frequency f_{qs} with respect to the corresponding first natural frequency f_n of the considered system.

Suppose $f_n = 13Hz$, or $\omega_n = 26\pi rad$, and consider two different desired accuracies: 1% and 5%.

Using formula A.9, and the relation $f_{qs} = \frac{\omega}{2\pi}$, following excitation frequencies are derived:

Accuracy	f_{qs}
1%	$1.3Hz$
5%	$3.0Hz$

Appendix B

Homogeneous transforms

B.1 Introduction

A homogeneous transform is a 4×4 matrix which for our purposes can be regarded purely as a construction used to cast the rotation and translation of a general transform into a single matrix [85].

The homogeneous transform ${}^0\mathbf{A}_1$ transforms the cartesian co-ordinates of a point P defined in the co-ordinate frame $\{X_1, Y_1, Z_1\}$, = $\{1\}$, to the corresponding cartesian co-ordinates of this point P defined in the co-ordinate frame $\{X_0, Y_0, Z_0\}$, = $\{0\}$ (figure B.1).

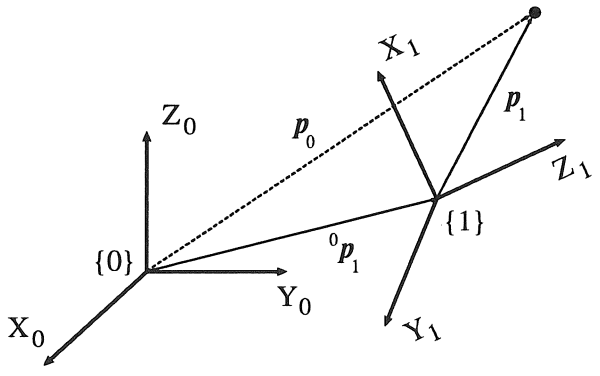

Figure B.1: General transform of a vector.

The transformation is given by:

$$\underbrace{\begin{bmatrix} x_0 \\ y_0 \\ z_0 \\ \hline 1 \end{bmatrix}}_{\mathbf{p}_0} = \underbrace{\left[\begin{array}{ccc|c} & {}^0\mathbf{R}_1 & & {}^0\mathbf{p}_1 \\ \hline 0 & 0 & 0 & 1 \end{array}\right]}_{{}^0\mathbf{A}_1} \underbrace{\begin{bmatrix} x_1 \\ y_1 \\ z_1 \\ \hline 1 \end{bmatrix}}_{\mathbf{p}_1}. \tag{B.1}$$

The vector ${}^0\mathbf{p}_1$ locates the origin of frame $\{1\}$ within frame $\{0\}$. This vector is a 3×1 vector and is called the position vector. The matrix ${}^0\mathbf{R}_1$ describes the rotation of frame $\{1\}$ with respect to frame $\{0\}$. This matrix is a 3×3 matrix and is called the orientation matrix. Note that while we have introduced homogeneous transforms in the context of general transformations, they also serve as descriptions of frames. The description of frame $\{1\}$ relative to frame $\{0\}$ is given by ${}^0\mathbf{A}_1$.

The homogeneous transform into two dimensions is a simplification of the general homogeneous transform into three dimensions. The transformation becomes:

$$\begin{bmatrix} x_0 \\ y_0 \\ \hline 1 \end{bmatrix} = \left[\begin{array}{cc|c} & {}^0\mathbf{R}_1 & {}^0\mathbf{p}_1 \\ \hline 0 & 0 & 1 \end{array}\right] \begin{bmatrix} x_1 \\ y_1 \\ \hline 1 \end{bmatrix}, \tag{B.2}$$

where ${}^0\mathbf{p}_1$ is a 2×1 vector, and ${}^0\mathbf{R}_1$ is a 2×2 matrix.

B.2 Inverse homogenous transforms

The inverse homogeneous transform ${}^1\mathbf{A}_0$ transforms the cartesian co-ordinates of a point P defined in the co-ordinate frame $\{0\}$, to the corresponding cartesian co-ordinates of this point P defined in the co-ordinate frame $\{1\}$.

The inverse homogeneous transform ${}^1\mathbf{A}_0$ is calculated by taking the inverse of ${}^0\mathbf{A}_1$. As the orientation matrix ${}^0\mathbf{R}_1$ is an orthonormal matrix

$${}^0\mathbf{R}_1^{-1} = {}^0\mathbf{R}_1{}^t, \tag{B.3}$$

where $\bullet^t$ means the transpose of $\bullet$. Using this property, the inverse homogeneous transform ${}^1\mathbf{A}_0$ can be calculated as follows:

$$ {}^{1}\mathbf{A}_{0} = \begin{bmatrix} & {}^{0}\mathbf{R}_{1}{}^{t} & & -{}^{0}\mathbf{R}_{1}{}^{t}\,{}^{0}\mathbf{p}_{1} \\ 0 & 0 & 0 & 1 \end{bmatrix}. \tag{B.4} $$

B.3 Translations and rotations

Translations along and rotations about the axes of a co-ordinate frame can be represented by homogeneous transforms. The possible translations and rotations are stated below. The first parameter stands for the axis along which or about which the transformation is carried out, the second parameter stands for the translation distance along or the rotation angle about this axis.

$$ \begin{aligned} \mathit{Translation}(X, d_x) &= \begin{bmatrix} 1 & 0 & 0 & d_x \\ 0 & 1 & 0 & 0 \\ 0 & 0 & 1 & 0 \\ 0 & 0 & 0 & 1 \end{bmatrix}, \\ \mathit{Translation}(Y, d_y) &= \begin{bmatrix} 1 & 0 & 0 & 0 \\ 0 & 1 & 0 & d_y \\ 0 & 0 & 1 & 0 \\ 0 & 0 & 0 & 1 \end{bmatrix}, \\ \mathit{Translation}(Z, d_z) &= \begin{bmatrix} 1 & 0 & 0 & 0 \\ 0 & 1 & 0 & 0 \\ 0 & 0 & 1 & d_z \\ 0 & 0 & 0 & 1 \end{bmatrix}. \end{aligned} \tag{B.5} $$

$$ \begin{aligned} \mathit{Rotation}(X, a_x) &= \begin{bmatrix} 1 & 0 & 0 & 0 \\ 0 & c_x & -s_x & 0 \\ 0 & s_x & c_x & 0 \\ 0 & 0 & 0 & 1 \end{bmatrix}, \\ \mathit{Rotation}(Y, a_y) &= \begin{bmatrix} c_y & 0 & s_y & 0 \\ 0 & 1 & 0 & 0 \\ -s_y & 0 & c_y & 0 \\ 0 & 0 & 0 & 1 \end{bmatrix}, \end{aligned} $$

$$Rotation(Z, a_z) = \begin{bmatrix} c_z & -s_z & 0 & 0 \\ s_z & c_z & 0 & 0 \\ 0 & 0 & 1 & 0 \\ 0 & 0 & 0 & 1 \end{bmatrix}. \qquad \text{(B.6)}$$

Appendix C

Influence of gravitation on translational accelerometer measurements

C.1 Introduction

If translational accelerometers are subject to rotation, gravitation influences the measured accelerations. This results from the principle of operation of translational accelerometers.

To perform an accurate compliance breakdown, a new method is developed to correct the influence of gravitation on translational accelerometer measurements. The author is not aware of the existence of any other method which compensates the influence of gravitation on translational accelerometer measurements, although it is essential. In fact, all people using translational accelerometer measurements encounter this phenomenon, but as they measure at higher frequencies they neglect, in many cases without knowing, this influence.

C.2 Influence of gravitation on translational accelerometer measurements

C.2.1 Pure translational accelerometers

Due to their principle of operation, translational accelerometers can be sensitive to gravitation if they are subject to rotation.

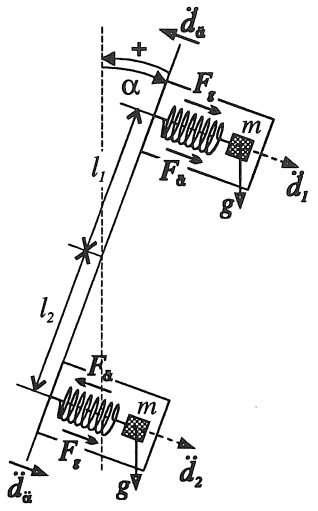

Figure C.1: Influence of gravitation on the acceleration measurement.

All commonly used translational accelerometers can be modelled as mass-spring systems fixed to a base which is subject to accelerations. The movement of the seismic mass relative to the movement of the base, or the force of the mass exerted on the spring, are a measure for the exerted translational acceleration on the system. The measurement of this movement, or of this force, provides, in the considered frequency range, the desired measure of the translational acceleration.

If translational accelerometers are subject, in addition to translation, to rotation, gravitation influences the measured accelerations. Figure C.1 gives a schematic representation of the measurement of the translational acceleration in a point of a rigid plane which is subject to a sinusoidal angular acceleration, $\ddot{\alpha}$. In order to see better the influence of gravitation on the measurements, two measurement points are considered. For the sake of simplicity, only a two-dimensional structure is considered; section C.3 gives a general mathematical description of the influence of gravitation on translational accelerometer measurements. The corresponding equations are

$$\ddot{\alpha} = \ddot{\alpha}_a \sin(2\pi f t), \tag{C.1}$$

$$\alpha = \alpha_a \sin(2\pi f t); \tag{C.2}$$

with

$$\alpha_a = -\frac{\ddot{\alpha}_a}{(2\pi f)^2}, \tag{C.3}$$

where α is the corresponding rotation angle of the rigid plane, $\bullet_a$ is the amplitude of the sinusoidal signal $\bullet$, and f is the frequency of the sinusoidal signal.

Suppose the rigid plane is subject to a sinusoidal angular acceleration $\ddot{\alpha}$, and *no gravitation* acts on the accelerometers. The forces $F_{\ddot{\alpha}}$ exerted on the spring of the accelerometers equal

$$F_{\ddot{\alpha}1} = m\, l_1\, \ddot{\alpha}, \tag{C.4}$$
$$F_{\ddot{\alpha}2} = -m\, l_2\, \ddot{\alpha}. \tag{C.5}$$

Elongation of the spring is considered positive and compression negative. The measured accelerations $\ddot{d}$, which are in the considered frequency range proportional to the forces $F_{\ddot{\alpha}}$ exerted on the springs, equal

$$\ddot{d}_1 = -l_1\, \ddot{\alpha}, \tag{C.6}$$
$$\ddot{d}_2 = l_2\, \ddot{\alpha}. \tag{C.7}$$

If however *gravitation* acts on the accelerometers, the forces $F_{\ddot{\alpha}}$ exerted on the spring of the accelerometers equal

$$F_{\ddot{\alpha}1} = m\, l_1\, \ddot{\alpha} - m\, g\, \sin\alpha, \tag{C.8}$$
$$F_{\ddot{\alpha}2} = -m\, l_2\, \ddot{\alpha} - m\, g\, \sin\alpha; \tag{C.9}$$

where g is the gravitational acceleration ($9.81 \frac{m}{s^2}$ in the considered location). In figure C.1 $\ddot{\alpha}$ is positive and α is negative, yielding

$$\ddot{d}_1 = -l_1\, \ddot{\alpha} + g\, \sin\alpha, \tag{C.10}$$
$$\ddot{d}_2 = l_2\, \ddot{\alpha} + g\, \sin\alpha. \tag{C.11}$$

For small angles α, $\sin\alpha = \alpha$; previous equations become

$$\ddot{d}_1 = -l_1\, \ddot{\alpha} + g\, \alpha, \tag{C.12}$$
$$\ddot{d}_2 = l_2\, \ddot{\alpha} + g\, \alpha. \tag{C.13}$$

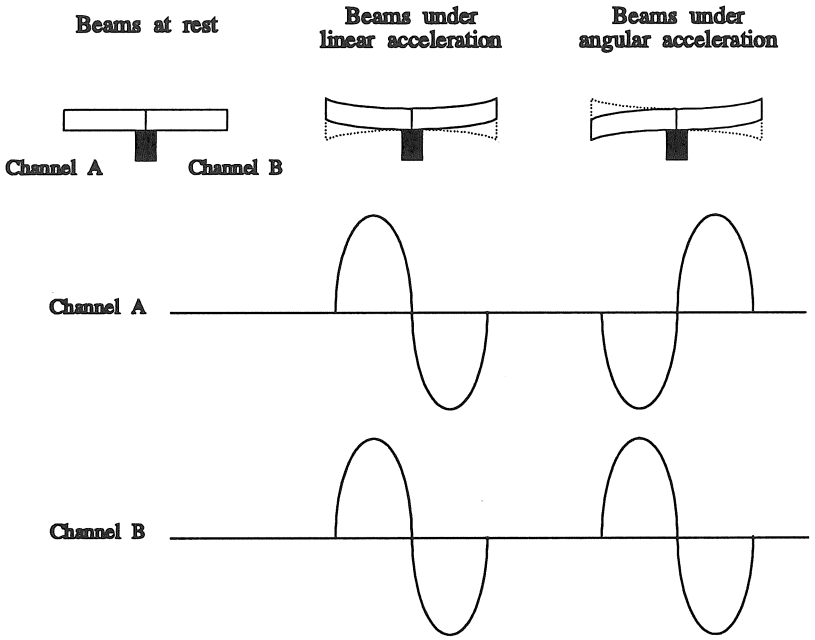

Figure C.2: Simplified beam motion and resulting output.

As in those equations no phase shift, or a phase shift of 180°, exists between the sinusoidal signals, the amplitude of the measured accelerations $\ddot{d}_a$ equal

$$\ddot{d}_{a1} = -l_1 \ddot{\alpha}_a + g\,\alpha_a, \tag{C.14}$$

$$\ddot{d}_{a2} = l_2 \ddot{\alpha}_a + g\,\alpha_a. \tag{C.15}$$

C.2.2 Combined translational and angular accelerometers

Recently, KISTLER INSTRUMENTE AG introduced a combined translational and angular acceleration measuring system; TAP - *Translational Angular Piezobeam* [63]. The system uses two cantilever beams, made of a piezoelectric ceramic bimorph, to measure simultaneously translational and angular accelerations. The two beams are arranged as shown in figure C.2 [63]. The output of the beams is an electrical charge signal whose charge polarity is shown in figure C.2. The beams will experience a slight deflection upon acceleration. If the acceleration

is purely translational, the beams will flex in the same direction. Under angular acceleration, the two beams will flex in opposite directions. The resulting electrical signals for a periodic acceleration vibration are also shown: translational acceleration produces signals which are in phase, whereas angular acceleration produces signals having opposite phase. Combining in a proper way the four electrical charge signals of the beams yields the translational and the angular component of the acceleration.

Also this acceleration measuring system is sensitive to gravitation if it is subject to rotation. However only the translational component of the acceleration is sensitive, not the angular component if the measuring system is perfectly symmetric. As the angular component can be measured directly, the translational component can be easily compensated for the gravitational influence due to rotation.

C.3 General mathematical description of the influence of gravitation on translational accelerometer measurements

C.3.1 Derivation of the general mathematical description

Figure C.3 shows the different co-ordinate frames relevant for the general mathematical description of the translational accelerations in a structural point P_i of a rigid plane W.

If the plane W undergoes a general, sinusoidal acceleration $\ddot{\mathcal{D}}_w$, with

$$\ddot{\mathcal{D}}_w = \begin{bmatrix} \ddot{\mathbf{d}}_w \\ \ddot{\mathbf{a}}_w \end{bmatrix},$$

$$\ddot{\mathbf{d}}_w = \begin{bmatrix} \ddot{d}_x \\ \ddot{d}_y \\ \ddot{d}_z \end{bmatrix},$$

$$\ddot{\mathbf{a}}_w = \begin{bmatrix} \ddot{a}_x \\ \ddot{a}_y \\ \ddot{a}_z \end{bmatrix}.$$

the translational acceleration vector in the point P_i, defined in the

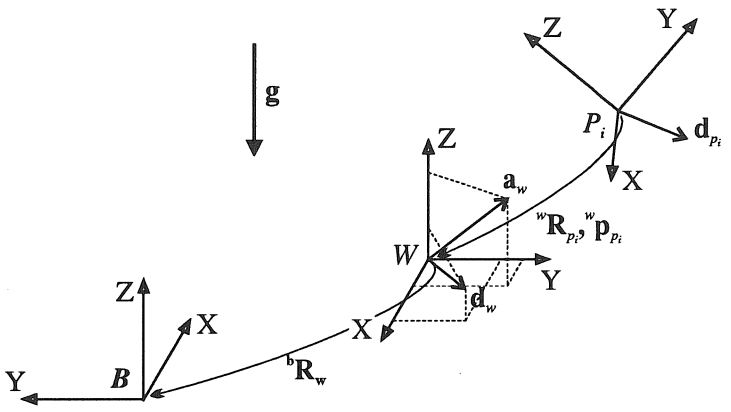

Figure C.3: Co-ordinate frames for the description of the influence of gravitation on translational accelerometer measurements.

plane frame $\{XYZ_w\}$, consists of three components:

$$(\ddot{\mathbf{d}}_{p_i})_w = \ddot{\mathbf{d}}_{\ddot{d}_w} + \ddot{\mathbf{d}}_{\ddot{a}_w} + \ddot{\mathbf{d}}_g. \tag{C.16}$$

- The first component is due to the translational accelerations of the rigid plane and equals:

$$\ddot{\mathbf{d}}_{\ddot{d}_w} = \ddot{\mathbf{d}}_w. \tag{C.17}$$

- The second component is due to the angular accelerations of the rigid plane and equals:

$$\ddot{\mathbf{d}}_{\ddot{a}_w} = \ddot{\mathbf{a}}_w \wedge {}^w\mathbf{p}_{p_i}, \tag{C.18}$$

$$= {}^w\mathbf{K}_{p_i}\,\ddot{\mathbf{a}}_w; \tag{C.19}$$

with

$$\begin{aligned} {}^w\mathbf{K}_{p_i} &= \left[\, \mathbf{x}_w \wedge {}^w\mathbf{p}_{p_i} \quad \mathbf{y}_w \wedge {}^w\mathbf{p}_{p_i} \quad \mathbf{z}_w \wedge {}^w\mathbf{p}_{p_i} \,\right] \\ &= \begin{bmatrix} 0 & ({}^w\mathbf{p}_{p_i})_z & -({}^w\mathbf{p}_{p_i})_y \\ -({}^w\mathbf{p}_{p_i})_z & 0 & ({}^w\mathbf{p}_{p_i})_x \\ ({}^w\mathbf{p}_{p_i})_y & -({}^w\mathbf{p}_{p_i})_x & 0 \end{bmatrix}. \end{aligned} \tag{C.20}$$

- The third component is due to gravitation. To derive a general mathematical expression for $\ddot{\mathbf{d}}_g$, the following assumptions have been made:

THE Z-AXIS OF THE ROBOT BASE FRAME

1. IS VERTICAL, AND
2. POINTS IN THE OPPOSITE DIRECTION OF THE GRAVITATIONAL ACCELERATION VECTOR.

Extending equations C.12 and C.13 to the general case yields the general mathematical expression for $\ddot{\mathbf{d}}_g$:

$$\ddot{\mathbf{d}}_g = \mathbf{a}_w \wedge \mathbf{g}_w, \tag{C.21}$$

with $\mathbf{g}_w$ the gravitational acceleration vector defined in the plane frame $\{XYZ_w\}$. SectionC.3.2 demonstrates the validity of this extension. Based on the above mentioned assumptions, an expression for $\mathbf{g}_w$ can be derived from the *known* expression of the gravitational acceleration vector defined in the robot base frame:

$$\begin{aligned} \mathbf{g}_w &= ({}^b\mathbf{R}_w)^t \begin{bmatrix} 0 \\ 0 \\ -g \end{bmatrix}, \\ &= -g\,({}^b\mathbf{r}_{\mathbf{3}w})^t; \end{aligned} \tag{C.22}$$

where ${}^b\mathbf{r}_{\mathbf{3}w}$ is the third row of ${}^b\mathbf{R}_w$, the orientation matrix of the rigid plane frame with respect to the robot base frame. The resulting mathematical expression for $\ddot{\mathbf{d}}_g$ becomes

$$\ddot{\mathbf{d}}_g = -g\,(\mathbf{a}_w \wedge ({}^b\mathbf{r}_{\mathbf{3}w})^t). \tag{C.23}$$

Summarizing, the general mathematical description of the translational accelerations in a structural point P_i of a rigid plane W, subject to a sinusoidal acceleration $\ddot{\mathcal{D}}_w$, is given by

$$(\ddot{\mathbf{d}}_{p_i})_w = \ddot{\mathbf{d}}_w + \ddot{\mathbf{a}}_w \wedge {}^w\mathbf{p}_{p_i} - g\,(\mathbf{a}_w \wedge {}^b\mathbf{r}_{\mathbf{3}w}), \tag{C.24}$$

where ${}^b\mathbf{r}_{\mathbf{3}w}$ is third row of ${}^b\mathbf{R}_w$, the orientation matrix of the rigid plane frame with respect to the robot base frame.

Transforming accelerations to displacements using equation C.3, the corresponding displacement vector in the structural point P_i, defined in the plane frame $\{XYZ_w\}$, is given by

$$\begin{aligned} (\mathbf{d}_{p_i})_w &= -\frac{(\ddot{\mathbf{d}}_{p_i})_w}{(2\pi f)^2}, \\ &= \mathbf{d}_w + \mathbf{a}_w \wedge {}^w\mathbf{p}_{p_i} + \mathbf{a}_w \wedge {}^b(\mathbf{d}_g)_w, \\ &= \mathbf{d}_w + \mathbf{a}_w \wedge \left({}^w\mathbf{p}_{p_i} + {}^b(\mathbf{d}_g)_w\right); \end{aligned} \tag{C.25}$$

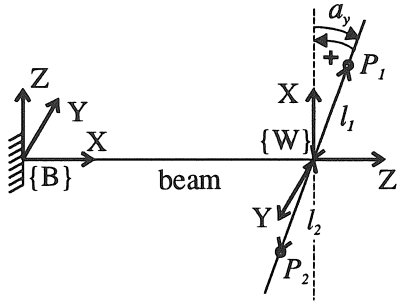

Figure C.4: Translational acceleration in two points of a rigid plane attached at the end of a clamped-free beam.

with

$$^b(\mathbf{d}_g)_w = \frac{g}{(2\pi f)^2} \, (^b\mathbf{r}_{\mathbf{3}w})^t.$$

C.3.2 Derivation of the mathematical expression for a clamped-free beam

Figure C.4 gives a schematic representation of the measurement of the translational acceleration in two points of a rigid plane attached at the end of a clamped-free beam.

For this setup following equalities are valid:

$$^b\mathbf{R}_w = \begin{bmatrix} 0 & 0 & 1 \\ 0 & -1 & 0 \\ 1 & 0 & 0 \end{bmatrix}, \tag{C.26}$$

$$^b\mathbf{r}_{\mathbf{3}w} = \begin{bmatrix} 1 \\ 0 \\ 0 \end{bmatrix}, \tag{C.27}$$

$$^w\mathbf{p}_{p_i} = \begin{bmatrix} l_i \\ 0 \\ 0 \end{bmatrix}, \tag{C.28}$$

with l_i=l_1 for i=1, l_i=-l_2 for i=2.

Using the equations derived in previous section, a mathematical expression can be derived for the translational acceleration, $(\ddot{\mathbf{d}}_{p_i})_w$, in point P_i.

1. Using equation C.17, $\ddot{\mathbf{d}}_{\ddot{d}_w}$ equals:

$$\ddot{\mathbf{d}}_{\ddot{d}_w} = \ddot{\mathbf{d}}_w. \tag{C.29}$$

2. Using equation C.19, with ${}^w\mathbf{p}_{p_i}$ replaced by equality C.28, $\ddot{\mathbf{d}}_{\ddot{a}_w}$ equals:

$$\ddot{\mathbf{d}}_{\ddot{a}_w} = \begin{bmatrix} 0 \\ l_i\,\ddot{a}_z \\ -l_i\,\ddot{a}_y \end{bmatrix}. \tag{C.30}$$

3. Using equation C.23, with ${}^b\mathbf{r}_{\mathbf{3}_w}$ replaced by equality C.27, $\ddot{\mathbf{d}}_g$ equals:

$$\ddot{\mathbf{d}}_g = \begin{bmatrix} 0 \\ -g\,a_z \\ g\,a_y \end{bmatrix}. \tag{C.31}$$

Substituting these equations into equation C.16 yields:

$$(\ddot{\mathbf{d}}_{p_i})_w = \ddot{\mathbf{d}}_w + \begin{bmatrix} 0 \\ l_i\,\ddot{a}_z \\ -l_i\,\ddot{a}_y \end{bmatrix} + \begin{bmatrix} 0 \\ -g\,a_z \\ g\,a_y \end{bmatrix}. \tag{C.32}$$

If the plane is subject only to a sinusoidal angular acceleration $\ddot{a}_y$, following equalities are valid:

$$\ddot{\mathbf{d}}_w = \begin{bmatrix} 0 \\ 0 \\ 0 \end{bmatrix}, \tag{C.33}$$

$$\ddot{\mathbf{a}}_w = \begin{bmatrix} 0 \\ \ddot{a}_y \\ 0 \end{bmatrix}. \tag{C.34}$$

Substituting these equalities into equation C.32 yields:

$$(\ddot{\mathbf{d}}_{p_i})_w = \begin{bmatrix} 0 \\ 0 \\ -l_i\,\ddot{a}_y + g\,a_y \end{bmatrix}. \tag{C.35}$$

By replacing

- $[(\ddot{d}_{p_i})_w]_z$ by $\ddot{d}_i$,
- $\ddot{a}_y$ by $\ddot{\alpha}$,
- a_y by α,
- l_i by l_1 for i=1, and l_i by -l_2 for i=2,

equation C.35 corresponds to equations C.12 and C.13 derived in section C.2.1. This proves the validity of the derived general mathematical expression.

Appendix D

Kinematic description of a manipulator

D.1 Denavit-Hartenberg approach

The Denavit-Hartenberg approach [86] for representing the kinematics of lower-pair mechanisms consists of:

a) a convention for assigning co-ordinate frames to the joint axes of the mechanism;

b) the definition of four describing parameters.

D.2 Assigning co-ordinate frames

- The Z_i-axis coincides with the $(i+1)^{th}$ joint axis;
- The X_i-axis is situated along the common normal of the Z_{i-1}-axis and the Z_i-axis. The cross product $Z_{i-1} \wedge Z_i$ determines the direction of the X_i-axis;
- The Y_i-axis is chosen so as to form a right handed co-ordinate frame.

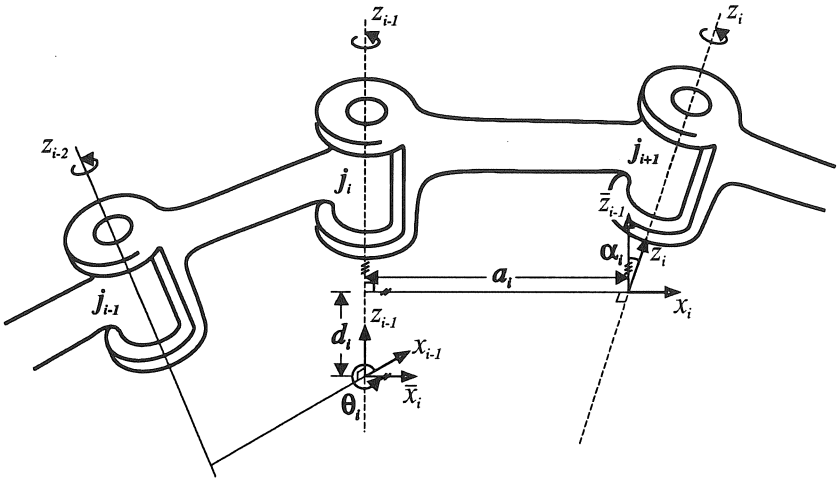

Figure D.1: Definition of Denavit-Hartenberg parameters.

D.3 Definition of Denavit-Hartenberg parameters

Joint frame $\{XYZ_i\}$ can be defined with respect to joint frame $\{XYZ_{i-1}\}$ by four parameters, called Denavit-Hartenberg parameters (figure D.1):

- θ_i: angle about Z_{i-1} between X_{i-1} and $\bar{X}_i$, where $\bar{X}_i$ is parallel to X_i;
- d_i: distance along Z_{i-1} between $\bar{X}_i$ and X_i;
- a_i: distance along X_i between Z_{i-1} and Z_i;
- α_i: angle about X_i between $\bar{Z}_{i-1}$ and Z_i, where $\bar{Z}_{i-1}$ is parallel to Z_{i-1}.

Either θ_i or d_i is the motion parameter:

- for a revolute joint: $\theta_i = q_i + \theta_i(0)$,
- for a prismatic joint: $d_i = q_i + d_i(0)$;

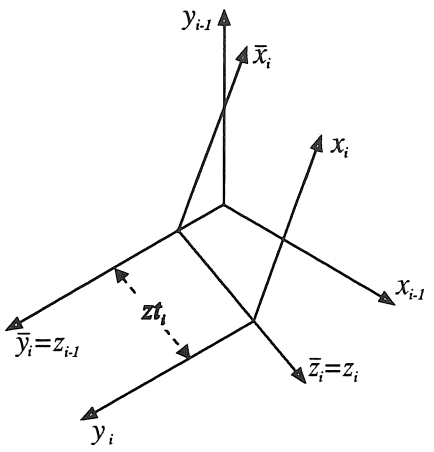

Figure D.2: Definition of zt_i.

where q_i is the joint value, and $\theta_i(0)$ and $d_i(0)$ are the Denavit-Hartenberg parameters of the mechanism is its reference position.

Van Aken [87] introduces a fifth parameter, zt_i, which represents the distance between o_{i-1} and o_i, measured along the Z_i-axis; zt_i solves the ambiguity in defining a common normal in case two successive joint axes intersect (figure D.2).

With these five parameters, the homogeneous transform ${}^{i-1}\mathbf{A}_i$ is given by:

$$
{}^{i-1}\mathbf{A}_i = \begin{bmatrix}
\cos\theta_i & -\sin\theta_i\cos\alpha_i & \sin\theta_i\sin\alpha_i & a_i\cos\theta_i + \sin\theta_i\sin\alpha_i\, zt_i \\
\sin\theta_i & \cos\theta_i\cos\alpha_i & -\cos\theta_i\sin\alpha_i & a_i\sin\theta_i - \cos\theta_i\sin\alpha_i\, zt_i \\
0 & \sin\alpha_i & \cos\alpha_i & d_i + \cos\alpha_i\, zt_i \\
0 & 0 & 0 & 1
\end{bmatrix} \tag{D.1}
$$

Appendix E

ROBOFLEX

E.1 Introduction

ROBOFLEX is a software package which has been developed within this research and which determines a static compliance model of an industrial robot based on quasi-static measurements. Section 2.2 describes the theory on which this software package is based.

The software is robot-independent, with the restriction that only serial driven robots can be modelled. The different components for which an appropriate compliance model is available are: prismatic long links, revolute joints, and robot bases with a diagonal compliance matrix. However, the software is built modular so other components and other compliance models can be easily added.

The software has been developed in Turbo Pascal 5.0.

E.2 Description of the ROBOFLEX program

Figure E.1 gives a schematic overview of the **ROBOFLEX** program. The **ROBOFLEX** program consists of three main parts: (1) a data initialization part, (2) a quasi-static measurement part, and (3) a compliance modelling part. The data transfer between the different parts is realized through ASCII files. In the figure these files are indicated with **.xyz*. The extension *xyz* defines the type of information the considered file contains.

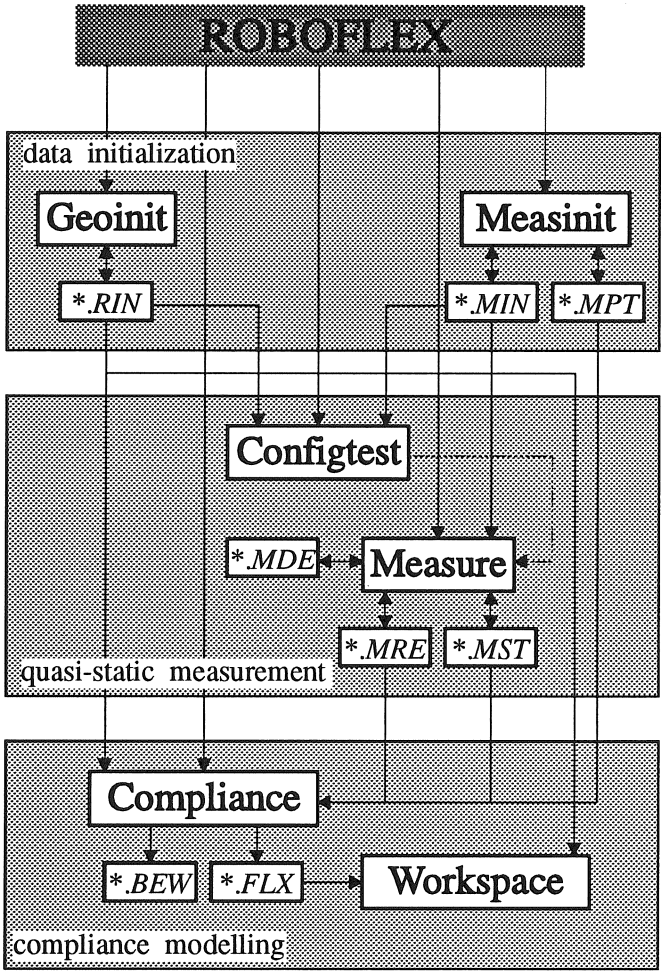

Figure E.1: Schematic overview of the **ROBOFLEX** software.

E.2.1 Data initialization

Before starting the quasi-static measurement and the subsequent compliance modelling some general parameters need to be initialized. This data initialization part consists of two subparts:

- input and change of the geometrical parameters: module **Geoinit**;
- input and change of the measurement parameters: module **Measinit**.

The two modules demand automatically all required parameters.

E.2.1.1 Input and change of the geometrical parameters: Geoinit

The geometrical parameters of the different elements which need to be initialized are:

robot

number of degrees-of-freedom, Denavit-Hartenberg parameters of the joint frames, Denavit-Hartenberg parameters of the link frames defined with respect to the corresponding joint frame, mass information (mass and center of gravity) of the links defined with respect to the corresponding link frame, limits of the joint angles.

force transducer: single or multi component

Denavit-Hartenberg parameters of the sensor frame defined with respect to the end-effector frame, mass information (mass and center of gravity) of the force transducer defined with respect to the corresponding sensor frame.

accelerometer

position of the acceleration measuring points defined with respect to the reference frame of the accelerometer.

All those geometrical parameters are stored in a **.RIN* file.

E.2.1.2 Input and change of the measurement parameters: Measinit

The measurement parameters of the different elements which need to be initialized are:

robot

position of the excitation point defined with respect to the end-effector frame, joint angles of the different robot configurations in which the quasi-static measurements will be carried out.

force transducer

sensitivity of the force transducer, in case of a multi component force transducer cross-sensitivities can be included.

accelerometer

sensitivity of the accelerometer.

All those measurement parameters are stored in a **.MIN* file.

Next to these measurement parameters the position and orientation of the different points in which the accelerations will be measured need to be initialized. At least three points need to be defined for each reference plane characterizing a compliant component. Those measurement parameters are stored in a **.MPT* file.

E.2.2 Quasi-static measurement

If all necessary geometrical and measurement parameters are initialized the quasi-static measurement can be carried out. This quasi-static measurement part consists of two subparts:

- testing of the considered robot configuration: module **Configtest**;
- quasi-static measurement: module **Measure**.

E.2.2.1 Testing of the considered robot configuration: Configtest

This module allows the verify, for a given excitation position and excitation force, the forces and moments that will be applied to the different links and joints of the considered robot. This is necessary to

check if no deformation of a component of the considered robot is left outside of consideration.

E.2.2.2 Quasi-static measurement: Measure

Through a multi-channel data acquisition system, linked to the micro-computer, this module

- acquires the (filtered) measured data,
- determines the magnitude and the phase dependent behaviour of the measured displacements and forces, based on a least squares approximation at the considered frequency and for a number of repeated measurements,
- controls the excitation frequency and excitation force.

The data acquisition system used within this research is a 8-channel Data-Harvester [61]. However, this software is built modular so software required for other data acquisition systems can be easily added.

Within this module some extra measurement parameters need to be initialized. Those parameters are the number of measuring channels, the reference channel to determine the frequency responses of the robot, the desired excitation force and excitation frequency, and the number of repeated measurements. All those measurement parameters are stored in a **.MDE* file.

If all the necessary parameters are initialized the quasi-static measurements can be carried out. The only information required for each measurement is the number of the considered robot configuration, the number of the link which is measured, the number of the corresponding reference plane, and the number of the measuring point within this plane. The results of those measurements are stored in a **.MRE* file. Besides this file, a **.MST* is created which keeps up to date which measuring points for which robot configuration have already been measured.

Besides the quasi-static measurement this module also allows to determine the frequency responses of the robot. Those are necessary to choose the quasi-static excitation frequency.

E.2.3 Compliance modelling

If a sufficient number of quasi-static measurements are carried out the compliance modelling can start. This compliance modelling part contains two subparts:

- compliance modelling: module **Compliance**;
- workspace analysis: module **Workspace**.

E.2.3.1 Compliance modelling: Compliance

The data used by this module are the geometrical data (**.RIN*), the measurement data (**.MPT*) and the data resulting of the previous described module (**.MRE* and **.MST*). In a first step this module determines for which components of the robot a sufficient number of quasi-static measurements have been carried out to be able to calculate the compliance parameters. In a second step the module calculates the movement of the different reference planes characterizing the selected components. The resulting displacement and rotation vectors are stored in a **.BEW* file. Finally, the compliance parameters of the selected components are determined and are stored in a **.FLX* file.

E.2.3.2 Workspace analysis: Workspace

Based on the previously determined compliance parameters, this module allows to analyze the compliance of the robot within its total workspace. Section 2.3.3 shows an example of such a workspace analysis.

Appendix F

Some basic features of laser theory

F.1 Introduction

The word laser is an acronym for *L*ight *A*mplification by *S*timulated *E*mission of *R*adiation. A laser is a light amplifier which is capable of producing an intense beam of photons having identical scalar and vector properties (frequency, phase, direction and polarization). As a result, the beam has special characteristics: brightness, monochromaticity, coherence, and unidirectionality. All laser applications are dependent on one or more of these special characteristics.

This appendix deals only with those aspects of laser theory which contribute to a better comprehension of the previous chapters.

F.2 Mode structure of a laser beam

Lasers are characterized by a longitudinal mode structure, as well as by a transverse mode structure. A red HeNe laser is characterized by a longitudinal mode with a wavelength of $632.8nm$. In addition to longitudinal mode structure, the radiation field of a laser may have nodes and antinodes in the plane perpendicular to the laser axis. The different transverse irradiance (intensity) patterns are referred to as Transverse Electric and Magnetic (TEM) modes. Transverse modes are identified by their irradiance distributions and are designated TEM_{pq},

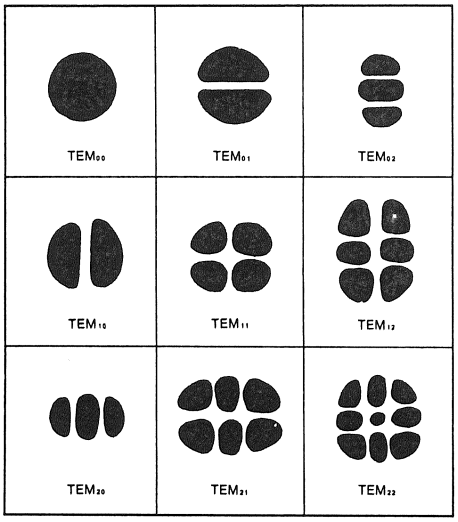

Figure F.1: Transverse Electric and Magnetic modes of a laser.

where the subscripts p and q refer to the number of nodes along the two orthogonal axes perpendicular to the laser axis. Figure F.1 [74] shows some TEM-modes of a laser. The irradiance distributions of all these modes are smoothly varying but none has a uniform irradiance distribution. The lowest order mode, TEM_{00}, has a cylindrical Gaussian irradiance distribution. This mode experiences the minimum possible diffraction loss, has minimum divergence, and can be focused to the smallest possible spot. For these reasons, laboratory HeNe lasers, and semiconductor lasers, are designed to ensure pure TEM_{00} output.

F.3 Gaussian beam optics

F.3.1 Gaussian beams

In the TEM_{00} mode, the beam emitted from a HeNe laser has a perfect plane wave front and a cylindrical Gaussian transverse irradiance profile. The Gaussian shape is truncated at some diameter either by the laser bore or some limiting aperture in the optical train. The commonly adopted definition for the beam diameter is the diameter at which the transverse field amplitude has fallen to a fraction $1/e$ of its peak axial value. At this same diameter, the corresponding beam

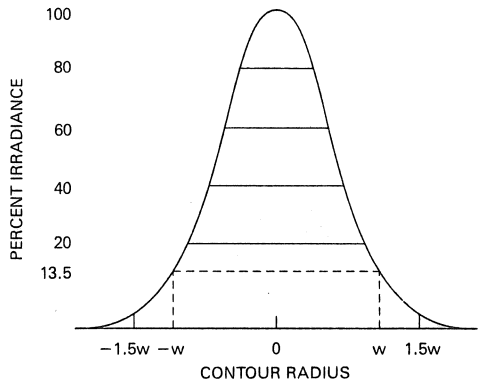

Figure F.2: Gaussian irradiance profile for TEM_{00} mode, showing definition of beam radius w.

irradiance will have fallen to $1/e^2$ (13.5%) of its peak or axial value (figure F.2 [74]).

F.3.2 Beam divergence

Diffraction causes light waves to spread transversely as they propagate, and it is therefore impossible to have a perfectly collimated beam. The spreading of HeNe laser beams, and of semiconductor laser beams, is in precise accord with the predictions of pure diffraction theory. The formulas which follow accurately describe beam spreading. Through them it is easy to see the capabilities and limitations of laser beams. The notation is consistent with much of laser literature.

Even if a Gaussian TEM_{00} laser beam wave front were made perfectly flat at some plane, it would quickly acquire curvature and begin spreading in accordance with

$$w(z) = w_0 \cdot \left[1 + \left(\frac{\lambda z}{\pi {w_0}^2}\right)^2\right]^{\frac{1}{2}}, \qquad \text{(F.1)}$$

where z is the distance propagated from the plane where the wave front was flat, λ is the wavelength of the laser light, w_0 is the radius of the $1/e^2$ irradiance contour at the plane where the wave front was flat, and $w(z)$ is the radius of the $1/e^2$ contour after the wave has propagated a distance z. The plane z=0 marks the location of a Gaussian "waist",

or a place where the wave front is flat, and w_0 is called the waist radius. A waist occurs at the surface of the plane mirror of the cavity used in HeNe lasers.
For large z, $w(z)$ asymptotically approaches the value

$$w(z) \cong \frac{\lambda z}{\pi w_0}, \tag{F.2}$$

where z is presumed much larger than $\frac{\pi {w_0}^2}{\lambda}$ so that the $1/e^2$ irradiance contours asymptotically approach a cone of angular radius θ, with

$$\theta = \frac{w(z)}{z} = \frac{\lambda}{\pi w_0}. \tag{F.3}$$

This value is the far field angular radius of the Gaussian TEM_{00} beam. The vertex of the cone lies at the centre of the waist (figure F.3 [74]).

The irradiance distribution of the Gaussian TEM_{00} beam, namely

$$I(r) = I_0 . \exp \frac{-2r^2}{w^2} = \frac{2P}{\pi w^2} . \exp \frac{-2r^2}{w^2}, \tag{F.4}$$

is the same at all cross sections of the beam, where $w = w(z)$ and P is the total power in the beam.

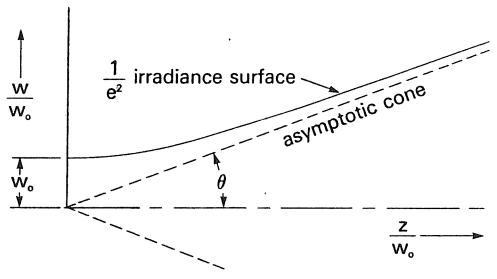

Figure F.3: Growth in $1/e^2$ contour radius with distance propagated away from Gaussian waist.

Appendix G

Formulas concerning optical deflection measurement

G.1 Introduction

This appendix contains detailed mathematical derivations in connection with the relation between the structural deflections of a flexible link and the measurements by the optical transducers. The different co-ordinate frames, used to describe this relation, are defined in section 3.4.3.1.1.

G.2 Co-ordinates of the laser spot in the corrected sensor frame

Figure G.1 shows the geometrical relation between the structural deflections d_x, d_y, a_z and the co-ordinates of the laser spot. This applies only for the PSD's without a lens (i=1–2). The description of the corrected sensor frame, before deflection, relative to the reference frame is given by the homogeneous transform ${}^{r}\mathbf{A}_1$, defined by:

$$ {}^{r}\mathbf{A}_1 = \begin{bmatrix} 1 & 0 & S_i c_i \\ 0 & 1 & S_i s_i \\ 0 & 0 & 1 \end{bmatrix}, \qquad \text{(G.1)} $$

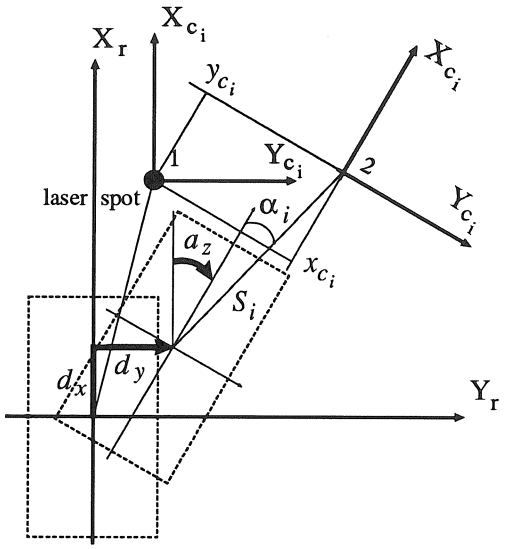

Figure G.1: Geometrical relation between the structural deflections d_x, d_y, a_z and the co-ordinates of the laser spot.

where c_i=cos α_i and s_i=sin α_i. Due to the structural deflections d_x, d_y and a_z, the PSD moves from position **1** to position **2** whereas the laser spot remains at position **1**. The homogeneous transform for ${}^r\mathbf{A}_2$ is defined by

$$ {}^r\mathbf{A}_2 = \mathbf{A}\ {}^r\mathbf{A}_1, \tag{G.2} $$

with **A** the transformation matrix due to the structural deflections, defined by:

$$ \mathbf{A} = Translation(X_r, d_x)\ \ Translation(Y_r, d_y)\ \ Rotation(Z_r, a_z). $$

Using the equations of appendix B.3, **A** becomes:

$$ \mathbf{A} = \begin{bmatrix} & \mathbf{R} & & \mathbf{p} \\ 0 & & 0 & 1 \end{bmatrix} = \begin{bmatrix} c_z & -s_z & d_x \\ s_z & c_z & d_y \\ 0 & 0 & 1 \end{bmatrix}, \tag{G.3} $$

where c_z=cos a_z and s_z=sin a_z. The co-ordinates of the laser spot in the corrected sensor frame are given by the position vector ${}^2\mathbf{p}_1$, part

of the homogeneous transform ${}^2\mathbf{A}_1$, with ${}^2\mathbf{A}_1$ defined by

$$\begin{aligned} {}^r\mathbf{A}_2\,{}^2\mathbf{A}_1 &= {}^r\mathbf{A}_1, \\ {}^2\mathbf{A}_1 &= {}^r\mathbf{A}_2^{-1}\,{}^r\mathbf{A}_1. \end{aligned}$$

Taking into account equation G.2:

$$\begin{aligned} {}^2\mathbf{A}_1 &= (\mathbf{A}\,{}^r\mathbf{A}_1)^{-1}\,{}^r\mathbf{A}_1, \\ &= {}^r\mathbf{A}_1^{-1}\,\mathbf{A}^{-1}\,{}^r\mathbf{A}_1. \end{aligned} \tag{G.4}$$

Taking into account the properties of inverse homogeneous transforms, described in appendix B.2, the co-ordinates of the laser spot in the corrected sensor frame, given by ${}^2\mathbf{p}_1$, are calculated as follows

$${}^2\mathbf{p}_1 = -{}^r\mathbf{p}_1 - \mathbf{R}^t(\mathbf{p} - {}^r\mathbf{p}_1)$$

or,

$$x_{c_i} = -S_i c_i - c_z(d_x - S_i c_i) - s_z(d_y - S_i s_i), \tag{G.5}$$

$$y_{c_i} = -S_i s_i + s_z(d_x - S_i c_i) - c_z(d_y - S_i s_i). \tag{G.6}$$

G.3 Calculation of structural deflections d_x, d_y and a_z

This appendix deals with the derivation of the equations describing the structural deflections d_x, d_y and a_z as a function of the co-ordinates of the laser spots on the PSD's without a lens.

Equations G.5 and G.6 describe the relation between the co-ordinates of the laser spots on the PSD's and the structural deflections d_x, d_y and a_z. Within these equations, the torsion angle a_z is not found directly, but the sine and cosine of the angle are. So, three structural deflections result in four unknowns, and four equations are needed to determine these three structural deflections.

Solving equations G.5 and G.6 for the structural deflections d_x and d_y yields

$$d_x = S_i c_i - c_z(x_{c_i} + S_i c_i) + s_z(y_{c_i} + S_i s_i), \tag{G.7}$$

$$d_y = S_i s_i - s_z(x_{c_i} + S_i c_i) - c_z(y_{c_i} + S_i s_i). \tag{G.8}$$

If the structural deflection a_z is known, the structural deflections d_x and d_y can be calculated from the equations G.7 and G.8. The structural deflections d_x and d_y should be the same for both PSD's ($i = 1, 2$):

$$\begin{aligned} &\text{Equation G.7 } (i{=}1) = \text{Equation G.7 } (i{=}2), \\ &\text{Equation G.8 } (i{=}1) = \text{Equation G.8 } (i{=}2) \end{aligned}$$

or,

$$\begin{aligned} S_1c_1 - c_z(x_{c_1} + S_1c_1) + s_z(y_{c_1} + S_1s_1) = \\ S_2c_2 - c_z(x_{c_2} + S_2c_2) + s_z(y_{c_2} + S_2s_2), \quad \text{(G.9)} \end{aligned}$$

$$\begin{aligned} S_1s_1 - s_z(x_{c_1} + S_1c_1) - c_z(y_{c_1} + S_1s_1) = \\ S_2s_2 - s_z(x_{c_2} + S_2c_2) - c_z(y_{c_2} + S_2s_2). \quad \text{(G.10)} \end{aligned}$$

Solving equations G.9 and G.10 for s_z and c_z yields the structural deflections d_x, d_y and a_z:

$$\begin{aligned} s_z &= [(S_2s_2 - S_1s_1)(x_{c_2} + S_2c_2 - x_{c_1} - S_1c_1) \\ &\quad -(S_2c_2 - S_1c_1)(y_{c_2} + S_2s_2 - y_{c_1} - S_1s_1)]/\Delta, \\ c_z &= [(S_2c_2 - S_1c_1)(x_{c_2} + S_2c_2 - x_{c_1} - S_1c_1) \\ &\quad +(S_2s_2 - S_1s_1)(y_{c_2} + S_2s_2 - y_{c_1} - S_1s_1)]/\Delta, \\ \Delta &= (y_{c_2} + S_2s_2 - y_{c_1} - S_1s_1)^2 + (x_{c_2} + S_2c_2 - x_{c_1} - S_1c_1)^2. \end{aligned}$$

Putting s_z and c_z into equations G.7 and G.8 yields the the structural deflections d_x and d_y. The torsion angle a_z can be calculated as follows:

$$a_z = \arctan\frac{s_z}{c_z}. \quad \text{(G.11)}$$

G.4 Formulas concerning lens-PSD system

This appendix deals with the derivation of the equations describing the co-ordinates of the laser spot on the PSD, which forms part of a lens-PSD system, as a function of the structural deflections d_x, d_y, a_x, a_y and a_z. The co-ordinates are defined with respect to the sensor co-ordinate frame. For a lens-PSD system, a corrected sensor frame is not needed.

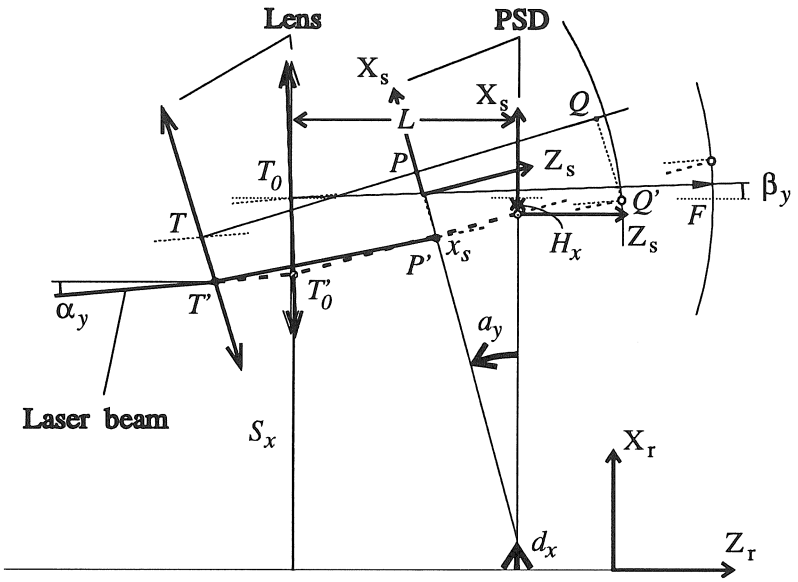

Figure G.2: Geometrical relation between the co-ordinate x_s and the structural deflections d_x and a_y for a lens-PSD system.

A first application of a lens-PSD system is the measurement of the structural deflections a_x and a_y. A second application consists of using a lens-PSD system to realize a larger measuring range with a smaller PSD.

The equations are derived for the structural deflections d_x and a_y. The equations for the structural deflections d_y and a_x are analogue the equations for d_x and a_y.

Assume a_z=0 or is negligible. Figure G.2 shows the geometrical relation between the co-ordinate x_s of the laser spot on the PSD and the structural deflections d_x and a_y for a lens-PSD system. This figure is the projection in the XZ-plane of the reference co-ordinate frame of the physical lens-PSD system. If $a_z \neq 0$ then the projection in the XZ-plane of the *rotated* reference co-ordinate frame should be considered.

The derivation is based on the congruence of triangles:

$$\frac{\overline{TT'} - \overline{QQ'}}{\overline{PP'} - \overline{QQ'}} = \frac{\overline{TQ}}{\overline{PQ}}, \tag{G.12}$$

where : T : intersection of the lens and its optical axis;
T' : intersection of the lens and the laser beam;
P : projection of P' on the optical axis;
P' : intersection of the laser beam and the PSD;
Q : projection of Q' on the optical axis;
Q' : imaginary intersection of the laser beam and the focal plane of the lens.

This congruence is considered after deflection due to d_x and a_y. The line segments are defined within the optical axis co-ordinate frame $\{x_{op}, y_{op}\}$.
Following relations are found from figure G.2:

$$\overline{QQ'} = -F \sin(a_y + \beta_y - \alpha_y); \tag{G.13}$$

$$\overline{PP'} = x_s \cos\beta_y - L \sin\beta_y - H_x \cos\beta_y; \tag{G.14}$$

$$\overline{TT'} = \frac{S_x - \cos a_y (S_x + \overline{TT'_{0x}} \cos\beta_y) + L \sin a_y - d_x}{\cos(a_y + \beta_y)}; \tag{G.15}$$

$$\overline{TQ} = F \cos(a_y + \beta_y - \alpha_y); \tag{G.16}$$

$$\overline{PQ} = F \cos(a_y + \beta_y - \alpha_y) - \frac{L}{\cos\beta_y} - \overline{PP'} \tan\beta_y; \tag{G.17}$$

where : F : focal length of the lens;
L : distance along the optical axis of an ideal lens (β_y=0) between lens and PSD;
H_x : x-component within the sensor frame of the distance between the origin of the sensor frame and the intersection of the optical axis of an ideal lens and the PSD;
S_x : x-component within the reference frame of the perpendicular distance from T'_0 to the Z-axis of the reference frame;
T_0 : intersection of the lens and its optical axis, before deflection;

T_0' : intersection of the lens and the laser beam, before deflection;
$\overline{TT'_{0x}}$: x-component within the reference frame of the distance between T_0 and T_0';
α_y : angle defined in the XZ-plane of the reference frame between the laser beam and the Z-axis of the reference frame;
β_y : angle defined in the XZ-plane of the sensor frame between the optical axis of the lens and the Z-axis of the sensor frame.

To find equation G.15, a first assumption is made: α_y is assumed to be small so the laser beam is almost parallel to the Z-axis of the reference frame and S_x is the perpendicular distance from each T' to the Z-axis of the reference frame.

Solving equations G.12, G.13, G.16 and G.17 for $\overline{PP'}$ yields:

$$\overline{PP'} = \frac{\overline{TT'}(F\cos(a_y+\beta_y-\alpha_y) - \frac{L}{\cos\beta_y}) - \frac{L}{\cos\beta_y}F\sin(a_y+\beta_y-\alpha_y)}{F\cos(a_y+\beta_y-\alpha_y) + \tan\beta_y(\overline{TT'} + F\sin(a_y+\beta_y-\alpha_y))}. \tag{G.18}$$

Solving equation G.14 for x_s, taking into account equation G.18, yields:

$$\begin{aligned} x_s &= \frac{\overline{TT'}(1 - \frac{L}{F\cos(a_y+\beta_y-\alpha_y)\cos\beta_y}) - \frac{L}{\cos\beta_y}\tan(a_y+\beta_y-\alpha_y)}{\cos\beta_y + \frac{\overline{TT'}\sin\beta_y}{F\cos(a_y+\beta_y-\alpha_y)} + \sin\beta_y\tan(a_y+\beta_y-\alpha_y)} \\ &\quad + L\tan\beta_y + H_x. \end{aligned} \tag{G.19}$$

This exact formula for x_s as a function of d_x and a_y is however hardly solvable. Therefore, a second assumption is made: β_y is assumed to be small so in equation G.17 the term $\overline{PP'}\tan\beta_y$ is negligible with respect to the other terms. Taking into account equation G.15, equation G.19 becomes:

$$\begin{aligned} x_s &= A\,(1 - \frac{L}{F\cos(a_y+\beta_y-\alpha_y)\cos\beta_y}) - \frac{L}{\cos^2\beta_y}\tan(a_y+\beta_y-\alpha_y) \\ &\quad + L\tan\beta_y + H_x, \end{aligned} \tag{G.20}$$

with

$$A = \frac{S_x - \cos a_y(S_x + \overline{TT'_{0x}}\cos\beta_y) + L\sin a_y - d_x}{\cos(a_y + \beta_y)\cos\beta_y}. \qquad \text{(G.21)}$$

Within this equation, one parameter can be eliminated, that is H_x. This parameter is not a real structural parameter: it is a function of the real structural parameters F, L, $\overline{TT'_{0x}}$, α_y and β_y. This relation is derived by considering equation G.20 before deflection: in this case $d_x = 0$, $a_y = 0$ and by definition of the sensor co-ordinate frame $x_s = 0$; H_x as a function of the real structural parameters becomes:

$$H_x = \frac{\overline{TT'_{0x}}}{\cos\beta_y}\left(1 - \frac{L}{F\cos(\beta_y - \alpha_y)\cos\beta_y}\right) + \frac{L}{\cos^2\beta_y}\tan(\beta_y - \alpha_y) - L\tan\beta_y. \qquad \text{(G.22)}$$

Since a_y, α_y and β_y are small, following approximations are valid:

$$\cos\beta_y \approx 1; \qquad \text{(G.23)}$$

$$\cos(\beta_y - \alpha_y) \approx 1; \qquad \text{(G.24)}$$

$$\cos(a_y + \beta_y - \alpha_y) \approx 1; \qquad \text{(G.25)}$$

$$\tan(\beta_y - \alpha_y) \approx \tan\beta_y - \tan\alpha_y; \qquad \text{(G.26)}$$

$$\tan(a_y + \beta_y - \alpha_y) \approx \tan a_y + \tan\beta_y - \tan\alpha_y. \qquad \text{(G.27)}$$

Taking into account equation G.22 and approximations G.26 and G.27, equation G.20 becomes:

$$\begin{aligned} x_s &= A\left(1 - \frac{L}{F\cos(a_y + \beta_y - \alpha_y)\cos\beta_y}\right) - \frac{L}{\cos^2\beta_y}\tan a_y \\ &\quad + \frac{\overline{TT'_{0x}}}{\cos\beta_y}\left(1 - \frac{L}{F\cos(\beta_y - \alpha_y)\cos\beta_y}\right), \end{aligned} \qquad \text{(G.28)}$$

with

$$A = \frac{S_x - \cos a_y(S_x + \overline{TT'_{0x}}\cos\beta_y) + L\sin a_y - d_x}{\cos(a_y + \beta_y)\cos\beta_y}.$$

This is the most general equation which describes the co-ordinate x_s of the laser spot on the PSD as a function of the structural deflections d_x and a_y for an arbitrary distance L between the lens and the PSD.

If the lens-PSD system is used to measure the structural deflections a_x and a_y, the PSD should be mounted in the focal plane of the lens, or L should be equal F. This is the third assumption. In this case, taking into account approximations G.23, G.24 and G.25, the first and the third term of equation G.28 are negligible with respect to the second one. Equation G.28 is reduced to:

$$x_s = -L \tan a_y. \tag{G.29}$$

Finally, the formulas to calculate the structural deflections a_x and a_y are:

$$a_y = \arctan \frac{-x_s}{L} \tag{G.30}$$

$$a_x = \arctan \frac{y_s}{L}. \tag{G.31}$$

a_z is assumed to be negligible. If however a_z becomes important, the formulas to calculate the structural deflections a_x and a_y remain the same if a_x and a_y are defined with respect to the rotated reference frame.

If the lens-PSD system is used to realize a larger measuring range with a smaller PSD, L should be chosen smaller than F. The value of L is determined by the desired measuring range and by the dimensions of the sensitive surface of the available PSD. The desired measuring range determines also the dimensions of the lens. However, the computations are much more complex than within the original optical measurement system. Two identical lens-PSD systems are needed to determine the structural deflections d_x, d_y and a_z. To get rid of the influence of the structural deflections a_x and a_y, a third lens-PSD system with the PSD mounted in the focal plane of the lens should be used.

For the lens-PSD system with $L \neq F$, the parameters of equation G.28 should be adapted if $a_z \neq 0$. Because in this case the structural deflections a_x and a_y are defined with respect to the rotated reference frame, equation G.28 is also defined with respect to the rotated reference frame: all parameters within this equation, which are before deflection defined with respect to the reference frame, should after deflection be defined with respect to the rotated reference frame. The transition of the parameters from the reference frame to the rotated reference frame is realized by the homogeneous transform ${}^{rr}\mathbf{A}_r$, which

represents the description of the reference frame relative to the rotated reference frame:

$$ {}^{rr}\mathbf{A}_r = \begin{bmatrix} c_z & s_z & 0 \\ -s_z & c_z & 0 \\ 0 & 0 & 1 \end{bmatrix}. \qquad \text{(G.32)} $$

So, the structural deflection d_x within equation G.28 should be replaced by $d_x c_z + d_y s_z$:

$$ \begin{bmatrix} d_x c_z + d_y s_z \\ -d_x s_z + d_y c_z \\ 1 \end{bmatrix} = {}^{rr}\mathbf{A}_r \begin{bmatrix} d_x \\ d_y \\ 1 \end{bmatrix} \qquad \text{(G.33)} $$

The same should be done with the following sets of parameters: (S_x,S_y), (α_x,α_y) and $(\overline{TT'_{0x}},\overline{TT'_{0y}})$.

G.5 Calibration of the focal length of the lens

The objective of this calibration is the determination of the focal length of the lens used in the lens-PSD system, and of the distance L between the lens and the PSD. An additional application of this calibration is the verification if the PSD is mounted really in the focal plane of the lens: if $L{=}F$.

This calibration starts from equation G.28 which describes the coordinate x_s of the laser spot on the PSD as a function of the structural deflections d_x and a_y for an arbitrary distance L between the lens and the PSD.

$$ \begin{aligned} x_s &= A\,(1 - \frac{L}{F\cos(a_y + \beta_y - \alpha_y)\cos\beta_y}) - \frac{L}{\cos^2\beta_y}\tan a_y \\ &\quad + \frac{\overline{TT'_{0x}}}{\cos\beta_y}(1 - \frac{L}{F\cos(\beta_y - \alpha_y)\cos\beta_y}), \end{aligned} $$

with

$$ A = \frac{S_x - \cos a_y(S_x + \overline{TT'_{0x}}\cos\beta_y) + L\sin a_y - d_x}{\cos(a_y + \beta_y)\cos\beta_y}. $$

Referring to the first two structural requirements of the lens-PSD system of section 3.4.3.1.3, α_y and β_y are assumed to be small. If no

bending angle ($a_y = 0$) is applied to the lens-PSD system, this equation becomes:

$$x_s = -(1 - \frac{L}{F})d_x. \tag{G.34}$$

This is the formula of a straight line. If L is known, F is determined by applying at least one displacement d_x to the lens-PSD system. However L is difficult to measure accurately. Therefore, L is subdivided into two parts: $L = L^* + dL$, where L^* has a variable length, which can be measured very accurately, and dL is the unknown distance. By varying L^*, for a certain d_x, a set of equations is found from which F and dL are easily derived:

$$[L_i^*] = F\left[\frac{x_{s_i}}{d_x} + 1\right] - dL. \tag{G.35}$$

Once F and dL are derived, L^* can be adapted so $L^* + dL = F$ which meets the third structural requirement of the lens-PSD system of section 3.4.3.1.3.

These equations depends only on the system parameters due to the lens-PSD system: all other system parameters due to the global measurement system have disappeared. So, this calibration can be done by the manufacturer of the measurement system.

To calibrate the focal length of the lens, described in table 3.5, and to adapt, for the corresponding lens-PSD system, L so L=F, following method has been used [77]. The lens-PSD system has been mounted on a 3D co-ordinate measuring machine which is used to realize the displacement d_x. Subsequently, x_s is measured for four different lengths of L^*. Solving the set of equations G.35 results in a value of $56.41mm$ for the focal length of the considered lens, which corresponds to the value of $56mm \pm 1\%$ given in table 3.5.

G.6 Formulas concerning focused laser beams passing through a lens

This appendix deals with the derivation of the equations describing the place where the minimal cross-section of a focussed laser beam occurs when this laser beam passes through another lens. From this, the real cross-section of the light spot on the PSD can be deduced.

Because of their electromagnetic properties, laser beams can not be totally focussed. Equation 3.52 gives the minimal cross-section $2w_0$ of the laser beam:

$$2w_0 = \frac{4\lambda F_d}{\pi D}, \tag{G.36}$$

where : λ : output wavelength of the laser beam;
F_d : focal distance of the semiconductor laser;
D : diameter of the output beam.

An equation to describe the behaviour of a nonparallel laser beam passing through a lens is the thin lens equation for Gaussian beams [80]:

$$(z - F)(z' - F) = F^2 - {F_0}^2, \tag{G.37}$$

where F is the focal length of the lens, and F_0 is a correction factor which considers the electromagnetic properties of the laser beam. The other quantities are defined in figure G.3. An important quantity is the Raleigh zone. By definition, the Raleigh zone is the zone in which the radius of the laser beam varies from w_0 to $\sqrt{2}w_0$. The Rayleigh zone measures z_R:

$$z_R = \frac{\pi {w_0}^2}{\lambda} \qquad z'_R = \frac{\pi {w'_0}^2}{\lambda}. \tag{G.38}$$

The new minimal cross-section $2w'_0$ of the laser beam is given by:

$$(2w'_0)^2 = \frac{4F^2 {w_0}^2}{(z - F)^2 + {z_R}^2}. \tag{G.39}$$

From these quantities, the correction factor F_0 can be calculated:

$$F_0 = \sqrt{z_R z'_R} = \frac{\pi w_0 w'_0}{\lambda}. \tag{G.40}$$

With respect to the optical measurement system, those quantities have following meaning:

- z : distance between the lens and the original focal plane of the focussed semiconductor laser;
- z' : distance between the lens and the place where the new minimal cross-section of the focussed laser beam occurs;
- $2w_0$: original minimal cross-section of the focussed laser beam;
- $2w'_0$: new minimal cross-section of the focussed laser beam.

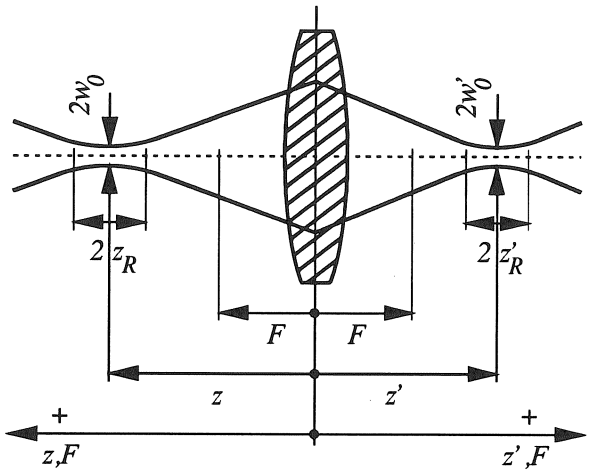

Figure G.3: Transformation of a Gaussian beam by a thin lens.

The place where the minimal cross-section of a focussed laser beam occurs when this laser beam passes through another lens is given by z', and is calculated from equation G.37. The real cross-section of the light spot on the PSD $2w_{psd}$ is calculated as follows:

$$2w_{psd} = 2w_l \frac{F - z'}{z'}, \tag{G.41}$$

where w_l is the radius of the light spot on the lens. w_l is given by:

$$w_l = D \frac{z}{2F_d}. \tag{G.42}$$